공학박사 학위논문

Novel Design of Syntheses and Materials for Stable and Efficient Perovskite Photovoltaics

소재 및 공정 설계를 통한

장수명 고효율의 페로브스카이트 광전소자 구현

2019 년 8 월

서울대학교 대학원

재료공학부

김진현

Ph.D. Thesis

Novel Design of Syntheses and Materials for Stable and Efficient Perovskite Photovoltaics

Jinhyun Kim

August 2019

Department of Materials Science and Engineering

Seoul National University

Abstract

Global energy demand mainly relies on fossil fuels, petrochemical, and nuclear energy. Those causes the emission of greenhouse gas and radioactive waste, threatening the mankind. Alternatively, renewable energy is slowly replacing the demand of current energy sources, yet the portion of renewable energy production is very small. Solar cell is one of the most promising energy production by converting incident light into electricity, expecting the solution for energy problem without environmental issues. In order to make solar cell compatible in an energy market, high power conversion efficiency (PCE) at low production cost with high durability should be satisfied. Moreover, solar cells must applicate into various situations in human lives, such as wearable devices, improving the efficiency of energy production. Therefore, understanding and developing the science of material and device must be advocated to commercialize the solar cells in a broad market.

Researchers have been explored the sufficient material and device structures to robust the potential of solar cell. Especially, utilization of thin-film semiconductor in solar cell has explored widely due to its superior optoelectronic properties. Among the various types of thin-film semiconducting materials, organometallic perovskite has demonstrated amorous potential due to the nature advantage of proper bandgap, absorption coefficient, and diffusion length. Moreover, synthesis and fabrication of material and layer are inexpensive and facile, promising for the large scale production. However, the organic site of organometallic perovskite (methylamonium (MA) or formamidinium (FA)) is highly reactive under light, heat, and water, making device insufficient for the commercial

use.   Despite the issues of organometallic perovskite, electron and hole transporting materials in solar cell take expensive and complex processes, limiting the potential of organometallic perovskite photovoltaics.   Therefore, further modification steps for materials and device should be proposed to overcome the current limitation.

In Chapter 1, basic understanding of organometallic perovskite and solar-cell physics are discussed.   It includes theoretical study of material design and functional mechanism of solar cells by physicochemical perspectives, and discuss the pioneered researches to improve the optoelectronic property of solar cells. Moreover, general principles of material and device degradation with established strategy will be handled to follow the general principle of organometallic perovskite research.

In Chapter 2, ideal process and synthesis of organometallic perovskite solar cells are covered.   In early 2014, chlorine-doped perovskite has gather the much attentions due to the passivating effect of chlorine in a perovskite lattice.   Chlorine (Cl) doping not just improve the PCE of the device, but also enhance the stability. However, the detailed reaction process wasn't defined clearly, which could provide an additional room for the further optimization.   To understand the reaction steps and formation of Cl-doped perovskite, different synthesis and deposition techniques were studied.   Therefore, the extent of reaction was controlled to observe the intermediate phases during the reaction, and we have further utilized them to create the highly stable and efficient material synthesis.   At the end, stable solar cell was fabricated by using newly created perovskite.

In Chapter 3, synthesis and fabrication of electron transporting (n-type) material are discussed.   Metal oxide are widely used as an n-type layer, and

deposition and synthesis require complex processes to make a high quality film. Vacuum and solution depositions are two typical method for *n*-type layer, and individual deposition has problem on a rough transparent-conducting oxide (TCO) substrate (*n-i-p* structured device). Also, the growth of perovskite can be hindered by the quality of *n*-type layer, requiring further improvement. Therefore, combinational strategy of vacuum and solution processes has conducted to provide the extreme compact *n*-type layer, improving the performance of device.

In Chapter 4, degradation issue of organometallic perovskite under light, heat, and water are investigated. Organic site of organometallic perovskite roles the main terminal for degradation, which will be studied and modified to resolve the instable behavior of organometallic perovskite (methylamonium (MA) or formamidinium (FA)). Also, optoelectrical property of organometallic perovskite will be discussed to develop the ideal methodology of organometallic perovskite design. Especially, organic cation with multiamine based aromatic compound is ideally utilized as a solute of organometallic perovskite. Distinctive structure of aromatic compound obtains delocalized π-bonds exhibiting superior optoelectronic property with sensational stability to resolve the stabilities of material and device. Therefore, chemistry and design theory of organometallic perovskite will be discussed deeply.

In Chapter 5, stability and cost of *n*-type layer (metal oxide) are discussed. In most of cases, metal oxide produces photocatalytic reaction during the illuminating condition, leading unexpected degradation of solar cells. Therefore, progress for developing efficient and stable electron transporting materials will be

handled with the detailed study.   Moreover, metal oxides require high temperature process to obtain the proper electron mobility, requiring high cost to fabricate. Therefore, low-temperature synthesis of metal oxide for efferent device will be handled in this chapter.

In Chapter 6, combinational strategy of perovskite chemistry are covered. Organometallic perovskite chemistry obtains organics, post transition metal, and halides, where the organic site role as the main terminal for perovskite degradation. Organics share hydrogen bonding within a lattice, which is weak enough to break under high energy or polar environment.   Therefore, the interaction of organics is fully engineered by substituting alkali metal to form a covalent bond and low-dipole organics to stabilize the material.   While the material has engineered, optoelectrical and thermodynamic property of organics and metal are once more understood to create the efficient and stable device.

Keywords: Solar cells, organometallic perovskite, compositional engineering, solvent, cation, anion, electron transporting material, hole transporting material, stability, polymer, metal oxides, hybrid material, deposition process, recombination, defect, electronic trap.

Student Number: 2013-23817

Table of Contents

List of Figures

Chapter 1.

Chapter 2

Chapter 3

Chapter 4

Chapter 5

Chapter 6

List of Tables

Chapter 1

Chapter 2

Chapter 3

Chapter 4

Chapter 5

Chapter 6

Chapter 1.

Overview of Perovskite Photovoltaics

1.1 Operation Mechanism of Solar Cells

The solar cell functions with the photovoltaic effect, converting light energy into charges to generate an electricity. This type of energy conversion is cost-effective and clean approach to support the energy consumption. The basic principle for solar energy conversion is shown in Fig. 1-1. The solar cell consists *n*-type and *p*-type material, which collect and transport the electrons and holes generated from a light absorbing material. Electrons and hole pair generates from the incident photon has a greater bandgap of the material. Simply, the incident light comes through the transparent conducting oxide (TCO), light absorbing material produces hole and electron pair to generate the electricity by the electric field existing at the *p-n* junction [1,2]. In order to generate hole and electron pair efficiently, bandgap of light-absorbing material should satisfy the solar spectrum as shown in Fig. 1-2. Therefore, the bandgap between 1.2~1.5 eV can be called as a proper material for photo-induced charge generating material [3-5].

The performance of solar cell is defined as power conversion efficiency (PCE), defining by the multiplication of short-circuit current (*Jsc*), open-circuit voltage (*Voc*), and fill factor (FF). While the solar cell is in the operating situation, as shown in Fig. 1-1, the incident light or photons are

absorbed by light harvesting material, producing photo-exited electrons and holes, which will be utilize as current density. In order to obtain high *Jsc*, bandgap of light harvesting material must be small enough to absorb much of incident light. However, PCE isn't the single component of *Jsc*, requiring *Voc* and fill factor (FF) to generalize the device performance. PCE is defined as *Jsc* X *Voc* X FF, where the *Voc* can be determined by the quasi-fermi difference of material, requiring high and proper bandgap and band alignment, Therefore, bandgap should be optimized to exhibit the both high *Voc* and *Jsc* (details are shown in Fig. 1-3) [6].

Performance of single-junction photovoltaic can be examined by the Shockley and Queisser limit, regarding on the one-sun efficiency by using the bandgap of light-absorbing material [2,7]. Throughout the extensive works, as shown in Fig. 1-4, different types of solar cell material are approaching its limit, requiring further strategy to compete against the energy market [2]. Therefore, the tandem structured device has introduced to overcome the limit, using the high bandgap and low bandgap material to boosts the limit of single-junction cell [8-10]. The structure of tandem solar cell can be separated into two different parts, two-terminal and four-terminal cells (Fig. 1-5), requiring may room to utilize the process and material for future uses [8]. Moreover, multi-junction solar cell can be designed to explore the potential of photovoltaics.
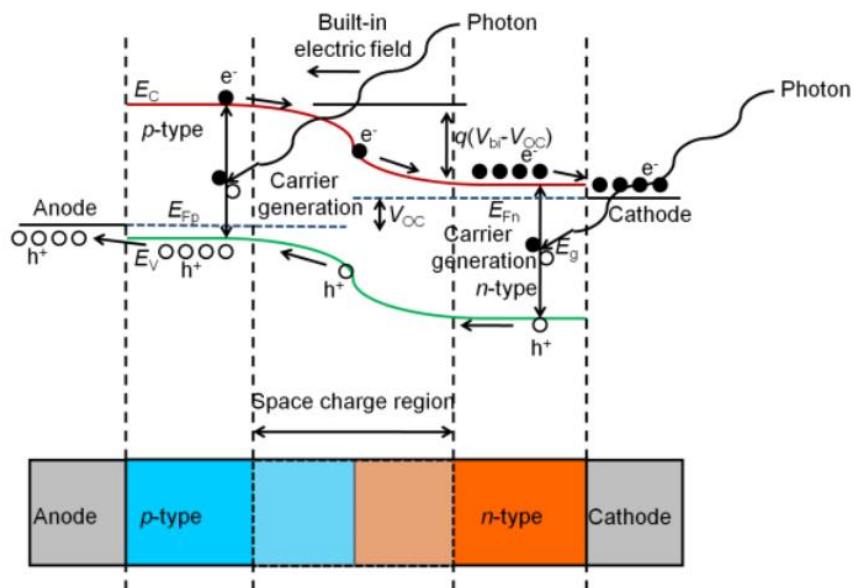
Fig. 1-1.   Energy-band diagram of a silicon *p-n* junction solar cell.   From Ref. [1].
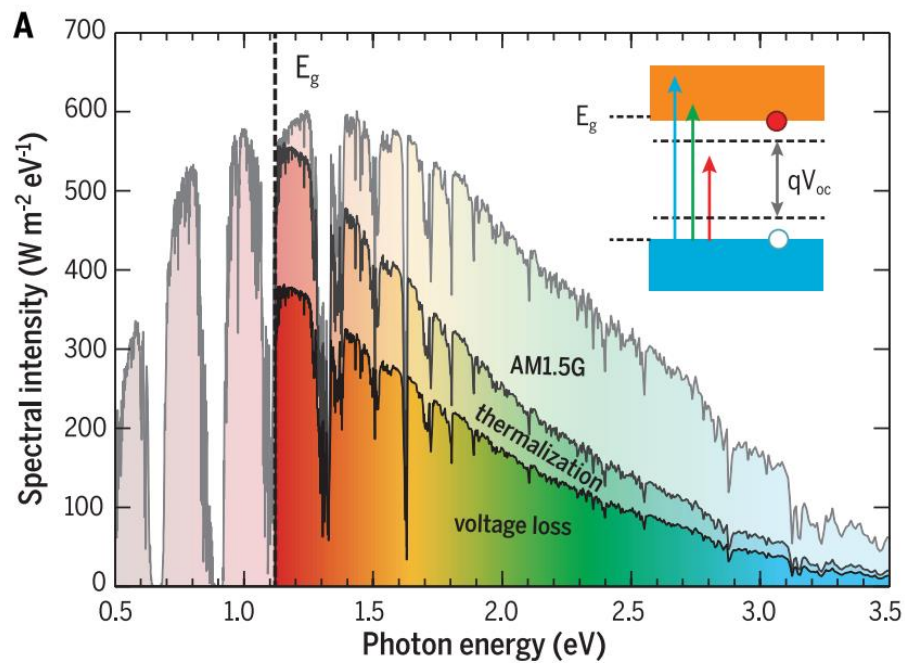
Fig. 1-2. Solar spectrum and the energy production of light-induced solar cells. From Ref. [3].
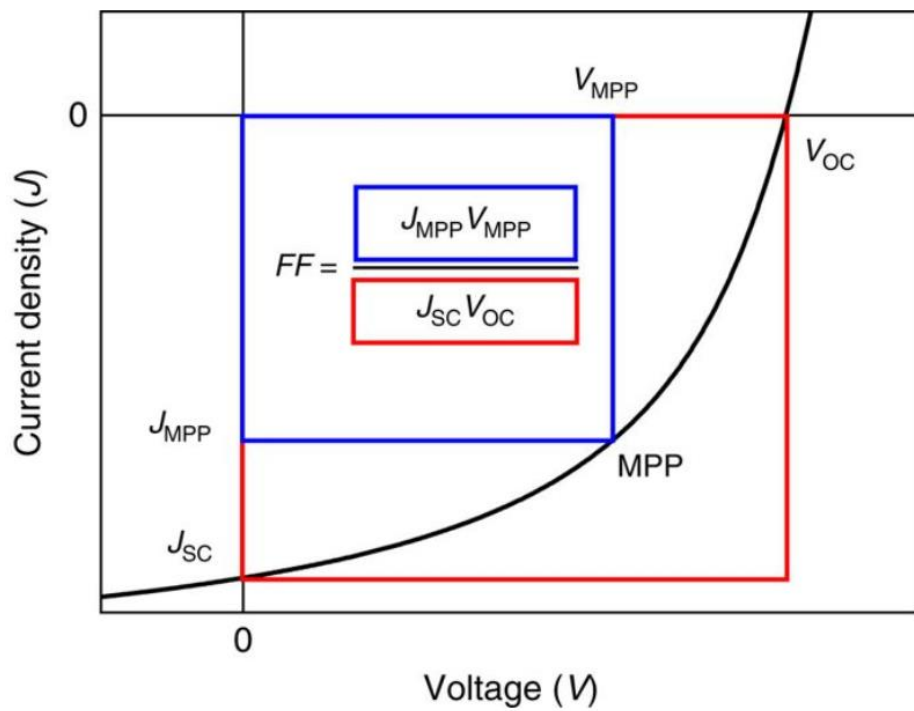
Fig. 1-3. *J-V* characteristic and factors in solar cells. From Ref. [6].
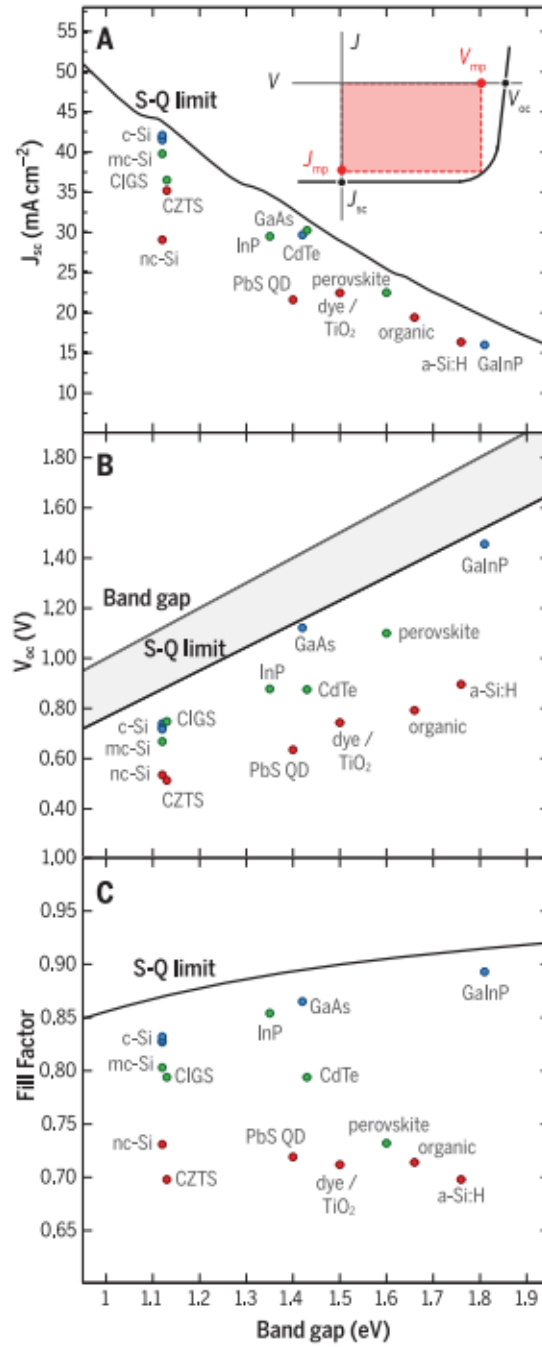
Fig. 1-4. Plots for recorded solar cell efficiencies and *S-Q* limit. From Ref. [3].
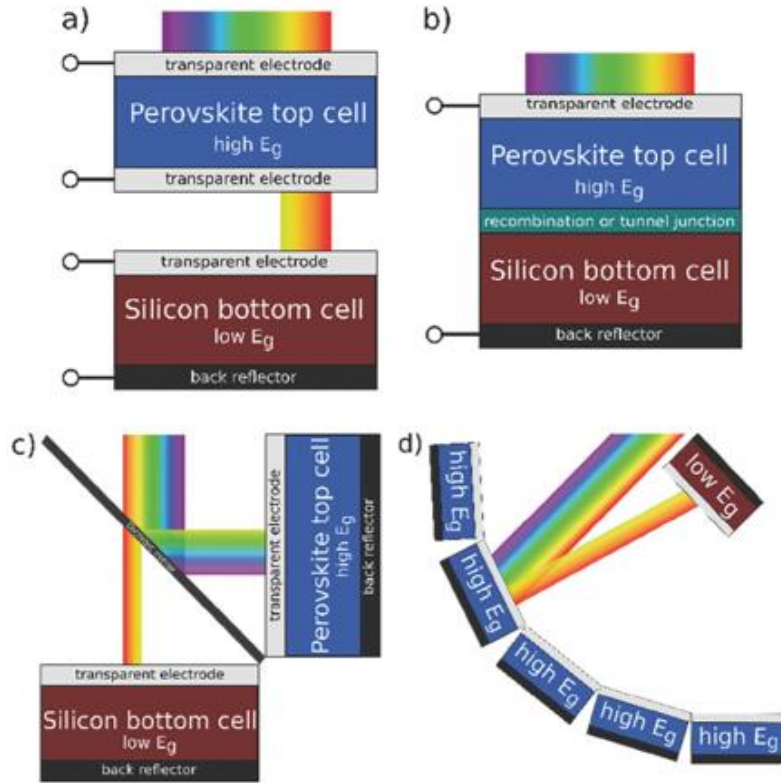
Fig. 1-5. (a) 4-terminal, (b) 2-terminal, (c) four-terminal optical spectral splitting, and (d) four-terminal reflective tandem solar cells. From Ref. [8].

1.2 Application of Perovskite in Solar Cells

Perovskite can be formed in many different types, such as oxide-based or organometallic perovskite, and the organometallic perovskite can be utilized efficiently due to its suitable bandgap and physical properties [11-14]. Also the cost of perovskite is very cheap and the deposition can be easily done below 100°C, allowing the strong advantage in a market competition. General chemistry of organometallic perovskite consists ABX_3, where A is $CH_3NH_3^+$ (MA), $CN_2H_5^+$ (FA) or Cesium, B is Pb^{2+} or Sn^{2+}, and X is I^- or Br^- (as shown in Fig. 1-6), and the property of material can be largely changed by the combination of A, B, and X [15,16]. In most of cases, many works utilized $MAPbI_3$ or $FAPbI_3$ framework to the solar cell due to the suitable property, but Br or Sn is often use as solute to stabilize or improve the device, which will be discussed in Chapter 1-5.

Application of organometallic perovskite is firstly demonstrated by Miyasaka group in 2009 with the 3.8% of PCE. Within 10 years of researches PCE is boosted to 24.2%, which is competitive against the commercialized Si-based solar cells [2,17-19]. Perovskite solar cells obtains transparent conducting oxide (TCO) / *n*-type layer / perovskite/ *p*-type layer / gold, and the early version of device used liquid based *p*-type electrolyte, leading extremely poor stability (as shown in Fig. 1-7), but the utilization of solid *p*-type and encapsulation techniques lead the improvement of solar cell stability [20,21]. Also, the different types of architecture (inverted structure) has also explored to widen the application of materials and processes [22]. Moreover the depositions of individual layers were widely studied

to obtain high PCE and stability [23].

The perovskite material obtains superior intrinsic properties such as high absorption coefficient and low defect density with the ambipolar charge transport property, leading the highly performable device as shown in Fig. 1-8 [24,25]. Moreover, the bandgap of perovskite can be tunable from 1.2 eV to 2.3 eV by substitution of different ion in perovskite chemistry [as prensted in Fig. 1-9]. These facts are highly important because tunable bandgap allows the application of tandem solar cells and other displays, widening the study and application of perovskite [26].
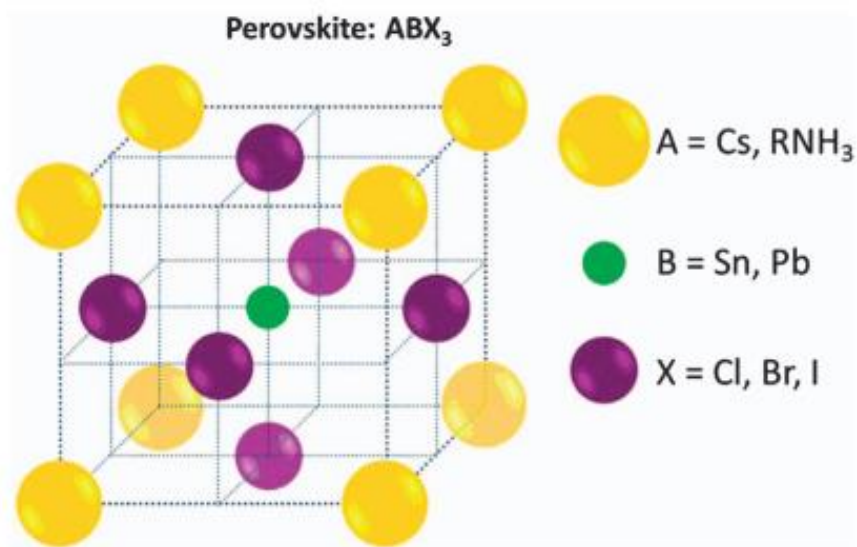
Fig. 1-6.   Schematic representation of the organometallic perovskite with species

A, B and X.   From Ref. [15].
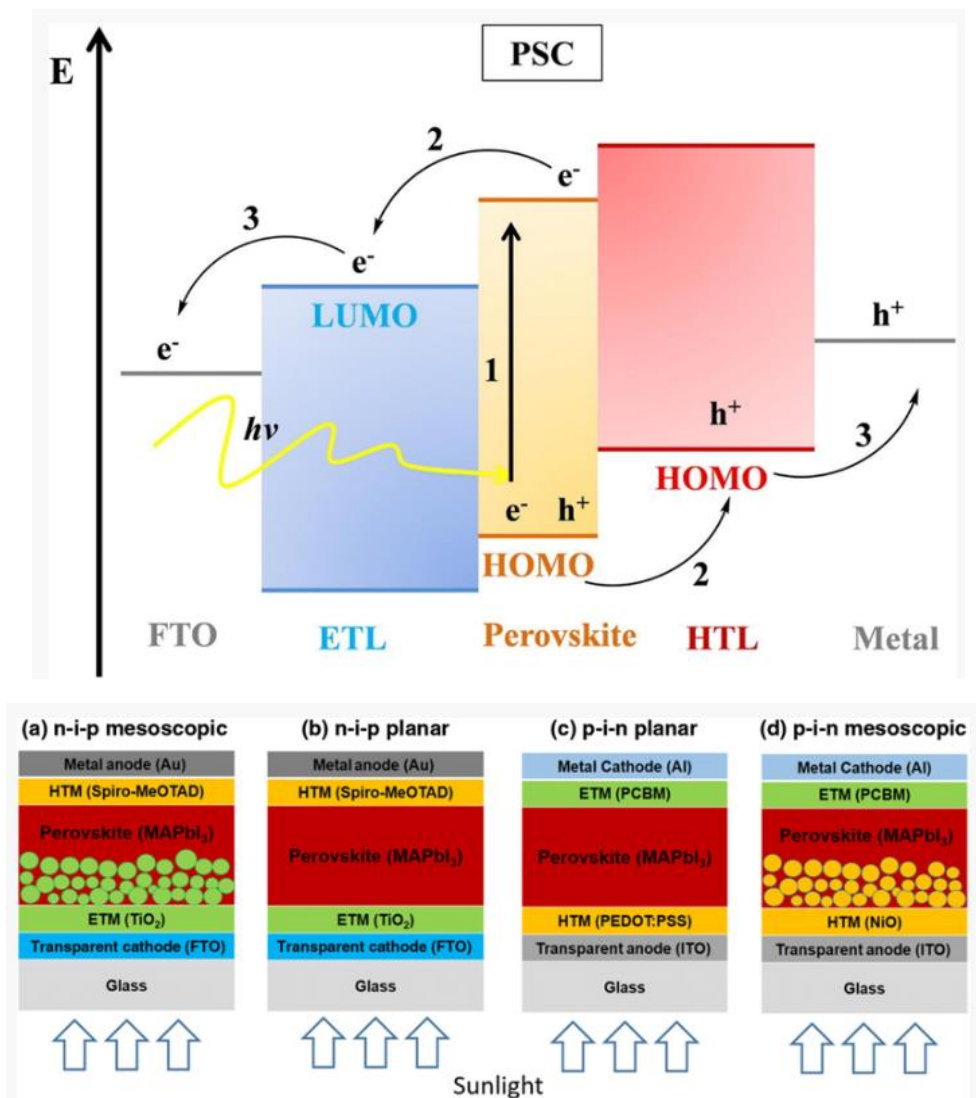
Fig. 1-7.   Band diagram of perovskite solar cells with the different device architectures and materials.   From Ref. [22].
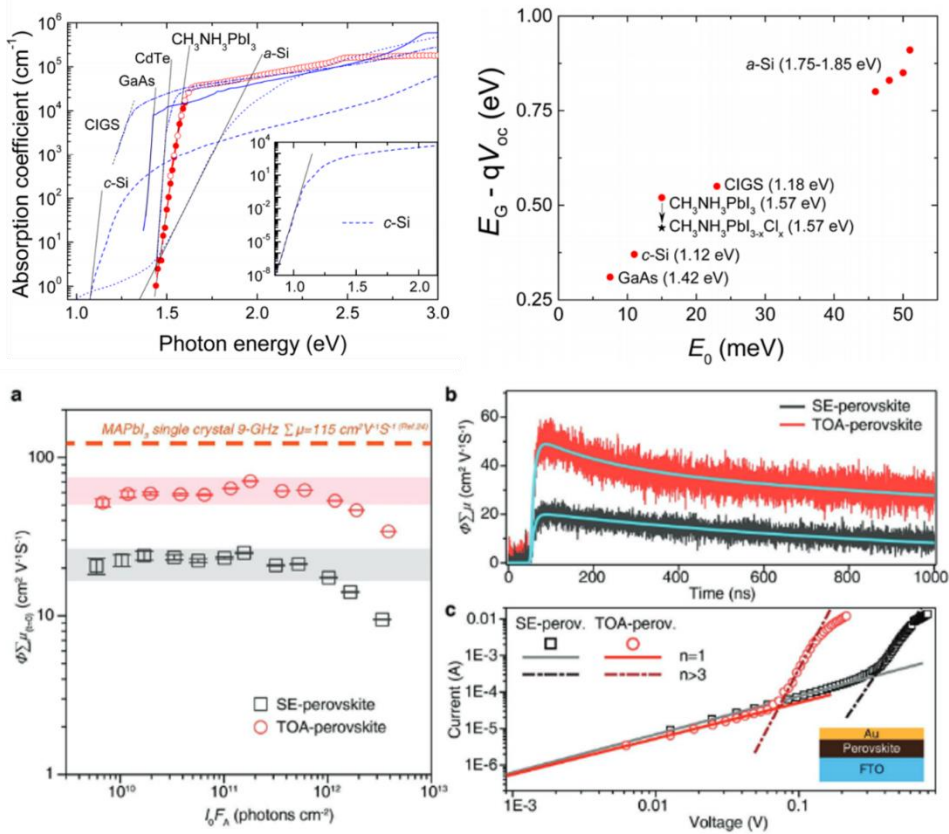
Fig. 1-8.   Absorption coefficient and relation between Urbach energy of various solar cell materials.   Charge mobility and defect of perovskite.   From Ref. [25].
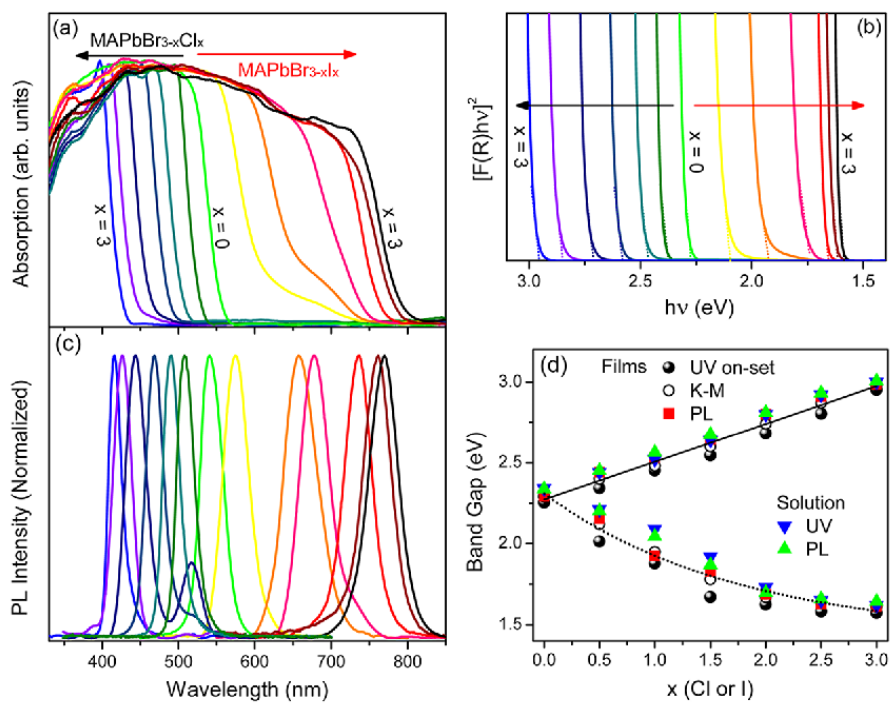
Fig. 1-9.   Tunable bandgap of perovskite by halide exchange.   From Ref. [26].

1.3 Deposition of Perovskite Photovoltaics

Fabrication of perovskite photovoltaics requires the deposition of *n*-type layer, perovskite, *p*-type layer, and gold on a TCO substrate. In general, deposition of *n*- or *p*-type material on a TCO goes first (depends on *n-i-p* or *p-i-n* structure, where *i* indicates perovskite layer), then deposit perovskite on an *n*- or *p*-type layer next. After, deposit the remaining *n*- or *p*-type material on the perovskite layer. Lastly, deposit the counter electrode (gold) to finish up the solar cell fabrication. Majorly, vacuum and solution processed depositions were widely introduced to utilize the efficient layer (simple schematic shown in Fig. 1-10) [27]. To make a complete device, both vacuum and solution depositions are required, but the process cost should be considered.

Solution deposition regularly separates into precursors and nanoparticles. Precursor deposition is the deposition of reactant and add the thermal or external inputs to complete the reaction, then the creation of grain nucleation occur on a substrate as shown in Fig. 1-11 [28]. Precursor deposition is highly preferable to make a uniform and compact film, but the external input, such as heat or chemical can damage other layers such as TCO, *n*-, perovskite, or *p*-type layers [29]. Therefore, precursor deposition is generally preferable for the low temperature synthesis and the non-reactive substrate. On the other hand, nanoparticle deposition is quite direct. After synthesize the material, those material are dilute into the dispersive solvent, then deposit on a substrate to complete the film fabrication. Even though the temperature should applied to evaporate the

dispersive solvent, the temperature isn't very high [30]. However, nanoparticle deposition is quite limited to make a high quality film. Nanoparticle deposition has to consider the size of nanoparticle and adhesion energy between the substrate and material during the deposition, and also the property of dispersive solvent because it can vary the quality of film. Therefore, solution based deposition should be carefully carried out to make a high quality film.

Vacuum deposition is theoretically the best option for the film deposition due to the clean and slow processes. Majorly, sputtering, evaporation, and atomic layer depositions (ALD) are the main depositions in the fabrication of perovskite photovoltaics [28-30]. Although atomic layer deposition is known for the fabrication of ideal deposition, the process and costs are slow and expensive. Also the temperature cannot go high, limiting the synthesis of metal oxides (those require high temperature to fabricate). On the other hand, sputter is suitable to deposit metal oxides by applying plasma energy, but the sputtering damage is too strong, diminishing the substrate [31]. Lastly, thermal evaporation suitable for the deposition of metal oxides or organometallic system but the uniformity of film is poor. Regardless on the advantages and disadvantage of vacuum depositions, the process cost is highly expensive when it was compared with cost of solution process, requiring alternative solution to reduce cost and improve the quality of film [29].
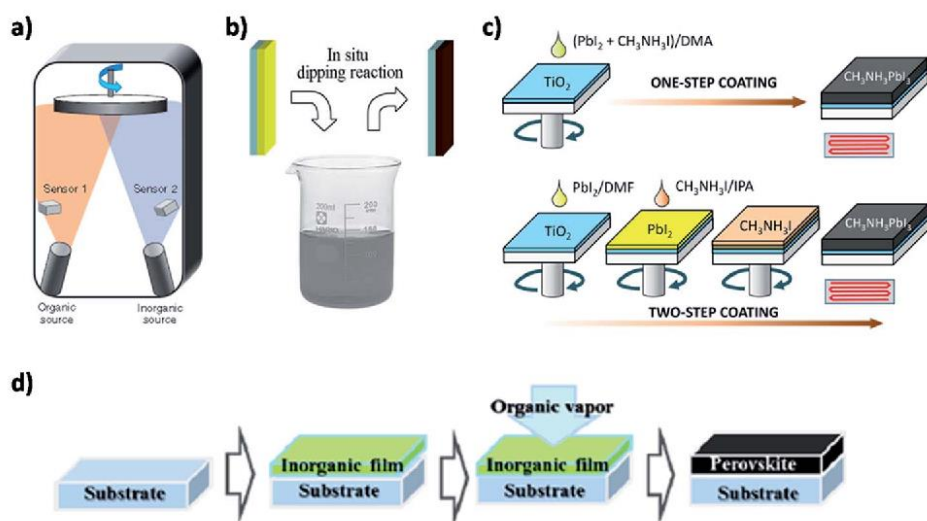
Fig. 1-10.   (a) Vacuum, (b) and (c) solution process, and combination of vapor and

solution depositions of perovskite film.   From Ref. [27].
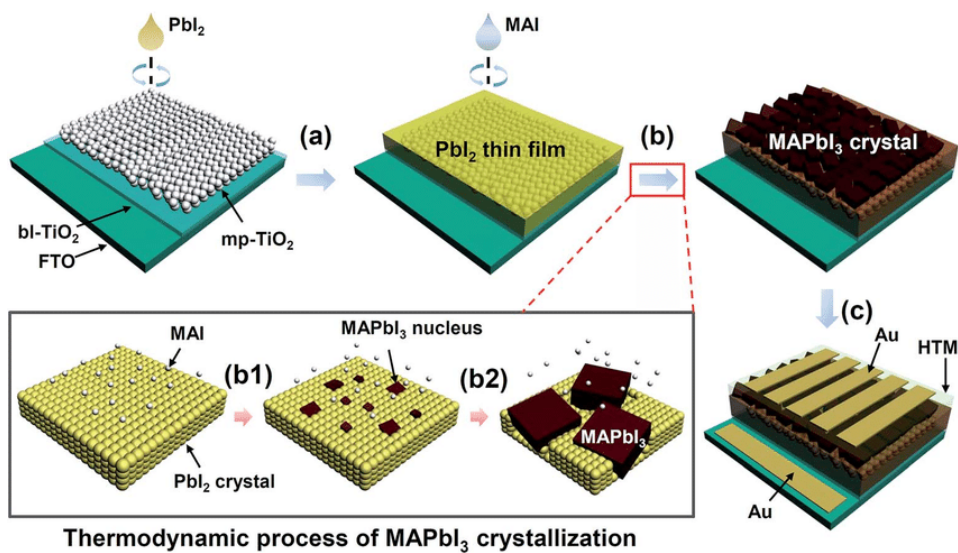
Fig. 1-11.   Thermodynamic nucleation of precursor-processed perovskite (MAPbI$_3$).   From Ref. [28].

1.4 Degradation Issues in Perovsktie Solar Cells.

Perovskite photovoltaics established enormous PCE growth within 6 years, and settled as strong candidate as a next generation photovoltaics. However, the perovskite solar cell obtains major issue for the commercialization, which is the stability. While the solar cell is in the operating conditions, the device is exposed under an ambient and illuminating conditions. Ambient condition can be extreme, such as high temperature conditions or humid conditions, leading the damages of materials and solar cells. Also illumination produces latent heat, causing the additional problem in solar cell stability.

As discussed, perovskite solar cell consists *n*-type, perovskite, and *p*-type material (assume that TCO and Au are stable). Among the various degradation factors, humidity is directly related to the degradation of organometallic perovskite. Organometallic perovskite obtains organic site, such as FA and MA, and those ions form an oxygen bonding with the skeletal structure of metal halide. When the water atom attacks the organometallic perovskite, organic cation interacts with cation to ruin the structure of perovskite (as shown in Fig. 1-12) [32,33]. Moreover, organic site of organometallic perovskite reactive in aqueous solution, which causes the serious problem in solution manufacturing process.

Heat is also the main factor in the degradation of perovskite solar cells. Organometallic perovskite obtains organic compound and it is very volatile, which easily dissociate from the perovskite structure when the heat is induced (as shown in Fig. 1-13) [34,35]. Moreover, heat-induced degradation is also related to the

stability of *p*-type organics.   Polymer or small organics were widely used as *p*-type material.   Those organic compounds obtains low hole-mobility compared to the inorganic compound, requiring doping of metal with additives [36,37].   When the heat is induced, as shown in Fig 1-14, dopant and additives staring to evaporate and react with the perovskite layer, resulting in the destruction of the device.

　　　Light is also the major issue in the degradation of perovskite solar cells. When the light comes in through the TCO, it react with metal oxide (majorly) or perovskite layer.   Most of metal oxide has photocatalytic activity, making the oxygen radical inside of layer, and produced oxygen radical make a reaction with the organic site of perovskite to form a gaseous phase to damage the overall devices (shown in Fig. 1-15) [38,39].   Not only the issue of metal oxide layer, but also the perovskite itself has a problem with the light.   When the device is exposed under the illuminating condition, gas evolution of organic halides and hydrogen halide starts to occur, leading the degradation of perovskite and solar cells, which shown in Fig. 1-16 [40].

　　　Although the perovskite had a significantly showed the potential as a next generation photovoltaics, management of surrounding attack should be handled for the future commercialization.   There were many establishment has made to sustain long-term stability, yet the intrinsic property of organic part of perovskite and *n*- or *p*-type layer should be further investigated to compete against the other types of solar cells.
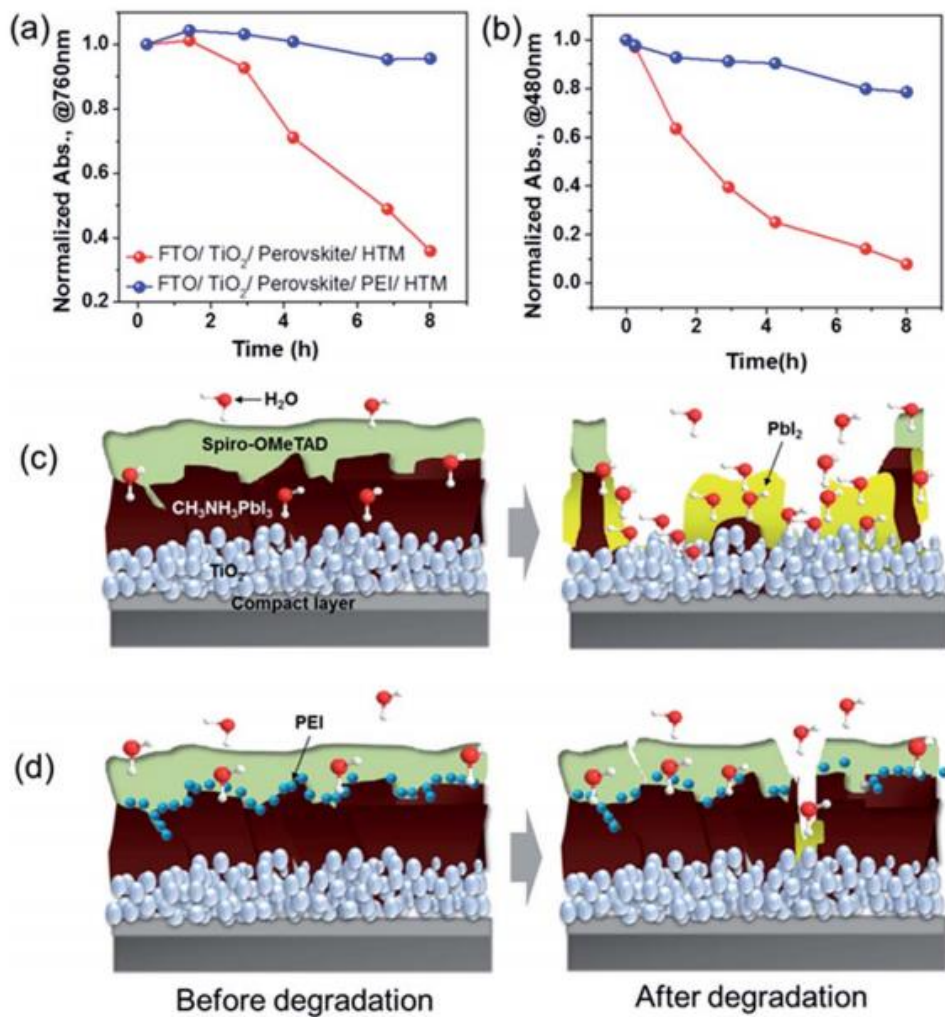
Fig. 1-12.　(a-c) Water-induced degradation of perovskite layer, and (a,b,d) the

passivation layer to block the water damage.　　From Ref. [32].
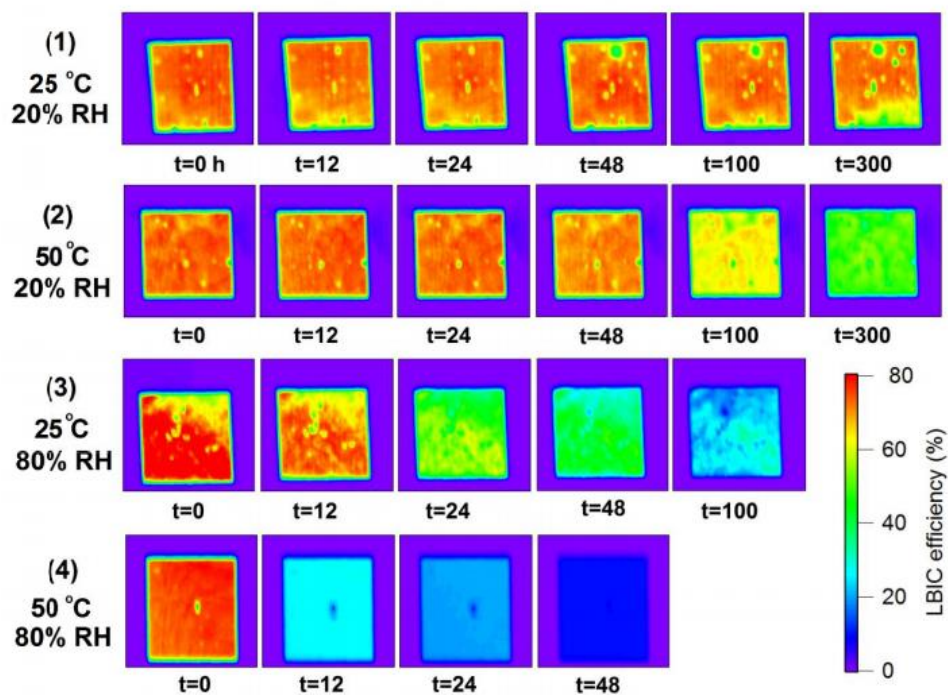
Fig. 1-13.　Evolution of LBIC mapping of perovskite at the different temperature and relative humidity.　From Ref. [35].
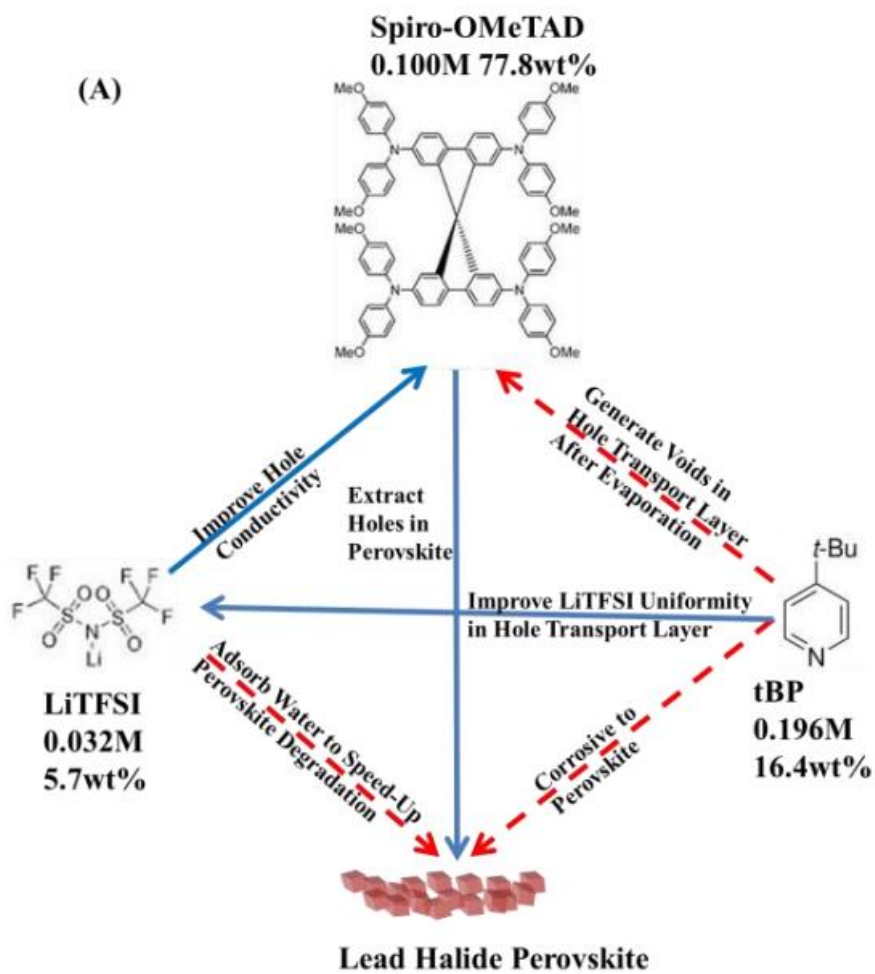
Fig. 1-14.   Degradation mechanism of metal doped Spiro-OMeTAD.   From Ref. [36].
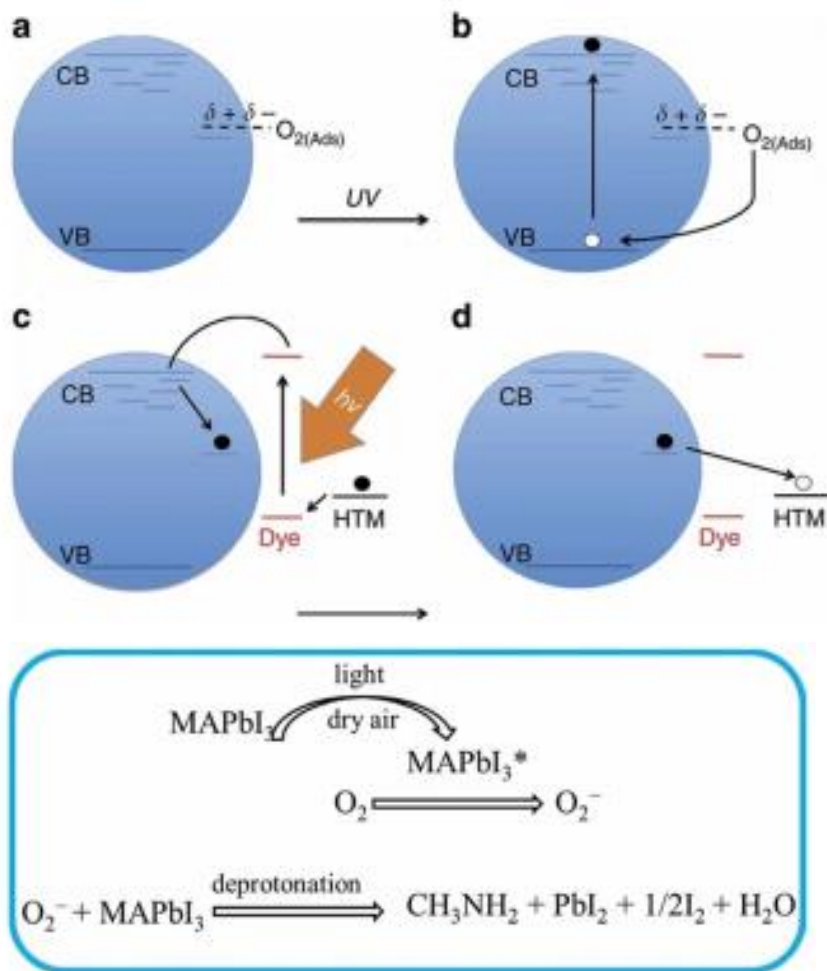
Fig. 1-15. Degradation mechanism of photocatalyzed metal oxide and perovskite.

From Ref. [38].
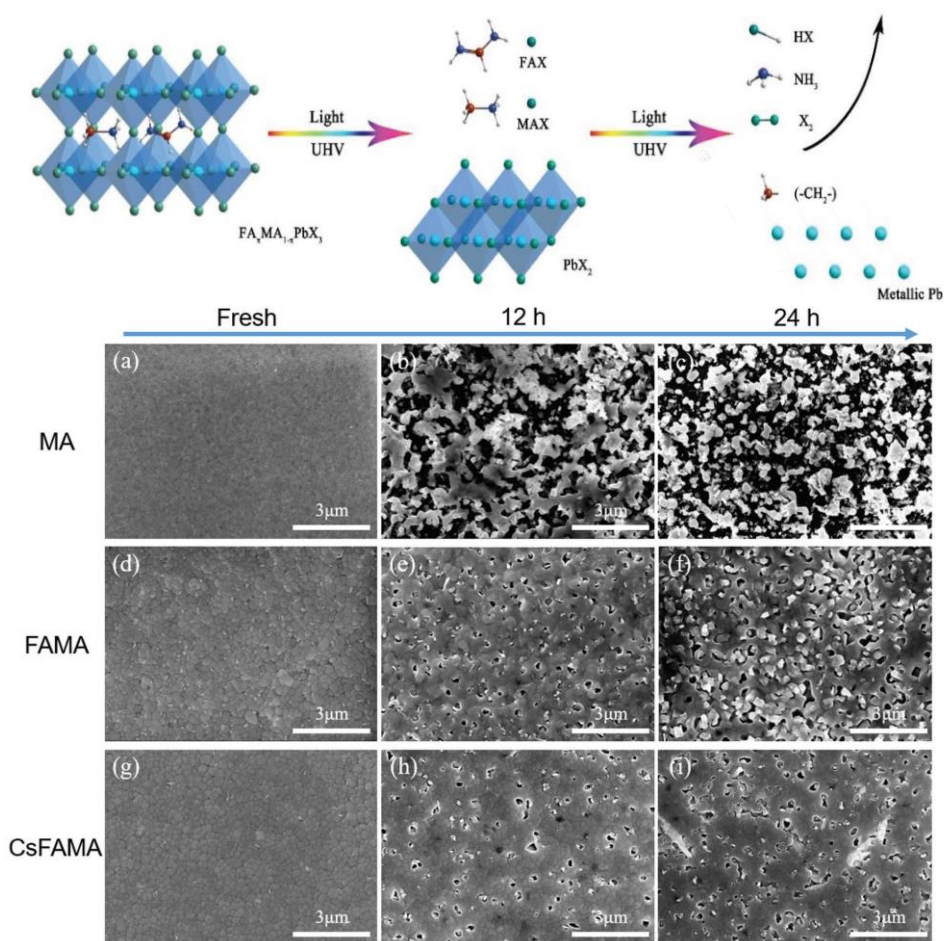
Fig. 1-16.　Light-induced degradation of perovskite.　From Ref. [40].

1.5 References

1. M. Shanawani, D. Masotti, and A. Costanzo, "THz Rectennas and Their Design Rules," *Electronics*, **6**, 99 (2017).

2. S. C. Jain, E. L. Heasell, and D. J. Roulston, "Recent Advances in the Physics of Silicon P-N Junction Solar Cells Including Their Transient Response," *Prog. Quant. Electr.* **11**, 10 (1987).

3. A. Polman, M. Knight, E. C. Garnett, B. Ehrler, and W. C. Sinke, "Photovoltaic Materials: Present Efficiencies and Future Challenges," *Science*, **352**, 6283 (2016).

4. D. Mühlbacher, M. Scharber, M. Morana, Z. Zhu, D. Waller,.R. Gaudiana, and C. Brabec, "High Photovoltaic Performance of a Low-Bandgap Polymer," *Adv. Mater.***18**, 2884 (2006).

5. M. A. Contreras, L. M. Mansfield, B. Egaas, J. Li, M. Romero, R. Noufi, E. Rudiger-Voigt, and W. Mannstadt, "Wide Bandgap $Cu(In,Ga)Se_2$ Solar Cells with Improved energy Conversion Efficiency," *Prog. Photovolt: Res. Appl.* **20**, 843 (2012).

6. D. Bartesaghi, I. d. C. Pérez, J. Kniepert, S. Roland, M. Turbiez, D. Neher, and L. J. A. Koster, Competition between Recombination and Extraction of Free Charges Determines the Fill Factor of Organic Solar Cells," *Nat. Commun*. **6**, 7083 (2015).

7. W. Shockley, and H. J. Queisser, "Detailed Balance Limit of Efficiency of *p-n* Junction Solar Cells," *J. of Appl. Phys*. **32**, 3 (1961).

8. J. Werner, B. Niesen, and C. Ballif, "Perovskite/Silicon Tandem Solar Cells: Marriage of Convenience or True Love Story? – An Overview," *Adv. Mater. Interfaces* **5**, 1700731 (2018).

9. G. E. Eperon, T. Leijtens, K. A. Bush, R. Prasanna, T. Green, J. T.-W. Wang, D. P. McMeekin, G. Volonakis, R. L. Milot, R. May, A. Palmstrom, D. J. Slotcavage, R. A. Belisle, J. B. Patel, E. S. Parrott, R. J. Sutton, W. Ma, F. Moghadam, B. Conings, A. Babayigit, H.-G. Boyen, S. Bent, F. Giustino, L. M. Herz, M. B. Johnston, M. D. McGehee, and H. J. Snaith, "Perovskite-Perovskite Tandem Photovoltaics with Optimized Band Gaps," *Science* **354**, 861 (2016).

10. M. Anaya, G.Lozano, M. E.Calvo, and H. Míguez, "ABX_3 Perovskites for Tandem Solar Cells," *Joule* **1**, 769 (2017).

11. M. D. McGehee, Materials science: Fast-Track Solar Cells. *Nature* **501**, 323 (2013).

12. G. Hodes, Perovskite-Based Solar Cells. *Science* **342**, 317 (2013).

13. C. S. Ponseca, T. J. Savenije, M. Abdellah, K. Zheng, A. Yartsev, T. Pascher, T. Harlang, P. Chabera, T. Pullerits, A. Stepanov, J.-P. Wolf, and V. Sundstrom, "Organometal Halide Perovskite Solar Cell Materials Rationalized: Ultrafast Charge Generation, High and Microsecond-Long Balanced Mobilities, and Slow Recombination," *J. Am. Chem. Soc*. **136**, 5189 (2014).

14. J. M. Frost, K. T. Butler, F. Brivio, C. H. Hendon, M. v. Schilfgaarde, A. Walsh, "Atomistic Origins of High-Performance in Hybrid Halide Perovskite Solar Cells," *Nano Lett*. **14**, 2584 (2014).

15. J. H. Rhee, C.-C. Chung, and E. W.-G. Diau, "A Perspective of Mesoscopic Solar

Cells Based on Metal Chalcogenide Quantum Dots and Organometal-Halide Perovskites," *NPG Asia Materials* **5**, e68 (2013).

16. Z. Fan, K. Sun, and J. Wang, "Perovskites for Photovoltaics: A Combined Review of Organic–Inorganic Halide Perovskites and Ferroelectric Oxide Perovskites," *J. of Mater. Chem. A* **3** 37 (2015).

17. A. Kojima, K. Teshima, Y. Shirai, and T. Miyasaka, "Organometal Halide Perovskites as Visible-Light Sensitizers for Photovoltaic Cells," *J. Am. Chem. Soc*. **131**, 6050 (2009).

18. National Renewable Energy Laboratory (NREL), Best Research-Cell Efficiencies, http://www.nrel.gov/ncpv/images/efficiency_chart.jpg (Accessed: 30th March, 2016).

19. P. K. Nayak, S. Mahesh, H. J. Snaith, and D. Cahen, "Photovoltaic Solar Cell Technologies: Analysing the State of the Art," *Nat. Rev. Mater.* **4**, 269 (2019).

20. J.-H. Im , C.-R. Lee , J.-W. Lee , S.-W. Park, and N.-G. Park, "6.5% Efficient Perovskite Quantum-Dot-Sensitized Solar Cell," *Nanoscale* **3**, 4088 (2011).

21. H.-S. Kim, C.-R. Lee, J.-H. Im, K.-B. Lee, T. Moehl, A. Marchioro, S.-J. Moon, R. Humphry-Baker, J.-H. Yum, J. E. Moser, M. Grätzel, and N.-G. Park, "Lead Iodide Perovskite Sensitized All-Solid-State Submicron Thin Film Mesoscopic Solar Cell with Efficiency Exceeding 9%," *Sci. Rep*. **2**, 591 (2012).

22. I. Hussain, H. P. Tran, J. Jaksik, J. Moore, N. Islam, M. J. Uddin, "Functional materials, device architecture, and flexibility of perovskite solar cell," *Emergent Materials* **1**, 133 (2018).

23. G. Grancini, C. Roldán-Carmona, I. Zimmermann, E. Mosconi, X. Lee, D. Martineau, S. Narbey, F. Oswald, F. De Angelis, M. Graetzel, and M. K. Nazeeruddin, "One-Year Stable Perovskite Solar Cells by 2D/3D Interface Engineering, *Nat. Commun*. **8**, 15684 (2017).

24. S. D. Wolf, J. Holovsky, S.-J. Moon, P. Löper, B. Niesen, M. Ledinsky, F.-J. Haug, J.-H. Yum, and C. Ballif, "Organometallic Halide Perovskites: Sharp Optical Absorption Edge and Its Relation to Photovoltaic Performance," *J. Phys. Chem. Lett.* **5**, 1035 (2014).

25. D. H. Kim, J. Park, Z. Li, M. Yang, J.-S. Park, I. J. Park, J. Y. Kim, J. J. Berry, G. Rumbles, and K. Zhu, "300% Enhancement of Carrier Mobility in Uniaxial-Oriented Perovskite Films Formed by Topotactic-Oriented Attachment," *Adv. Mater*. **29**, 1606831 (2017).

26. D. M. Jang, K. Park, D. H. Kim, J. Park, F. Shojaei, H. S. Kang, J.-P. Ahn, J. W. Lee, and J. K. Song, "Reversible Halide Exchange Reaction of Organometal Trihalide Perovskite Colloidal Nanocrystals for Full-Range Band Gap Tuning," *Nano Lett*. **15** 5191 (2015).

27. T.-B. Song, Q. Chen, H. Zhou, C. Jiang, H.-H. Wang, Y. Yang, Y. Liu, J. You, and Y. Yang, "Perovskite Solar Cells: Film Formation and Properties," *J. Mater. Chem. A* **3**, 9032 (2015).

28. N. Ahn, S. M. Kang, J.-W. Lee, M. Choi, and N.-G. Park, "Thermodynamic Regulation of $CH_3NH_3PbI_3$ Crystal Growth and its Effect on Photovoltaic Performance of Perovskite Solar Cells," *J. Mater. Chem. A* **3**, 19901 (2015).

29. J. Kim, T. Hwang, S. Lee, B. Lee, J. Kim, J. Kim, B. Gil, and B. Park, "Synergetic Effect of Double-Step Blocking Layer for the Perovskite Solar Cell," *J. Appl. Phys.* **122**, 145106 (2017).

30. A. J. Yun, J. Kim, T. Hwang, and B. Park, "Origins of Efficient Perovskite Solar Cells with Low-Temperature Processed SnO_2 Electron Transport Layer," *ACS Appl. Energy Mater.* **2**, 3554 (2019).

31. J. Sundberg, R. Lindblad, M. Gorgoi, H. Rensmo, U. Jansson, and A. Lindbla, "Understanding the Effects of Sputter Damage in W–S thin films by HAXPES," *Appl. Surf. Sci.* **305**. 203 (2014).

32. J. H. Yun, I. Lee, T.-S. Kim, M. J. Ko, J. Y. Kim, and H. J. Son, "Synergistic Enhancement and Mechanism Study of Mechanical and Moisture Stability of Perovskite Solar Cells Introducing Polyethylene-Imine into the $CH_3NH_3PbI_3$/HTM Interface," *J. Mater. Chem. A* **3**, 22176 (2015).

33. X. Dong, X. Fang, M. Lv, B. Lin, S. Zhang, J. Ding, and N. Yuan, "Improvement of the Humidity Stability of Organic–Inorganic Perovskite Solar Cells using Ultrathin Al_2O_3 Layers Prepared by Atomic Layer Deposition," *J. Mater. Chem. A* **3**, 5360 (2015).

34. E. J. Juarez-Perez, L. K. Ono, M. Maeda, Y. Jiang, Z. Hawasha, and Y. Qi, "Photodecomposition and Thermal Decomposition in Methylammonium Halide Lead Perovskites and Inferred Design Principles to Increase Photovoltaic Device Stability," *J. Mater. Chem. A* **6**, 9604 (2018).

35. Z. Song, S. C. Watthage, A. B. Phillips, and G. K. Liyanage, "Investigation of

Degradation Mechanisms of Perovskite-Based Photovoltaic Devices using Laser Beam Induced Current Mapping," *Proc. of SPIE* **9561** 956107 (2015).

36. S. Wang, Z. Huang, X. Wang, Y. Li, M. Günther, S. Valenzuela, P. Parikh, A. Cabreros, W Xiong, and Y. S. Meng, "Unveiling the Role of tBP–LiTFSI Complexes in Perovskite Solar Cells," *J. Am. Chem. Soc.* **140**, 16720 (2018).

37. A. K. Jena, M. Ikegami, and T. Miyasaka, "Severe Morphological Deformation of Spiro-OMeTAD in $(CH_3NH_3)PbI_3$ Solar Cells at High Temperature," *ACS Energy Lett.* **2**, 1760 (2017).

38. B. Li, Y. Li, C. Zheng, D. Gao, and W. Huang, "Advancements in the Stability of Perovskite Solar Cells: Degradation Mechanisms and Improvement Approaches," *RSC Adv.* **6**, 38079 (2016).

39. C. Wang, B.-Q. Xu, X. Wang, and J. Zhao, Preparation and Photocatalytic Activity of $ZnO/TiO_2/SnO_2$ Mixture, *J. of Solid State Chem.* **178**, 3500 (2005).

40. J. Yang, Q. Hong, Z. Yuan, R. Xu, X. Guo, S. Xiong, X. Liu, S. Braun, Y. Li, J. Tang, C. Duan, M. Fahlman, and Q. Bao, "Unraveling Photostability of Mixed Cation Perovskite Films in Extreme Environment," *Adv. Optical Mater.* **6**, 1800262 (2018).

Chapter 2.

Solvent and Intermediate Phase as Boosters for the Perovskite Transformation and Solar Cell Performance

2.1. Introduction

The feasible challenges in solar cell commercialization are enhancement in power conversion efficiency (PCE) and cost reduction to support the world-wide electricity consumption [1–5]. Alternatively, organometallic perovskite solar cells were first demonstrated by Miyasaka's group in 2009 with a PCE of 3.8% [6], and an enormous growth has been achieved over the last 6 years with the highest efficiency of 22.10% [7]. Perovskite ($CH_3NH_3PbI_3$) solar cells are settled as the most attractive topic in photovoltaic research areas due to the low fabrication cost and high efficiencies, followed by inherent advantages of the perovskite material which include an appropriate and direct bandgap, small exciton binding energy, balanced ambipolar charge transport properties, etc. [8–12]. Furthermore, the synthesis of $CH_3NH_3PbI_3$ ($MAPbI_3$) goes through a simple process, by mixing PbI_2 and MAI precursors [6]. In 2012, the superior performance via $MAPbI_3$ synthesis with $PbCl_2$ and MAI precursors was introduced by Snaith's group, and property analyses were carried out by many groups [13–16]. Since then, researchers widely studied the chlorine effect, and concluded that chlorine enhances the morphology of perovskite films [16–20]. Even though the chlorine effect is suggested by many research groups, understanding the mechanisms on the synthesis is still required to

be elucidated.

Architectural challenges are widely studied due to the ambipolar behavior [21–23] of perovskites. Among them, the highest efficiency of 22.10% [7] has been achieved with mesoporous structure, and mesoporous layer allows the additional light trapping effect [24,25]. In the mesoscopic structure, there are two major $MAPbI_3$ deposition methods. The one-step solution deposition generally uses a mixture solution of PbI_2 and MAI [16], and the sequential deposition is carried out by pre-depositing the PbI_2 film, followed by dipping it into an MAI-dissolved iso-propanol solution to form the $MAPbI_3$ film [26]. Among them, the one-step solution deposition is highly beneficial in that this process is quite simple and time-saving. However, the sequential deposition is reported with a higher PCE than that of the one-step deposition [27–29] due to the enhanced pore filling through the mesoporous TiO_2 (mp-TiO_2). Although the sequential deposition guarantees a high PCE, a comparative disadvantage in the sequential deposition is that it is a long-time process, since it goes through multiple steps to fabricate the perovskite film [26].

In this article, we have demonstrated a straightforward diffusion-controlled synthesis approach by replacing the conventional MAI-dissolved iso-propanol solution with a MAI-dissolved ethanol solution, which enhanced the crystallinity, boosted the perovskite transformation, and minimized impurities. Moreover, we have detected intermediate phases when the $PbCl_2$ precursor transforms into $MAPbI_3$, and engineered the $MAPbI_3$ deposition procedure by artificially mixing those intermediates as deposition precursors. This novel approach allowed superior surface morphology and crystallinity with enhanced conversion kinetics of $MAPbI_3$, yielding an initial PCE of 11.23% and notable stability exhibiting 10.14% PCE after 30 days under ambient conditions.

2.2. Experimental Section

Perovskite Solar Cell Fabrication. Fluorine-doped tin oxide substrate (FTO, TEC 8: Pilkington) was cleaned by sonication in Mucasol (Aldrich), ethanol (DEAJUNG), and DI water for 30 min sequentially. 50 nm of compact the TiO_2 blocking layer was deposited by spin-coating the mixture solution of 0.15 mM titanium diisopropoxide bis(acetylacetonate) (Aldrich) and 1-butanol (75.0 wt. % in iso-propanol, Aldrich) in 2500 rpm for 20 s followed by heating at 125°C for 5 min in an air oven. The same step was repeated with 0.3 mM concentration and the substrate was annealed at 500°C for 30 min. After the TiO_2 blocking layer was ready, TiO_2 pastes (ENB Korea) with 20 nm-sized nanoparticles were mixed with terpineol (Aldrich) in 1:2 ratio, followed by spin-coating at 4000 rpm for 30 s, yielding a ~350 nm thickness of the mp-TiO_2 layer. For the perovskite synthesis, MAI was first synthesized by following literature method [26]. 1.5 M $PbCl_2$ (Aldrich) was diluted in dimethyl sulfoxide (DMSO, Aldrich), and then MACl (Aldrich) was added with different concentrations (0, 0.5, 1.0, and 1.5 M) to synthesize the reaction 1, 2, 3, and 4 precursors where the reaction 1, 2, and 3 precursors contain both $MAPbCl_3$ and $PbCl_2$ phases, whereas the reaction 4 precursor contains only $MAPbCl_3$ ($MAPbCl^3$ forms by 1:1 molar stoichiometric ratios of MACl and $PbCl_2$). After the preparation of precursor mixture solutions, the solution was preheated at 100°C and the substrate was preheated at 150°C, then the solution was spin-coated at 2000 rpm for 5 s, followed by 6000 rpm for 5 s. The film was annealed at 150°C for 30 min, and cooled down in an ambient condition. After the film was cooled down, it was dipped into 20 mg/mL of MAI in an anhydrous ethanol solution (Daejung) for 20 min under ambient conditions (25°C and 55% humidity) and annealed at 100°C for 30min. The hole transport solution

was prepared by mixing 72.3 mg/mL of spiro-OMeTAD (Merck) in chlorobenzene (Aldrich) with 28.8 μL of tert-butylpyridine (Aldrich) and a 17.5 μL solution of 520 mg of lithium bis(trifluoromethylsyfonyl) imide salt (Aldrich) in 1mL acetonitrile (Aldrich) was spin-coated at 3000 rpm for 45 s. Finally, 100 nm thickness of an Au electrode was then thermally evaporated.

Device Characterizations. The morphologies of $MAPbI_3$ perovskite films were analyzed using scanning electron microscope (Normal-SEM, JSM-6360: Hitachi). The chlorine compositions and distribution were examined using energy-dispersive X-ray spectroscopy (EDS, ISIS-300: Oxford Instruments). The phases of the synthesized samples were characterized by X-ray diffraction (XRD, D8 Advance: Bruker). The photocurrent-voltage (J–V) curves of $MAPbI_3$ perovskite solar cells were obtained with a potentiostat (CHI 608C: CH Instrumental Inc.) under AM 1.5 illumination at 100 mW/cm^2 (K3000: McScience) with an active cell area of 0.09 cm^2. The field-emission scanning electron microscope (FE-SEM, Merlin-Compact: Carl Zeiss) was used to observe the plan and cross-sectional views. The absorption spectra of the $MAPbI_3$-deposited films were recorded on a UV-Vis spectrophotometer (Lambda 20: Perkin Elmer). Stability was measured every 5 days, and stored at 25°C with 55% of humidity under dark conditions.

2.3. Results and Discussion

2.3.1. Ethanol Conversion. Sequential deposition is one of the most preferable methods for perovskite fabrication due to the high PCE. One major problem, however, is the long fabrication time by multiple fabrication steps [26]. To reduce the fabrication time in the sequential deposition process, boosting the formation kinetics of $MAPbI_3$ using MAI with $PbCl_2$ precursors is required. Therefore, a low viscous solvent and larger concentration of MAI are necessary for effective diffusion of MAI into the $PbCl_2$ layer. In general, conventional dipping solution uses 10mg/mL of MAI in iso-propanol [26], and a high concentration of MAI in solvent reduces both cuboid sizes and PCEs [30]. Thus, finding an alternative solvent is necessary for the viscosity and diffusion aspects. Figure 2-1 schematically illustrates the movements of ionized MAI into the $PbCl_2$ film with ethanol (20mg/mL) and iso-propanol (10mg/mL), where the conversion kinetics of $PbCl_2$ into $MAPbI_3$ for each solvent is quite different even with the optical images (Fig. 2-2, fast conversion kinetics with MAI/ethanol). The extent of the reaction was easily estimated by color changes (E_g of $MAPbI_3 \approx 1.55$ eV). However, less viscous methanol was not effective due to the dissolution of $MAPbI_3$ (Fig. 2-3) [26]. The fabricated perovskite film with the same concentration (20 mg/mL) for the iso-propanol solution results in rather small cuboid sizes (~80 nm) with a low PCE of 2.08% in the solar cell performance, as shown in Fig. 2-4. The cuboid size of $MAPbI_3$ with an ethanol solution is also distinguishable from that with iso-propanol, as shown in the scanning electron microscopy (SEM) (Figs. 2-5(a) and (b)). The $PbCl_2$-deposited film and cuboid-size distributions are plotted in Figs. 2-5(c), and the synthesized perovskite with twice-large cuboid sizes (~1180 nm) through an ethanol conversion is expected to produce higher carrier mobilities [31].
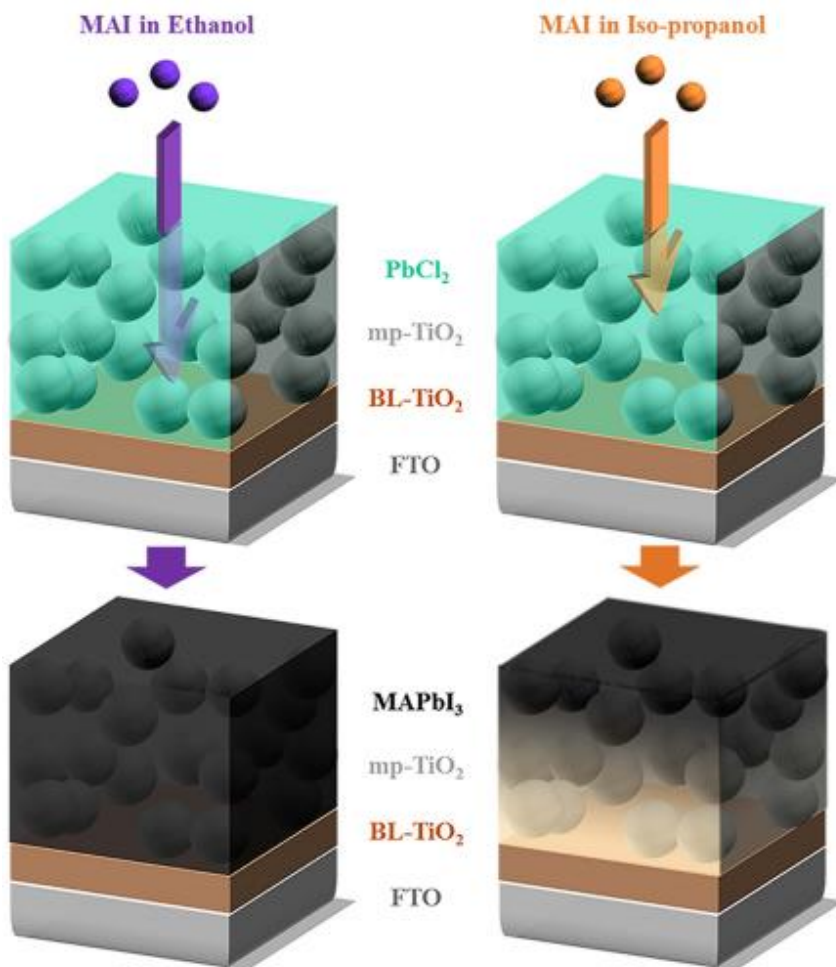
Fig. 2-1. Schematic illustration of the MAI in ethanol or iso-propanol diffusing
into the $PbCl_2$-wetted mesoporous-TiO_2 (mp-TiO_2).   The blocking-layer
is coated on SnO_2:F (FTO).
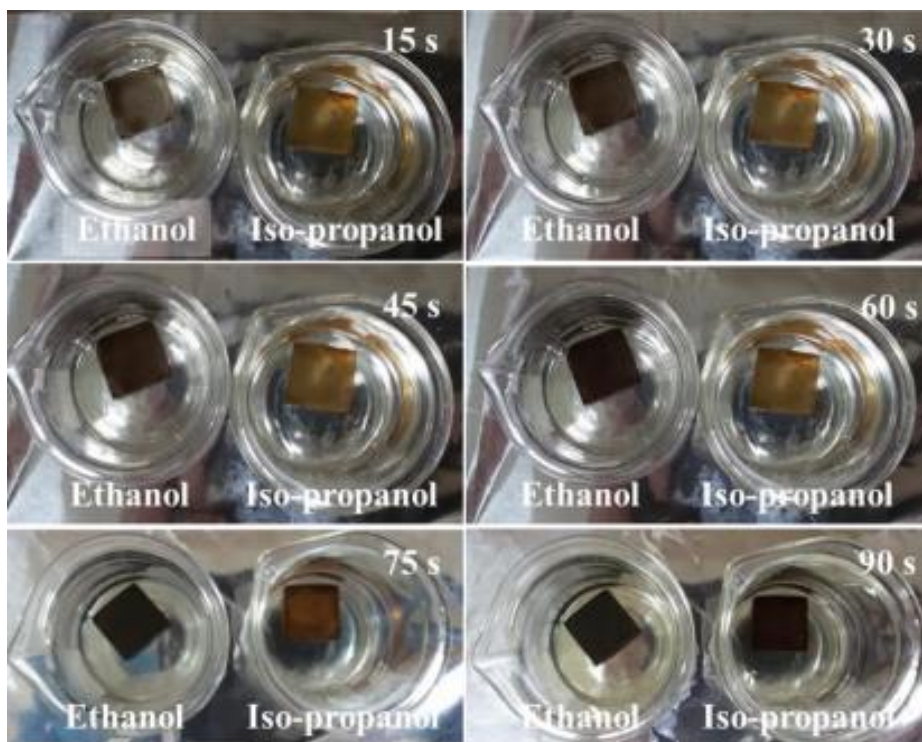
Fig. 2-2.   Time-dependent optical variation for the PbCl$_2$ films in the MAI/ethanol

or MAI/iso-propanol solution.
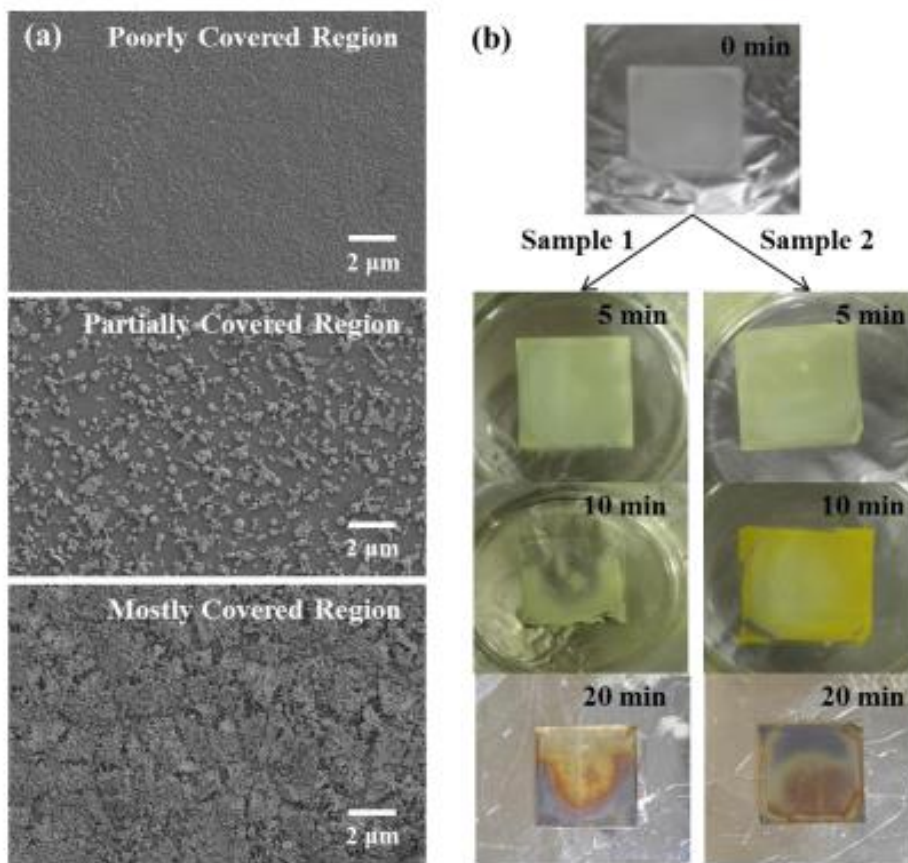
Fig. 2-3. MAPbI$_3$ conversion using a methanol solvent: (a) SEM images for the MAPb$_{I3}$ film in different regions (20-min dipping sample), and (b) optical observations in every 5 min.

V_{oc} (V)	J_{sc} (mA/cm^2)	FF	η (%)
0.99	4.64	0.45	2.08
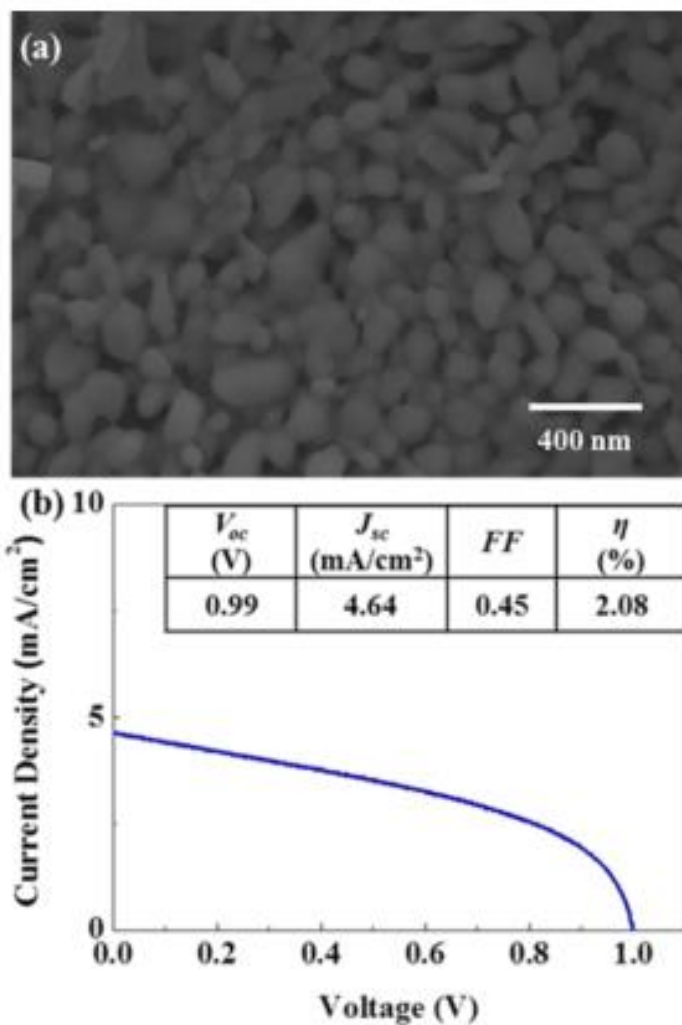
Fig. 2-4. SEM images of (a) MAPbI$_3$ and (b) *J-V* curve from the 20-mg/mL MAI/iso-propanol solution.
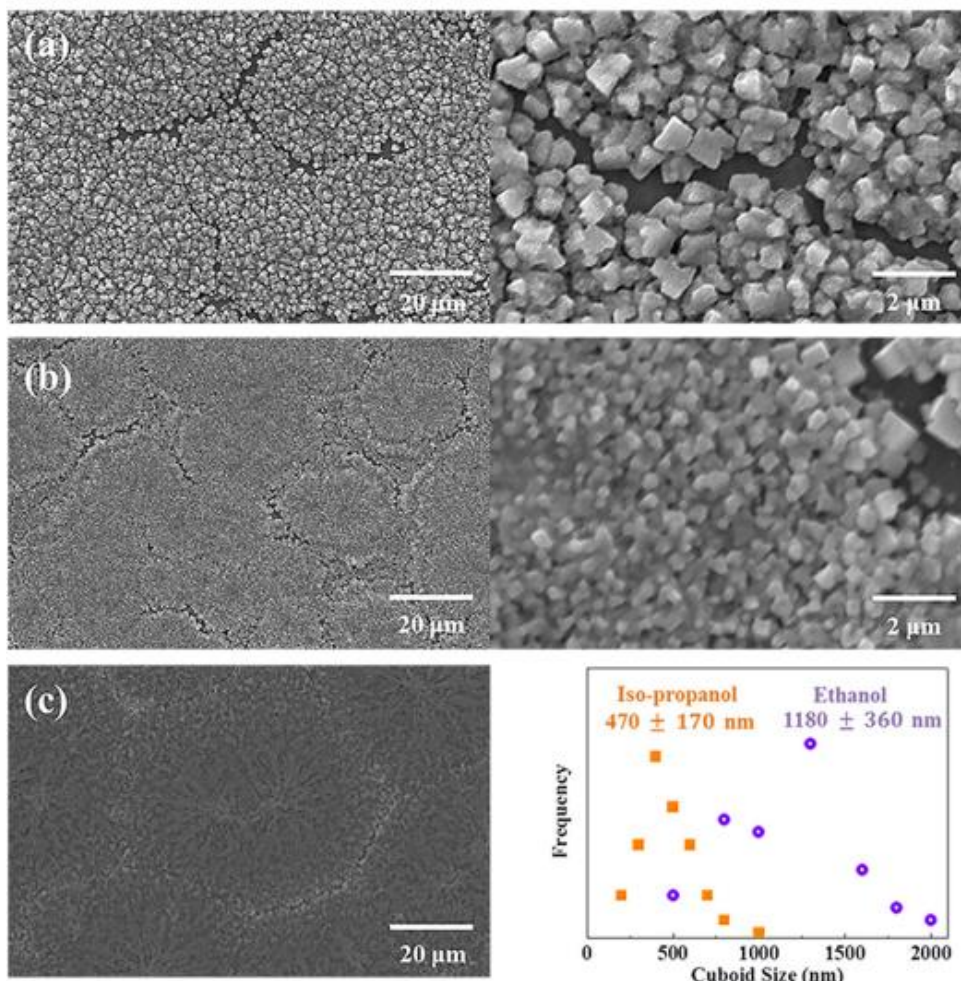
Fig. 2-5.   Solvent effects on MAPbI$_3$ using ethanol or isoporpanol.   (a) SEM images of MAPbI$_3$ using ethanol, (b) MAPbI$_3$ using iso-propanol, and (c) PbCl$_2$ on mp-TiO$_2$.   The average cuboid size is shown for MAPbI$_3$ by ethanol or iso-propanol.

Figure 2-6 illustrates qualitative analysis of the perovskite formation with ethanol or iso-propanol. The energy disperse x-ray spectroscopy (EDS) was conducted to identify the chlorine concentration (Fig. 2-6(a)). MAPbI$_3$ converted from an ethanol solution contains lower Cl than that of iso-propanol-synthesized MAPbI$_3$ since unreacted PbCl$_2$ or partially-reacted MAPbCl$_3$ remains in the film. Still, ethanol-based MAPbI$_3$ shows some chlorine content, and we believe that this is caused by MACl which is a co-product during the MAPbI$_3$ synthesis [16–18]. Actually, there is a possibility that chlorine is doped in the perovskite structure (MAPbI$_{3-x}$Cl$_x$) as reported by several groups [14–16]. However, the small quantity of chlorine in the perovskite structure is difficult to be evaluated, and the remaining chlorine may form other products [17,19]. Cross-sectional SEM image of MAPbI$_3$ perovskite solar cell by ethanol exhibits uniform film structures, as shown in Fig. 2-6(b). For further understanding of impurities, X-ray diffraction (XRD) scans were compared, and an ethanol-based MAPbI$_3$ shows clear (110), (220) and (330) peaks (Fig. 2-6(c)). On the contrary, the conversion with iso-propanol produced impurity peaks of PbI$_2$ and MAPbCl$_3$ (Fig. 2-6(c)), indicating incomplete reaction. To explain the effect of ethanol on the crystallinity, we have additionally confirmed that the longer dipping time increases the crystallinity of MAPbI$_3$ (Fig. 2-7) even when the reaction was completed. Together with the optical observation in Fig. 2-2, it can be said that MAI/ethanol-converted MAPbI$_3$ completes the reaction faster with better crystallinity, compared to that of iso-propanol for the same dipping time. Furthermore, the light absorption from the synthesized perovskite is clearly different between ethanol and iso-propanol (Fig. 2-6(d)). The enhanced absorption at approximately 800 nm by ethanol is due to the superior purity of MAPbI$_3$ ($Eg \approx 1.55$

eV), while partially-reacted MAPbI$_3$ by iso-propanol contains high-bandgap impurities, such as PbI$_2$ ($Eg\approx$ 2.36 eV) [32] and MAPbCl$_3$ ($Eg\approx$ 3.17 eV) [33]. Therefore, the overall PCE is greatly improved from 5.86% to 9.51% (Fig. 2-6(e)) with much better stability (Fig. 2-6(f)), and both methods performed high reproducibility (Fig. 2-8 and Table 2-1).   After 30 days, the PCE decreased from 9.51% to 8.53% and 5.86% to 3.75%, respectively, for the ethanol and iso-propanol solution (Table 2-2).   The improved crystallinity and enlarged grain of MAPbI$_3$ by ethanol surely prevents possible air penetration through various grain boundaries, leading to stability enhancement.   The half-lifetime of the MAPbI$_3$ perovskite solar cell (degradation details in Fig. 2-9) was estimated to be ~150 and ~40 days, respectively, for ethanol and iso-propanol.   To identify the reaction mechanisms, intermediate phases during the perovskite formation were investigated by the concentration variations of MAI in ethanol.   With a low concentration of MAI/ethanol (Fig. 2-10(a)), PbCl$_2$ partially reacts into PbI$_2$ (5mg/mL).   The chlorine in PbCl$_2$ ion-exchanges with iodine in MAI to form PbI$_2$, and the dissociated MA$^+$ and Cl$^-$ from outer PbCl$_2$ intercalate into the inner PbCl$_2$ layer, transforming to the MAPbCl$_3$ phase (15mg/mL of MAI/ethanol).   The intermediate PbI$_2$ reacts with MAI directly to form MAPbI$_3$ by intercalating MAI in the layered PbI$_2$, while MAPbCl$_3$ will ion-exchange with I$^-$ and reconstructs to the final MAPbI$_3$, as schemed in Fig. 2-10(b) (20mg/mL of MAI/ethanol). The whole reaction occurs through the following steps:

$$2 \text{ PbCl}_2 + 2 \text{ MAI} \rightarrow \text{PbI}_2 + \text{PbCl}_2 + \text{MACl} \text{ (step 1)}$$

$$\text{PbI}_2 + \text{MAI} \rightarrow \text{MAPbI}_3 \text{ (step 2)}$$

$$\text{PbCl}_2 + 2 \text{ MACl} \rightarrow \text{MAPbCl}_3 + \text{MACl} \text{ (step 3)}$$

$$\text{MAPbCl}_3 + \text{MACl} + 3\,\text{MAI} \rightarrow \text{MAPbI}_3 + 4\,\text{MACl (step 4)}$$

$$\text{PbCl}_2 + 3\,\text{MAI} \rightarrow \text{MAPbI}_3 + 2\,\text{MACl (Total Reaction)}$$
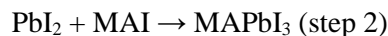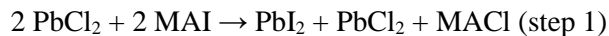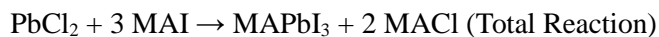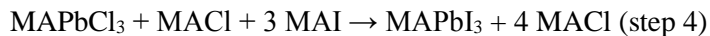
The PbI$_2$ phase converts into MAPbI$_3$ earlier than the formation of MAPbCl$_3$, as shown by the X-ray diffraction of MAPbI$_3$ vs. MAPbCl$_3$ phases for MAI concentrations of 10 and 15mg/mL (Fig. 2-10(a)). We have also compared the perovskite formation from MAPbCl$_3$ (MAPbCl$_3$ + 3 MAI → MAPbI$_3$ + 3 MACl) with PbI$_2$ (PbI$_2$ + MAI → MAPbI$_3$) (respectively, in the middle and right of Fig. 2-10(a)), and found that both have resulted in no intermediate phases. Synthesizing fully-converted MAPbI$_3$ from PbCl$_2$ requires both intercalation and reconstruction steps, while the idea of reconstruction from MAPbCl$_3$ to MAPbI$_3$ was investigated in the previous report [34]. Therefore, we intuitively conclude that the recrystallization of intermediates both inside and on top of the mp-TiO$_2$ film can enhance the coverage morphology, nanostructures, and crystallinity [16–18] of MAPbI$_3$ by multiple crystal-alignment steps. Moreover, ethanol conversion increases the kinetics of the reaction steps, and produces improved MAPbI$_3$ film, compared to the conversion with iso-propanol.
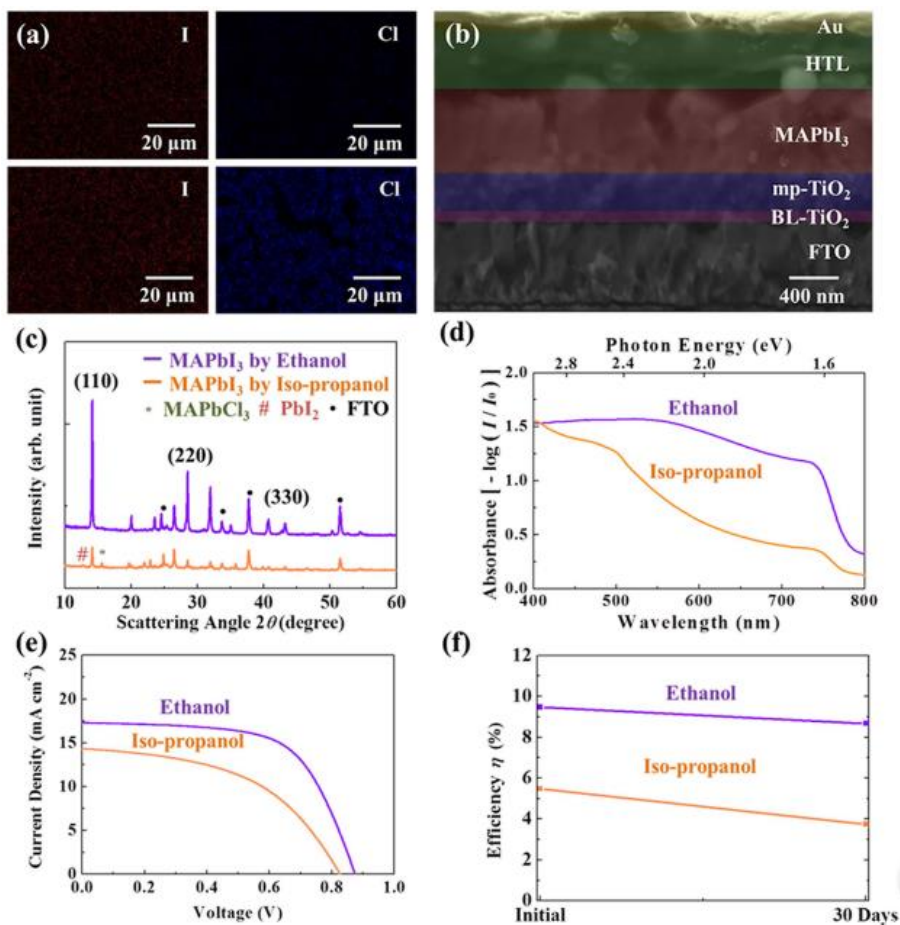
Fig. 2-6. The dependence of MAPbI$_3$ perovsktie solar cells using the MAI in an ethanol or iso-propanol solution.   (a) EDS mapping for iodine and chlorine in the synthesized MAPbI$_3$ with an ethanol (top) or isopropanol (bottom) solution.   (b) Cross-sectional SEM image of a MAPbI$_3$ perovskite solar cell from the MAI/ethanol solution.   (c) X-ray diffraction of MAPbI$_3$.   (d) Absorption spectra for the synthesized MAPbI$_3$.   (e) *J-V* characteristics of the MAPbI$_3$ perovskite solar cells. (f) Degradation of solar cells synthesized by ethanol or isopropanol for the as-fabricated cells and cells after 30 days.
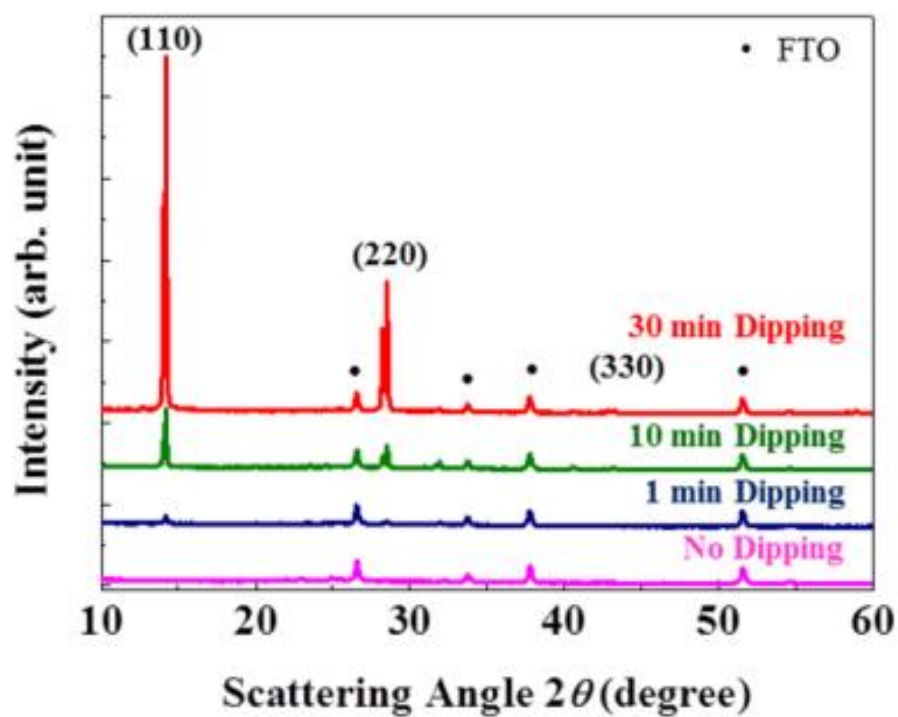
Fig. 2-7. X-ray diffraction from various MAI/ethanol dipping times on the PbCl$_2$ film.
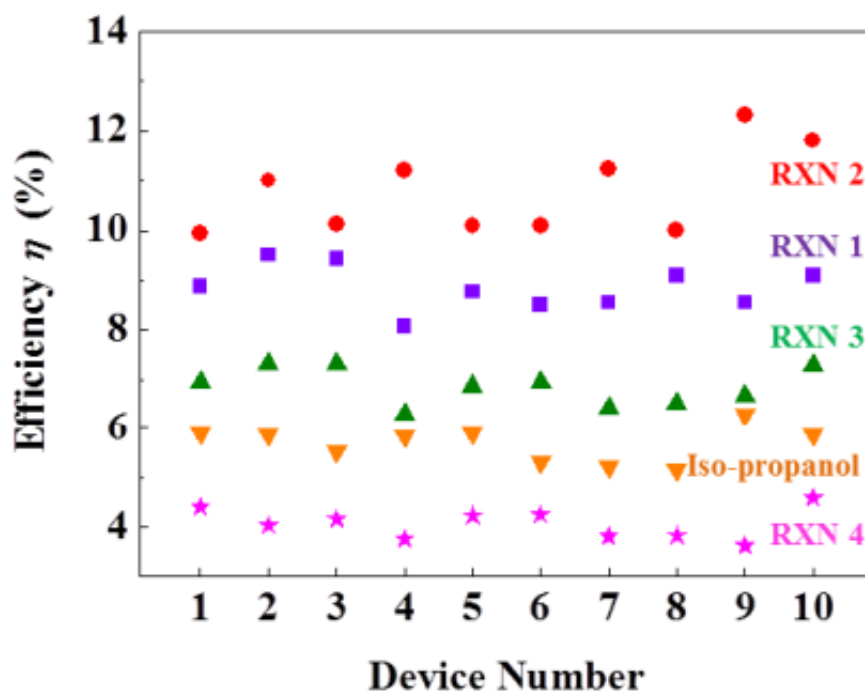
Fig. 2-8.   Device reproducibility of MAPbI$_3$ perovskite solar cells from the reactions 1, 2, 3, 4, and iso-propanol.

Device	Iso-propanol	RXN 1	RXN 2	RXN 3	RNX 4
1	5.89%	8.87%	9.95%	6.95%	4.40%
2	5.87%	9.51%	11.00%	7.32%	4.03%
3	5.53%	9.43%	10.12%	7.31%	4.16%
4	5.84%	8.07%	11.19%	6.29%	3.76%
5	5.91%	8.76%	10.10%	6.87%	4.23%
6	5.31%	8.50%	10.10%	6.94%	4.24%
7	5.23%	8.55%	11.24%	6.44%	3.80%
8	5.15%	9.09%	10.00%	6.51%	3.83%
9	6.30%	8.55%	12.30%	6.67%	3.62%
10	5.86%	9.09%	11.80%	7.29%	4.58%

Table 2-1.   Power conversion efficiencies of MAPbI$_3$ perovskite solar cells from

the reactions 1, 2, 3, 4, and iso-propanol.

Reaction Condition		V_{oc} (V)	J_{sc} (mA/cm^2)	FF	η (%)
Initial	Ethanol	0.87	17.3	0.63	9.51
	Iso-propanol	0.83	14.4	0.49	5.86
30 Days	Ethanol	0.84	16.4	0.63	8.53
	Iso-propanol	0.79	10.1	0.47	3.75

Table 2-2.   Photovoltaic performance of MAPbI$_3$ perovskite solar cells using an ethanol or iso-propanol solution (as-fabricated cells and cells after 30 days).
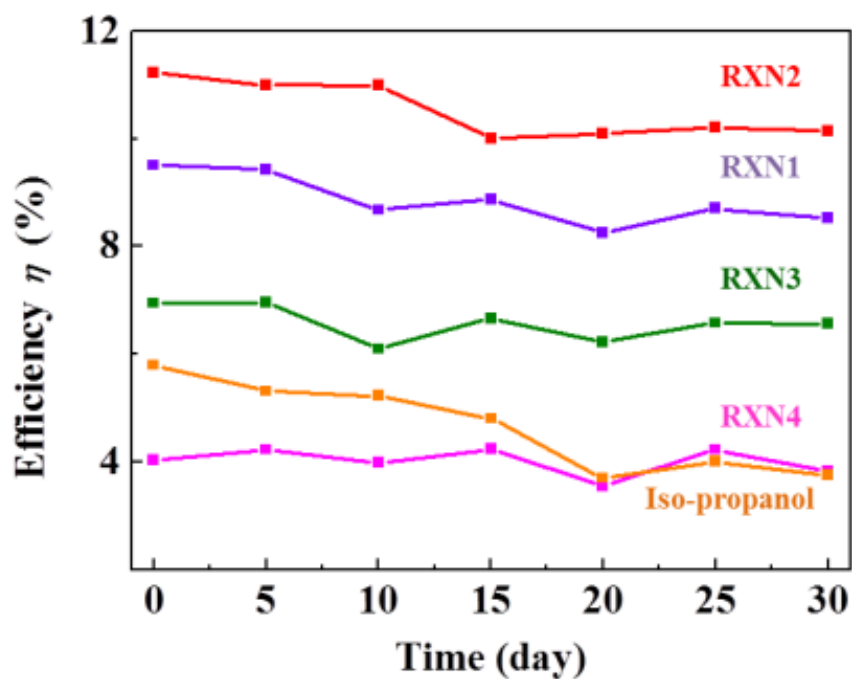
Fig. 2-9.   Stability of MAPbI$_3$ perovskite solar cells from the reactions 1, 2, 3, and 4 for 30 days.   The corresponding data by iso-propanol (RXN 1) are also shown.
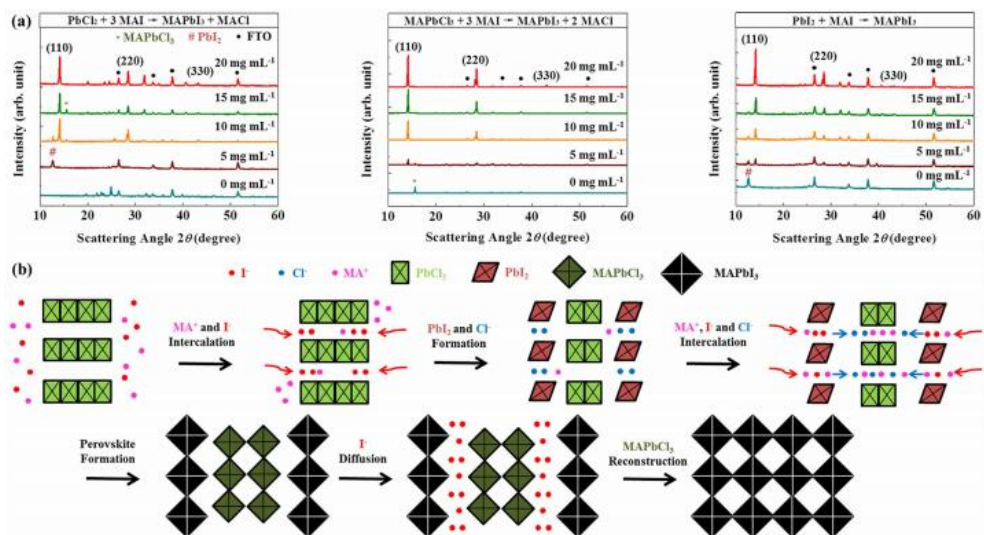
Fig. 2-10. Reaction intermediates and mechanism analysis by X-ray diffraction measurements. (a) Reaction 1 (left), reaction 4 (middle), and PbI_2 precursor (right) with various concentrations of MAI in an ethanol solution. (b) Mechanisms of reaction 1 ($PbCl_2$ + 3 MAI → $MAPbI_3$ + 2 MACl). The MAI and ethanol diffuse into the outer $PbCl_2$ layer, which converts $PbCl_2$ into PbI_2 and MACl. Additional MAI from the solution converts the synthesized outer PbI_2 into $MAPbI_3$, and MACl reacts with the inner $PbCl_2$ transforming into $MAPbCl_3$. The synthesized $MAPbCl_3$ ion-exchanges with I^- for the full $MAPbI_3$ and MACl to complete the reaction.

2.3.1. Reaction Mechanism Engineering. To understand the phase-formation paths of MAPbI$_3$ from PbCl$_2$, we came up with an idea to further optimize MAPbI$_3$ by utilizing the identified intermediate phases. While the direct conversion of MAPbCl$_3$ to MAPbI$_3$ can drastically reduce the reaction time, the repetition of crystallization from PbCl$_2$ to MAPbI$_3$ will enhance the surface morphology. Even though PbI$_2$ appears during the transformation of the PbCl$_2$ precursor to MAPbI$_3$, and increases the reaction kinetics, the MAPbCl$_3$ precursor is more reactive than the PbI$_2$ precursor to synthesize MAPbI$_3$ (middle and right graphs in Fig. 2-10(a)) where the MAPbCl$_3$ precursor is likely to transform with lower MAI concentration than that of the PbI$_2$ precursor. Also, the chlorine-based precursor should be preferred considering the positive effects of chlorine on the MAPbI$_3$ perovskite solar cells [16–20]. Therefore, a straightforward direction is rendered by mixing PbCl$_2$ and MAPbCl$_3$ in several different ratios of 3:0 (reaction 1), 2:1 (reaction 2), 1:2 (reaction 3), and 0:3 (reaction 4), to optimize the reaction time with smooth surface morphology (Table 2-3 and Fig. 2-11).

As expected, we observed the morphology changes by synthesizing MAPbI$_3$ films from precursors with different ratios of PbCl$_2$ and MAPbCl$_3$ through SEM, as shown in Fig. 2-12(a). Perovskite films synthesized by reaction 2 exhibits clearly improved coverage with ~2320-nm-sized cuboids. Furthermore, addition of MAPbCl$_3$ (reaction 3 and 4) deteriorates the coverage, but increases the cuboid size. When a larger amount of the MAPbCl$_3$ precursor is added through reactions, the crystallinity of MAPbI$_3$ is enhanced significantly, as shown by XRD (Figs. 2-12

(b) and (c)).   The enhanced crystallinity can be explained by the extent of reaction, and the facilely-transformed perovskite is likely to have high crystallinity even with the same dipping time (Fig. 2-7).   These observations are also consistent with the optical variations during the $MAPbI_3$ formation (Fig. 2-13).   It should be noted that the coverages for the reactions 1, 2, 3, and 4 are different.   However, conversions at ~10 s are distinct between reactions 1 ($PbCl_2$ precursor) and 4 ($MAPbCl_3$ precursor).   The light absorption in Figs. 2-12(d) indicates that the absorption is more influenced by the coverage rather than the crystallinity and cuboid size of $MAPbI_3$.   The maximum coverage in reaction 2 reached the highest absorption, and the minimum coverage with reaction 4 yielded the lowest absorption.   As a material perspective, $MAPbI_3$ synthesis by reaction 4 is supposed to show excellent properties due to the high crystallinity and cuboid sizes, as plotted in Fig. 2-14(a).   Moreover, EDS was additionally measured to identify the comparative chlorine contents with iodine, which is plotted in Fig. 2-14(b) for each reaction, indicating that reaction 1 obtained the highest, and reaction 4 occupied the lowest concentration of chlorine. This chlorine tendency suggests that a co-product of MACl is minimized through the addition of $MAPbCl_3$ (It should be noted that the EDS technique may not reflect the accurate chlorine concentration due to the coverage difference of each reaction.).   It is possible that the detected chlorine through EDS is from the MACl phase or other products [16–18].   Moreover, excessive chlorine may lead to impurities, and deteriorate the device performance.   Therefore, high crystallinity and low impurity of $MAPbI_3$ are highly beneficial in the carrier mobilities, but recombination of

carriers arising from poor coverage [31] is another factor that we should be aware of.

To understand the effects of crystallinity and coverage on the photovoltaic performance and stability, *J-V* curves are measured for 30 days under ambient conditions (Fig. 2-9, and Table 2-4).   In Fig. 2-14(c), *J-V* curves were shown for the performance of the solar cells from each reaction, and the highly covered perovskite film from reaction 2 achieved the highest PCE of 11.23%.   The lowest PCE of 4.03% was obtained by reaction 4, and these results indicate that the initial PCE is highly dependent on the perovskite coverage, which plays crucial roles in the carrier recombination.   In contrast, MAPbI$_3$ synthesized by reaction 4 was distinctively stable after 30 days.   The stability is well correlated with the crystallinity and grain size, apparent from the normalized PCE in Fig. 2-14(d), confirming the reduced decomposition behavior from the low-defect perovskite. All of the solar cells with different experimental conditions performed high reproducibility (Fig. 2-8 and Table 2-1).   From the reactions 1, 2, 3, and 4, the half-lifetimes of MAPbI$_3$ perovskite solar cells (degradation details in Supplementary Fig. 2-9) are estimated to be ~150, ~160, ~270, and ~300 days.

	Reaction Mechanism	Precursor Ratio ($PbCl_2$: $MAPbCl_3$)
RXN 1	$PbCl_2 + 3\ MAI \rightarrow MAPbI_3 + 2\ MACl$	3:0
RXN 2	$2\ PbCl_2 + MAPbCl_3 + 9\ MAI \rightarrow 3\ MAPbI_3 + 7\ MACl$	2:1
RXN 3	$PbCl_2 + 2\ MAPbCl_3 + 9\ MAI \rightarrow 3\ MAPbI_3 + 8\ MACl$	1:2
RXN 4	$MAPbCl_3 + 3\ MAI \rightarrow MAPbI_3 + 3\ MACl$	0:3

Table 2-3.   Precursor ratio of $PbCl_2$: $MAPbCl_3$ for the reactions 1, 2, 3, and 4.
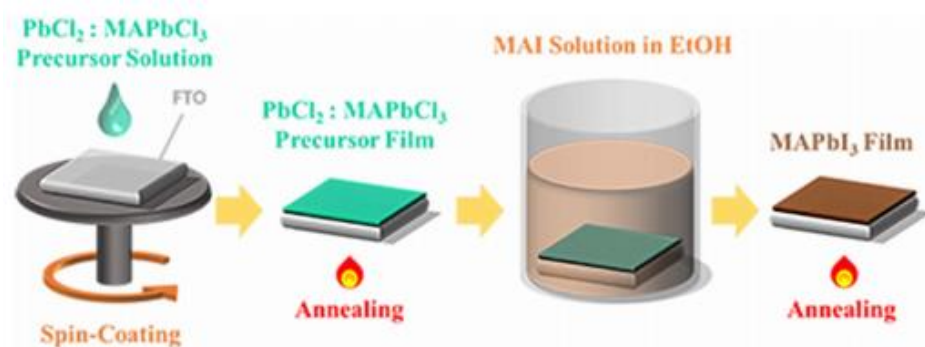
Fig. 2-11.　Schematic illustration of the experimental procedure.　Various ratios of PbCl$_2$: MAPbCl$_3$ were initially deposited on the substrate, and then the MAI-dissolved ethanol solution was utilized to synthesize MAPbI$_3$.
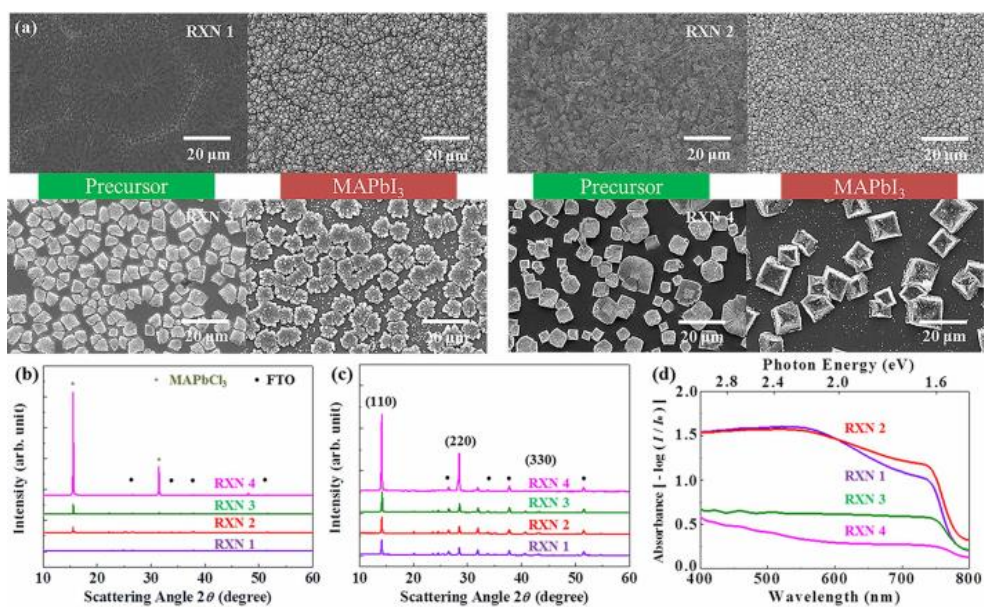
Fig. 2-12. The film quality dependence of MAPbI$_3$ for the reactions 1, 2, 3, and 4. (a) SEM images of the precursor and MAPbI$_3$, (b,c) X-ray diffraction for the precursor and MAPbI$_3$, and (d) absorption spectra of MAPbI$_3$ by reactions 1, 2, 3, and 4.
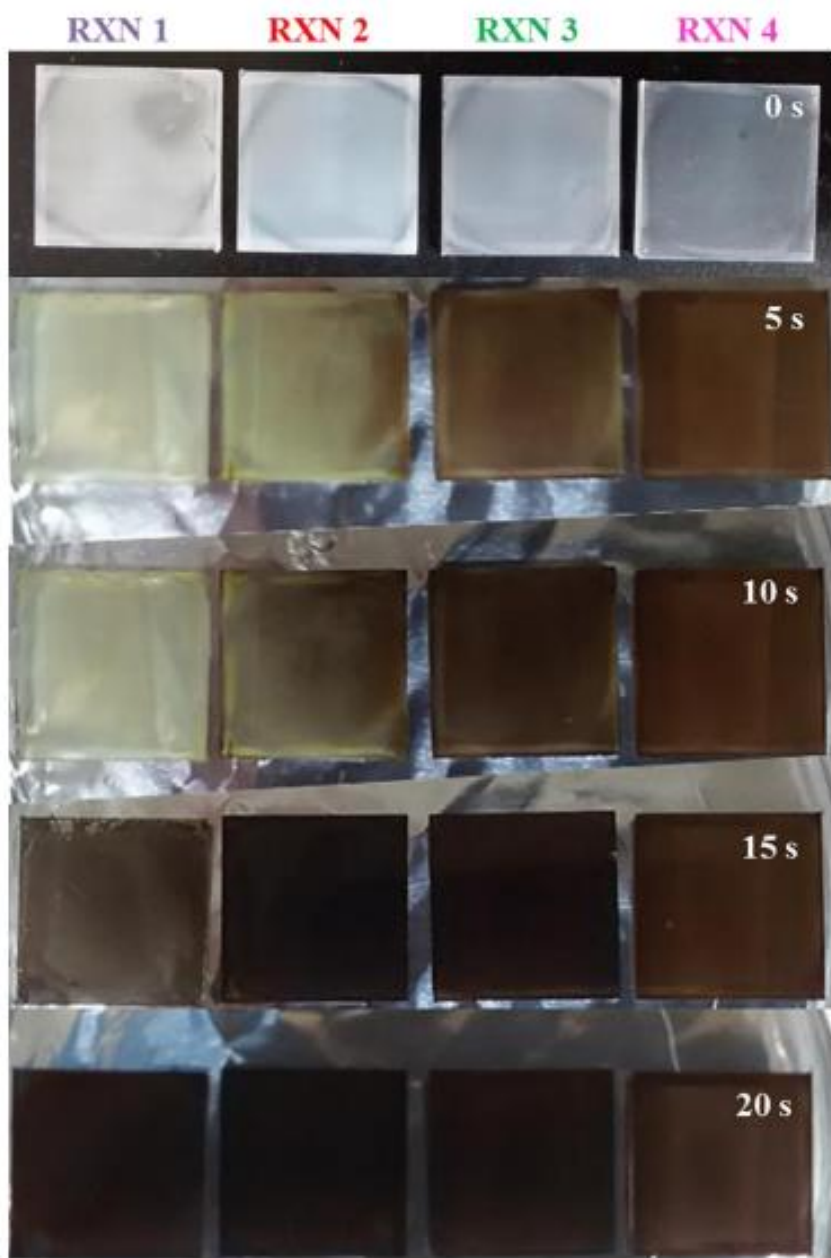
Fig. 2-14.   Time-dependent optical variation for the reactions 1, 2, 3, and 4 in a
MAI/ethanol solution.

Reaction Conditions		V_{oc} (V)	J_{sc} (mA cm^{-2})	FF	η(%)
Initial	RXN 1	0.87	17.3	0.63	9.51
	RXN 2	0.90	19.8	0.63	11.23
	RXN 3	0.76	16.3	0.56	6.94
	RXN 4	0.61	11.7	0.57	4.03
30 Days	RXN 1	0.84	16.4	0.62	8.53
	RXN 2	0.89	17.8	0.64	10.14
	RXN 3	0.73	15.2	0.59	6.55
	RXN 4	0.61	11.7	0.52	3.83

Table 2-4.   Solar cell performance from the reactions 1, 2, 3, and 4 (as-fabricated cells and cells after 30 days).

2.4. Conclusions

Fast conversion can have positive influences on the device performance and stability by producing highly-crystalline $MAPbI_3$ perovskite. Therefore, we have controlled the diffusion reaction of MAI and $PbCl_2$ with ethanol to boost the perovskite transformations, leading to phase-pure and highly-crystalline perovskite films. Since $PbCl_2$ goes through several intermediate phases during the formation of $MAPbI_3$, we utilized the intermediates by mixing them with a conventional $PbCl_2$ precursor to boost the conversion kinetics and performance of the resulting solar cell. Thereby, the optimized crystallinity and coverage yielded a PCE of 11.23% with $PbCl_2$: $MAPbCl_3$ = 2:1 (reaction 2). Although the precursor with 100% $MAPbCl_3$ (reaction 4) resulted in the fastest transformations of $MAPbI_3$ and the most stable solar cell performance, poor coverage lowered the PCE of the device. Therefore, compact coverage of the perovskite with super-sized cuboids expects to achieve further enhanced performance and stability of the $MAPbI_3$ perovskite solar cell. At this point, investigation of hysteresis still remains as a future work.

2.5. References

1. B. Shin, O. Gunawan, Y. Zhu, A. N. Bojarczuk, S. J. Chey, and S. Guha, "Thin Film Solar Cell with 8.4% Power Conversion Efficiency using an Earth-Abundant Cu_2ZnSnS_4 Absorber," *Prog. Photovolt.: Res. Appl.* **21**, 72 (2013).

2. H. Choi, J. Kim, C. Nahm, C. Kim, S. Nam, J. Kang, B. Lee, T. Hwang, S. Kang, D. J. Choi, Y.-H. Kim, and B. Park, "The Role of ZnO-Coating-Layer Thickness on the Recombination in CdS Quantum-Dot-Sensitized Solar Cells," *Nano Energy*, **2**, 1218 (2013).

3. D. Kim, C. M. Hangarter, R. K. Debnath, J. Y. Ha, C. R. Beauchamp, M. D. Widstrom, J. E. Guyer, N. V. Nguyen, B. Y. Yoo, and D. Josell, "Backcontact CdSe/CdTE Windowless Solar Cells," *Sol. Energ. Mat. Sol. C*. **109**, 246 (2013).

4. J. Kim, H. Choi, C. Nahm, C. Kim, S. Nam, S. Kang, D.-R. Jung, J.-I Kim, J. Kang, and B. Park, "The Role of a $TiCl_4$ Treatment on the Performance of CdS Quantum-Dot-Sensitized Solar Cells," *J. Power Sources* **220**, 108 (2012).

5. H. Choi, T. Hwang, S. Lee, S. Nam, J. Kang, B. Lee, and B. Park, "The Construction of Tandem Dye-Sensitized Solar Cells from Chemically-Derived Nanoporous photoelectrodes," *J. Power Sources* **274**, 937 (2015).

6. A. Kojima, K. Teshima, Y. Shirai, and T. Miyasaka, "Organometal Halide Perovskites as Visible-Light Sensitizers for Photovoltaic Cells," *J. Am. Chem. Soc.* **131**, 6050 (2009).

7. National Renewable Energy Laboratory (NREL), Best Research-Cell Efficiencies, http://www.nrel.gov/ncpv/images/efficiency_chart.jpg (Accessed:

30th March, 2016).

8. S. Kazim, M. K. Nazerruddin, M. Gratzel, and S. Ahmad, "Perovskite as Light Harvester: A Game Charger in Photovoltaics," *Angew. Chem. Int. Ed.* **53**, 2812 (2014).

9. M. D. McGehee, Materials science: Fast-Track Solar Cells. *Nature* **501**, 323 (2013).

10. G. Hodes, Perovskite-Based Solar Cells. *Science* **342**, 317 (2013).

11. C. S. Ponseca, T. J. Savenije, M. Abdellah, K. Zheng, A. Yartsev, T. Pascher, T. Harlang, P. Chabera, T. Pullerits, A. Stepanov, J.-P. Wolf, and V. Sundstrom, "Organometal Halide Perovskite Solar Cell Materials Rationalized: Ultrafast Charge Generation, High and Microsecond-Long Balanced Mobilities, and Slow Recombination," *J. Am. Chem. Soc*. **136**, 5189 (2014).

12. J. M. Frost, K. T. Butler, F. Brivio, C. H. Hendon, M. v. Schilfgaarde, A. Walsh, "Atomistic Origins of High-Performance in Hybrid Halide Perovskite Solar Cells," *Nano Lett*. **14**, 2584 (2014).

13. M. M. Lee, J. Teuscher, T. Miyasaka, T. N. Murakami, and H. J. Snaith, "Efficient Hybrid Solar Cells based on Meso-Superstructured Organometal Halide Perovskites," *Science* **338**, 643 (2012).

14. S. Colella, E. Mosconi, P. Fedeli, A. Listorti, F. Gazza, F. Orlandi, P. Ferro, T. Besagni, A. Rizzo, G. Calestani, G. Gigli, F. D. Angelis, R. Mosca, "MAPbI$_{3-x}$Cl$_x$ Mixed Halide Perovskite for Hybrid Solar Cells: the Role of Chloride as Dopant on the Transport and Structural Properties," *Chem. Mater*.

25, 4613 (2013).

15. C. Wehrenfennig, G. E. Eperon, M. B. Johnston, H. J. Snaith, and L. M. Herz, "High Charge Carrier Mobilities and Lifetimes in Organolead Trihalide Perovskites." *Adv. Mater.* **26**, 1584 (2014).

16. S. T. Williams, F. Zuo, C.-C. Chueh, C.-Y. Liao, P.-W. Liang, and A. K.-Y. Jen, "Role of Chloride in the Morphological Evolution of Organo-Lead Halide Perovskite Thin Films," *ACS Nano* **8**, 10640 (2014).

17. E. L. Unger, A. R. Bowring, C. J. Tassone, V. L. Pool, A. Gold-Parker, R. Cheacharoen, K. H. Stone, E. T. Hoke, M. F. Toney, and M. D. McGehee, "Chloride in Lead Chloride-Derived Organo-Metal Halides for Perovskite-Absorber Solar Cells," *Chem. Mater*. **26**, 7158 (2014).

18. M. Deepa, J. F. Ramos, M. S. Shivaprasad, and S. Ahmad, "Unravelling the Role of Monovalent Halides in Mixed-Halide Organic Inorganic Perovskite," *ChemPhysChem* **17**, 913 (2016).

19. W.-J. Yin, H. Chen, T. Shi, S.-H. Wei, and Y. Yan, "Origin of High Electronic Quality in Structurally Disordered $CH_3NH_3PbI_3$ and the Passivation Effect of Cl and O at Grain Boundaries," *Adv. Electron. Mater*. **1**, 1500044 (2015).

20. E. Mosconi, E. Ronca, and F. D. Angelis, "First-Principles Investigation of the TiO_2/Organohalide Perovskites Interface: the Role of Interfacial Chlorine," *J. Phys. Chem. Lett.* **5**, 2619 (2014).

21. Q. Chen, H. Zhou, Z. Hong, S. Luo, H.-S. Duan, H.-H. Wang, Y. Liu, G. Li, Y. Yang, "Planar Heterojunction Perovskite Solar Cells via Vapor-Assisted

Solution Process," *J. Am. Chem. Soc*. **136**, 622 (2013).

22. G. E. Eperon, V. M. Burlakov, P. Docampo, A. Goriely, and H. J. Snaith, "Morphological Control for High Performance, Solution Processed Planar Heterojunction Perovskite Solar Cells," *Adv. Funct. Mater.* **24**, 151 (2014).

23. M. Liu, M. B. Johnston, and H. J. Snaith, "Efficient Planar Heterojunction Perovskite Solar Cells by Vapour Deposition," *Nature* **501**, 395 (2013).

24. A. Mihi, C. Zhang, and P. V. Braun, "Transfer of Preformed Three-Dimensional Photonic Crystals onto Dye-Sensitized Solar Cells," *Angew. Chem. Int. Ed*. **50**, 5712 (2011).

25. J. Grandidier, D. M. Callahan, J. N. Munday, and H. A. Atwater, "Light Absorption Enhancement in Thin-Film Solar Cells using Whispering Gallery Modes in Dielectric Nanospheres," *Adv. Mater*. **23**, 1272 (2011).

26. J. Burschka, N. Pellet, S.-J. Moon, R. Humphry-Baker, P. Gao, M. K. Nazeeruddin, and Michael Gratzel, "Sequential Deposition Route to High Performance Perovskite-Sensitized Solar Cells," *Nature* **499**, 316 (2013).

27. J.-H. Im, H.-S. Kim, and N.-G. Park, "Morphology-Photovoltaic Property Correlation in Perovskite Solar Cells: One-Step Versus Two-Step Deposition of $CH_3NH_3PbI_3$," *APL Mater.* **2**, 081510 (2014).

28. Y. Ma, L. Zheng, Y.-H. Chung, S. Chu, L. Xiao, Z. Chen, S. Wang, B. Qu, Q. Gong, Z. Wu, and X. Hou. "A Highly Efficient Mesoscopic Solar Cell based on $CH_3NH_3PbI_{3-x}Cl_x$ Fabricated via Sequential Solution Deposition," *Chem. Commun*. **50**, 12458 (2014).

29. N. Yantara, D. Sabba, F. Yanan, J. M. Kadro, T. Moehl, P. P. Boix, S. Mhaisalkar, M. Grätzeld, and C. Grätzel, "Loading of Mesoporous Titania Films by $CH_3NH_3PbI_3$ Perovskite, Single Step vs. Sequential Deposition," *Chem. Commun*. **51**, 4603 (2015).

30. J.-H. Im, I.-H. Jang, N. Pellet, M. Gratzel, and N.-G. Park, "Growth of $CH_3NH_3PbI_3$ Cuboids with Controlled Size for High-Efficiency Perovskite Solar Cells," *Nat. Nanotechnol*. **9**, 927 (2014).

31. W. Nie, H. Tsai, R. Asadpour, J.-C. Blancon, A. J. Neukirch, G. Gupta, J. J. Crochet, M. Chhowalla, S. Tretiak, M. A. Alam, H.-L. Wang, A. D. Mohite, "High-Efficiency Solution-Processed Perovskite Solar Cells with Millimeter-Scale Grains," *Science* **347**, 522 (2015).

32. T. Supasai, N. Rujisamphan, K. Ullrich, A. Chemseddine, and T. Dittrich, "Formation of a Passivating $CH_3NH_3PbI_3/PbI_2$ Interface during Moderate Heating of $CH_3NH_3PbI_3$ Layers," *Appl. Phys. Lett*. **103**, 183906–1 (2013).

33. R. Comin, G. Walters, E. S. Thibau, O. Voznyy, Z.-H. Lu, and E. H. Sargent, "Structural, Optical, and Electronic Studies of Wide-Bandgap Lead Halide Perovskites." *J. Mater. Chem. C* **3**, 8839 (2015).

34. H. Zhou, Q. Chen, G. Li, S. Luo, T.-b. Song, H.-S. Duan, Z. Hong, J. You, Y. Liu, Y. Yang, "Interface Engineering of Highly Efficient Perovskite Solar Cells." *Science* **345**, 542 (2014).

Chapter 3.

Synergetic Effect of Double-Step Blocking Layer for the Perovskite Solar Cell

3.1. Introduction

The organometallic $CH_3NH_3PbI_3$ ($MAPbI_3$) perovskite solar cells have received an enormous attention as next generation photovoltaics due to the potential strength of high power conversion efficiencies (PCEs) and low fabrication cost [1–13]. The perovskite semiconductor satisfies appropriate and direct bandgap, small exciton binding energy, and balanced ambipolar charge transport properties [14–18]. Even though the PCE of perovskite solar cell has reached 22.10%, it still has a potential to enhance the performance up to the theoretical limit of 31.40% [19,20].

The role of blocking layer in the perovskite solar cell is crucial because it prevents the recombination of electrons from a transparent conducting oxide (TCO) to the perovskite layer, impacting hugely on the performance of solar cells [21–24]. Among various deposition methods, spray-pyrolysis and solution spin-coating are well known techniques in the field of perovskite solar cells due to their low cost and easiness of process [25–29]. In 2014, a compact layer using atomic layer deposition (ALD) was introduced with high PCE [30–32]. Nevertheless, ALD is inadequate to the large scale production due to its slow deposition rate and reaction

sensitivity [33].   On the other hand, the deposition is extensively utilized in industry owing to the fast deposition rate and compactness of the film and was also introduced with solar cell fabrication [2,6,10,34,35].   Even though the sputtering deposition can construct a compact layer, TiO_2 by sputtering yields some porous structure that allows the carrier recombination, and thereby, post-treatment or further improvement is still required [35].

Herein, we demonstrate the double-step deposition method, through a combination of sputter and solution to construct a vastly compact blocking layer. Compact TiO_2 layer was first deposited by sputtering, and any remaining pores were facilely post-treated through the solution process.   As a result, the transmittance and uniformity of the blocking layer were largely improved.   Consequently, the utilization of double-step deposition provided a favorable environment for the perovskite growth, leading to the enhancement of crystallinity and morphology of the perovskite layers.   Conclusively, this straightforward double-step deposition improved the quality of the perovskite solar cell, reducing the recombination rate and thereby yielding high solar-cell efficiency.

3.2. Experimental Section

Synthesis of TiO₂ blocking layer. Fluorine-doped tin oxide substrate (FTO, TEC 8: Pilkington) was cleaned by sonication in Mucasol (Aldrich), ethanol (Daejung), and de-ionized (DI) water for 30 min sequentially. The sputter-based TiO_2 blocking layer was fabricated by sputtering system. With the TiO_2 target (anatase, 99.99%, RND Korea), the deposition was performed at room temperature (RT) under an Ar atmosphere with an operating pressure of and rf power of 100 W for 100 min. The solution-based TiO_2 blocking layer was deposited by spin-coating the mixture solution of 0.15 M titanium diisopropoxide bis(acetylacetonate) (75.0 wt. % in iso-propanol, Aldrich) and 1-butanol (Aldrich) at 2500 rpm for 20 s, followed by heating at 125°C for 5 min in an air oven. For the double-step deposition, sputter deposition

was first performed for 60 min. Then, the 0.15 M mixture solution was spin-coated. The substrates with three different conditions were annealed at 500°C for 30 min.

Solar-cell fabrication. After the TiO_2 blocking-layer deposition, TiO_2 pastes (ENB Korea) with 20 nm nanoparticles were mixed with terpineol (Aldrich), followed by spin-coating at 4000 rpm for 30 s, yielding a 350 nm thickness of mesoporous TiO_2 (mp-TiO_2) layer. For the perovskite synthesis, the solution of 1.5 M $PbCl_2$ (Aldrich) diluted in dimethyl sulfoxide (DMSO, Aldrich) was preheated at 100°C, and spin-coated at 2000 rpm for 5 s, followed by 6000 rpm for 5 s on the preheated substrate at 150°C. The film was annealed at 150°C for , cooled down in an ambient condition (25°C and 55% humidity), and dipped into of synthesized CH_3NH_3I (MAI) in an anhydrous ethanol solution (Daejung) for 20 min, followed by annealing at

100°C for 30 min [25,36] The hole transport material (HTM) was prepared by mixing 72.3 mg/mL of spiro-OMeTAD (Merck) in chlorobenzene (Aldrich), with 28.8 uL of (Aldrich) and a 17.5 uL solution of 520 mg of lithium bis(trifluoromethylsulfonyl) imide salt (Aldrich) in 1 mL acetonitrile (Aldrich), and was at 3000 rpm for 45 s. Finally, 100-nm-thick Au electrode was thermally evaporated.

Device characterization.   The field-emission scanning electron microscope (FESEM; Merlin-Compact: Carl Zeiss) was used to observe the morphologies of blocking layer and MAPbI$_3$.   The phases of the synthesized samples were characterized by X-ray diffraction (XRD; D8 Advance: Bruker).   The photocurrent-voltage (*J–V*) curves of MAPbI$_3$ perovskite solar cells were obtained with a potentiostat (CHI 608C; CH Instrumental Inc.) under AM 1.5 at 100 mW/cm^2 (K3000; McScience) with an active cell area of 0.09 cm^2 and 10 V/s of scan rate. The transmittance spectra of the MAPbI$_3$ and blocking layers were recorded on a UV-vis spectrophotometer (Lambda 20; Perkin Elmer), and the electrochemical impedance spectra (EIS) were measured by a potentiostat with 20 mV sinusoidal perturbation and frequencies ranging from 10^{-1} to 10^5 Hz.   The topography data were obtained utilizing atomic-force microscopy (AFM; XE-70: Park System).   An external quantum efficiency (EQE) measurement system (K3100; McScience, Korea) was used to obtain the EQE spectra.

3.3. Results and Discussion

To resolve the carrier recombination problem, a highly compact blocking-layer is required. While sputter deposition is one option with energetic sputtered atoms (5 eV), it still yields a porous structure that allows some recombination [35,37]. Therefore, we have deposited TiO_2 by sputtering first and then filled up any porous channels with solution-based precursors (with the optimization step as illustrated in Table 3-1 and Fig. 3-1, supplementary material). Schematics and (Fig. 3-2) represent the expected nanostructures of the blocking layer, and the arrow size indicates the level of carrier recombination, which would be controlled by the compactness of blocking layer. However, band alignment of all three conditions stays the same, because sputter and solution both yield anatase-phase TiO_2 [38,39]. Previous studies identified that sputter-deposited blocking layer performs better than that of the solution owing to the high compactness of the film [34]. However, the cross-sectional and plan views of the sputter deposition present inevitable pinholes that can seriously degrade the cell performance (Fig. 3-3(a)). In addition, the cross-sectional image of solution deposition provides non-uniform and porous structure, with clear pinholes in plan-view (Fig. 3-3(b)). In contrast, the double-step deposition has more dense morphology with high uniformity (Fig. 3-3(c)). For the rational comparison, the

blocking layers were deposited with an equal thickness of for each deposition, which is an optimum value for sputtered TiO$_2$ as shown in Fig. 3-4. Transmittance was measured in Fig. 3-5. Both solution and sputter-deposited TiO$_2$ blocking layer obstructed a bit less than 60% of light at 300 nm region, where the transmission onset begins at 390 nm (bandgap of TiO$_2$ = 3.2 eV) [40]. On the other hand, the double-step deposition blocked approximately 90% of light, which indicates lower transmittance than that of sputter- or solution-based blocking layer. Also, solution-deposited TiO$_2$ shows some humps between 350 and 600 nm regions. These humps indicate the high roughness of film that addresses the poor quality of the film (also shown in Fig. 3-3(b)) [41]. Despite the compactness of the blocking layer, lower transmittance of double-step deposition can hinder the generation of photo-induced electrons under 350 nm region (bandgap region of TiO$_2$). However, the extent of solar irradiation is comparatively low under 350 nm, whereas the visible region has high solar irradiation [42]. Therefore, the detrimental effect of low wavelength region is negligible, and the compactness of TiO$_2$ is highly important with the satisfaction of good layer construction, efficient charge transport, and less possibility of carrier recombination in the solar cell.

	0 M	0.10 M	0.15 M	0.30 M	0.45 M
0 nm	✗	✗	3.60%	✗	✗
10 nm	✗	✗	5.15%	4.08%	✗
20 nm	✗	✗	6.10%	5.80%	✗
30 nm	4.28%	6.88%	12.31%	7.57%	6.27%
40 nm	✗	✗	6.86%	5.57%	4.84%
50 nm	✗	✗	6.54%	5.16%	4.45%

Table 3-1.   Optimization steps of PCE for the double-step deposition by tuning the

conditions of sputter (up to 50 nm) and solution (up to 0.45 M).
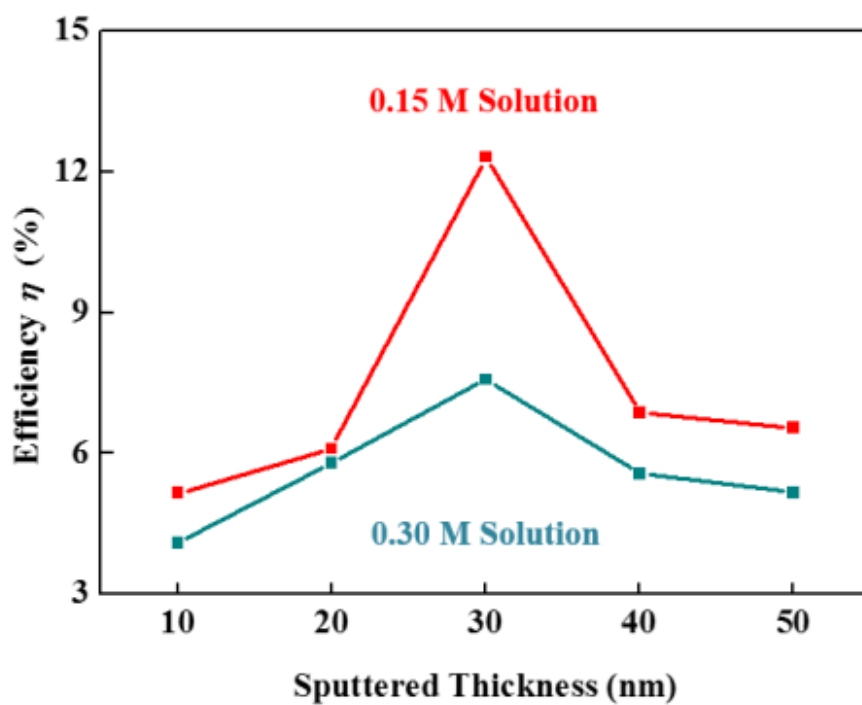
Fig. 3-1. Concentration control of a TiO_2 solution on the sputter-deposited TiO_2 to optimize the performance of perovskite solar cell (with hole-transporting material).
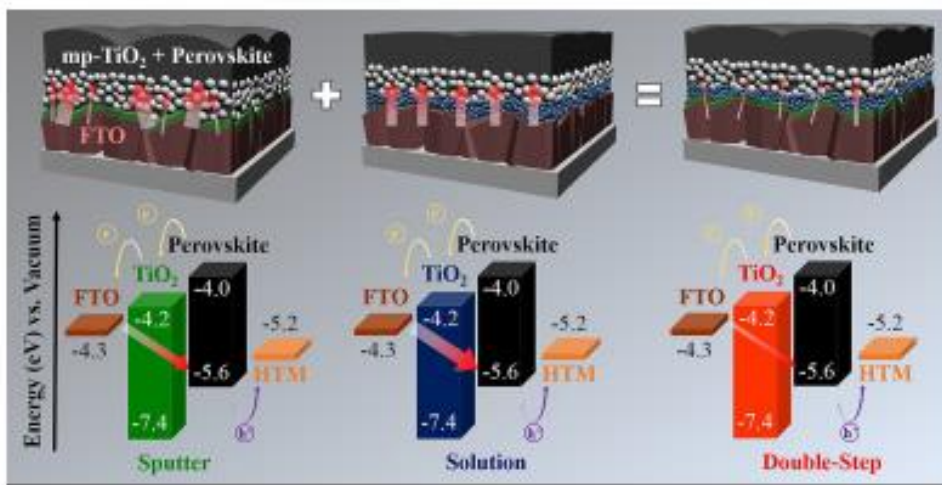
Fig. 3-2.   Schematics and energy diagrams of the solar cells with various TiO$_2$ blocking layers deposited by sputter, solution, or double-step method. Red arrows indicate the recombination phenomena of carriers.
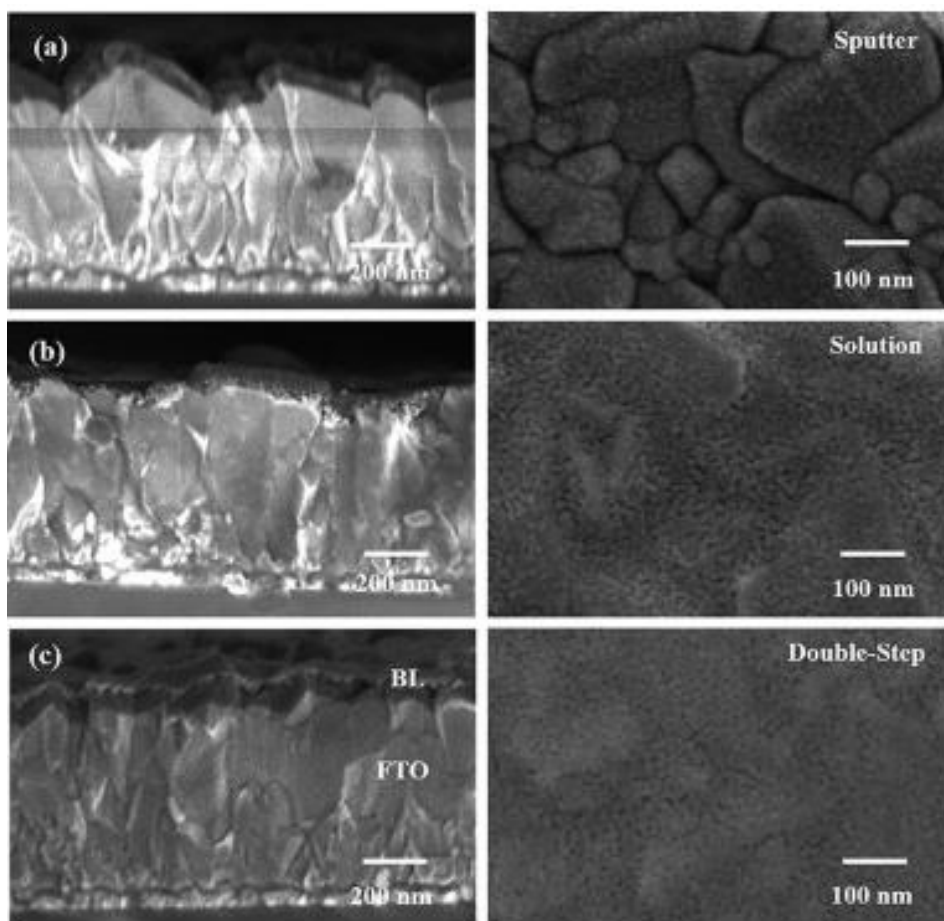
Fig. 3-3.　Cross-sectional and plan-view SEM images of blocking-layer TiO_2 by (a) sputter, (b) solution, and (c) double-step deposition.
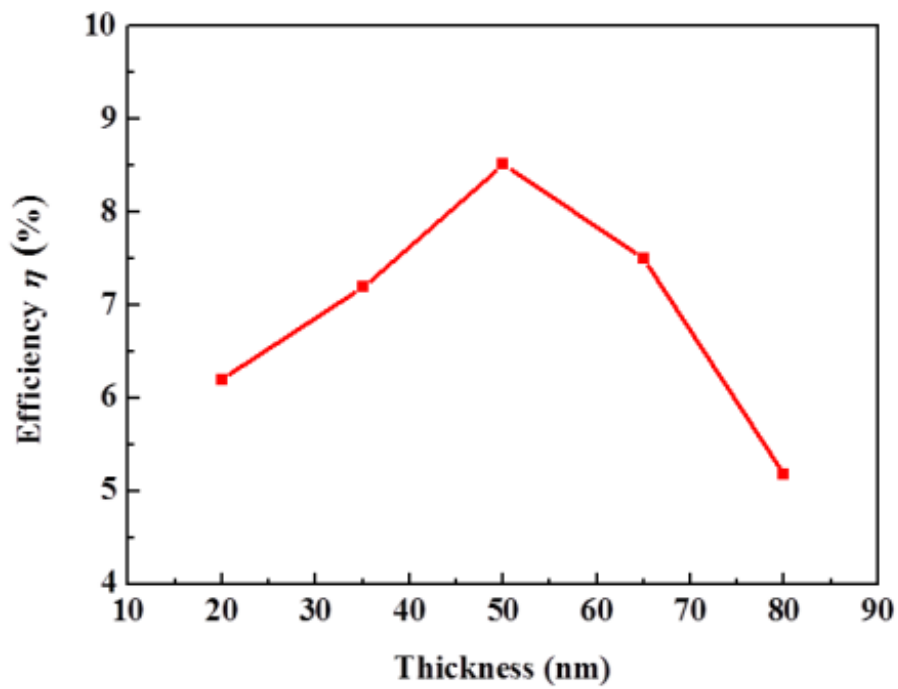
Fig. 3-4.   Performance optimization of the perovskite solar cell by varying

the thickness of sputter-deposited TiO_2.
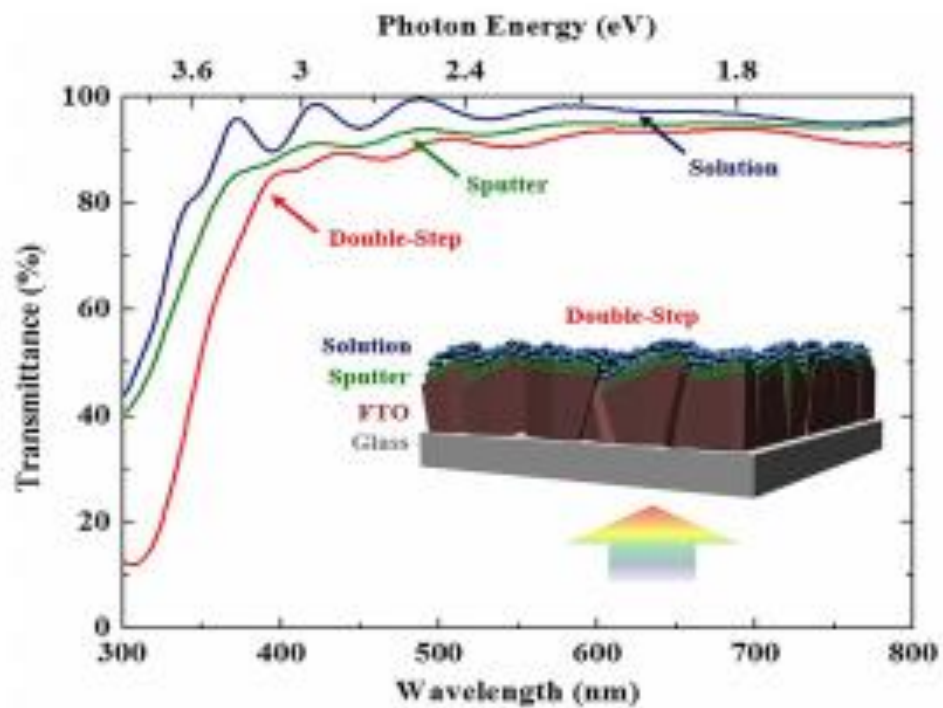
Fig. 3-5.　Transmittance from the differently deposited blocking layers (before the

solar-cell fabrication).

On top of the fabricated blocking layer, mp-TiO$_2$ layer was additionally deposited to transport electrons more efficiently from the perovskite [23,43]. The SEM images in Fig. 3-6 for each deposition present distinctive perovskite morphologies. As shown in Figs. 3-6(a) and (c), aggregated perovskite grains are constructed by stacking both on a side and top. Therefore, the sputter processed blocking layer yielding a rough semiconductor morphology (Fig. 3-6(a)), whereas solution deposition produced a smooth layer with few pinholes (Fig. 3-6(b)). With the double-step deposition, perovskite was more densely covered (Fig. 3-6(c)). To further confirm the roughness of film, atomic-force microscopy (AFM) is additionally conducted (Fig. 3-7), which revealed higher RMS roughness for the perovskite on the sputter-processed TiO$_2$ than others, and lowest RMS roughness in solution. Therefore, higher number of aggregated perovskite increased the RMS roughness due to the different grain-growth environment. As the double-step strategy exhibited distinctive morphologies for both blocking and perovskite layers, additional analyses were performed to advocate the synergetic effect of double-step deposition. Figure 3-8(a) illustrates X-ray diffraction of the perovskite with each blocking-layer method. The double-step deposition exhibited the highest crystallinity compared with either sputter or solution deposition (grain sizes of each condition is calculated in Table 3-2), and these phenomena can be addressed from the previous report that perovskite does not crystallize sufficiently on the FTO substrate [43-45]. Therefore, highly compact blocking TiO$_2$ layer by the double-step deposition can be a useful method to produce excellent quality of crystallized perovskite. Furthermore, the sputtering deposition resulted in the lowest transmittance, and the second lowest for the double-step (Fig. 3-8(b)). Due to the

aggregation phenomena of sputter and double-step shown in Fig. 3-6, perovskite layer by sputter deposition transmitted less light compared to that of double-step. However, since device performance does not depend solely on the light transmittance of photon absorber, further investigation of other layers and devices should be elucidated. To understand the effect of blocking layer in a solar cell performance, *J-V* curve was measured, and the highest PCE of 12.31% was achieved with the double-step deposition (Fig. 3-8(c), Table 3-3), and reproducibility is checked as shown in Table 3-4 and Fig. 3-9 (supplementary material). As shown in Fig. 3-8(d), EQE spectra of solar cells exhibited the highest value for the double-step deposition, especially at long wavelength region. Even though the light absorption in the sputter-based perovskite solar cell was higher than that in the double-step deposition, compactness of blocking layer and well-crystallized perovskite in the double-step based perovskite solar cell collects charge carriers better than that of sputter or solution. For the further investigation of devices, impedance spectroscopy was carried out under dark condition at various voltages (Fig. 3-10). Tendency of semi-circle at each voltage elucidates that the double-step has the highest recombination resistance, whereas solution reached the lowest (with the calculation values in Table 3-5). Conclusively, recombination resistance of double-step can be explained by the dense morphology of blocking and perovskite layer, and the solution process yielded the lowest resistance owing to its porous and pinhole structure of the blocking layer, which critically causes the carrier recombination. Additional Nyquist-plot data with the fitting profile are shown in Figs. 3-11 and 12.
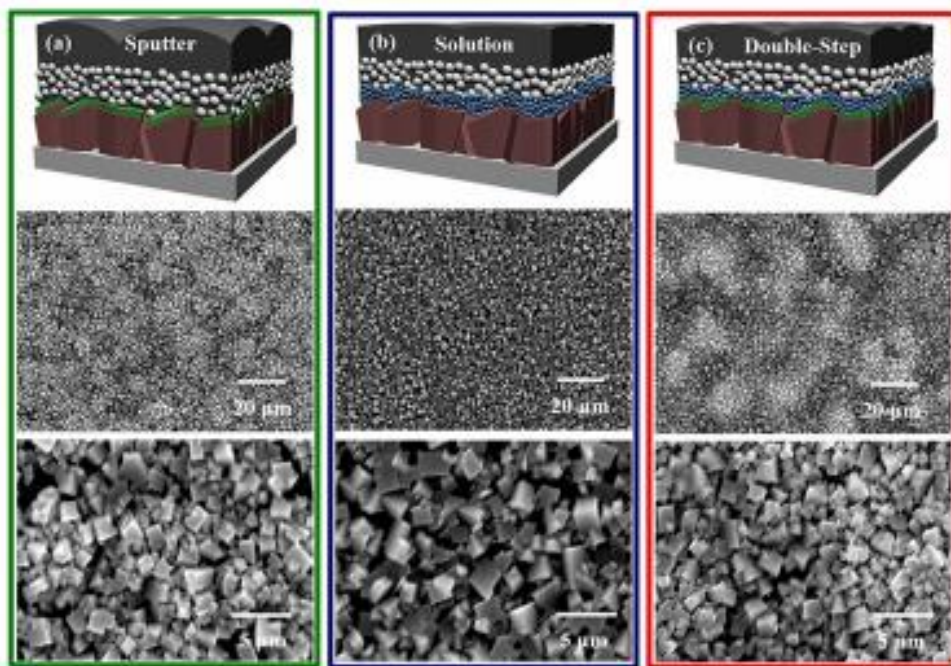
Fig. 3-6.   Schematics with top-view SEM images of MAPbI$_3$/mp-TiO$_2$/BL-TiO$_2$/FTO: (a) sputter, (b) solution, and (c) double-step deposition.
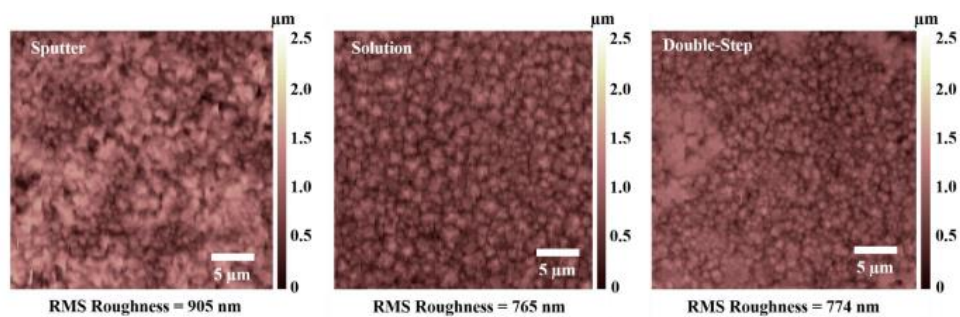
Fig. 3-7.   Topography maps and RMS values of the perovskite films obtained from
atomic-force microscopy (AFM).
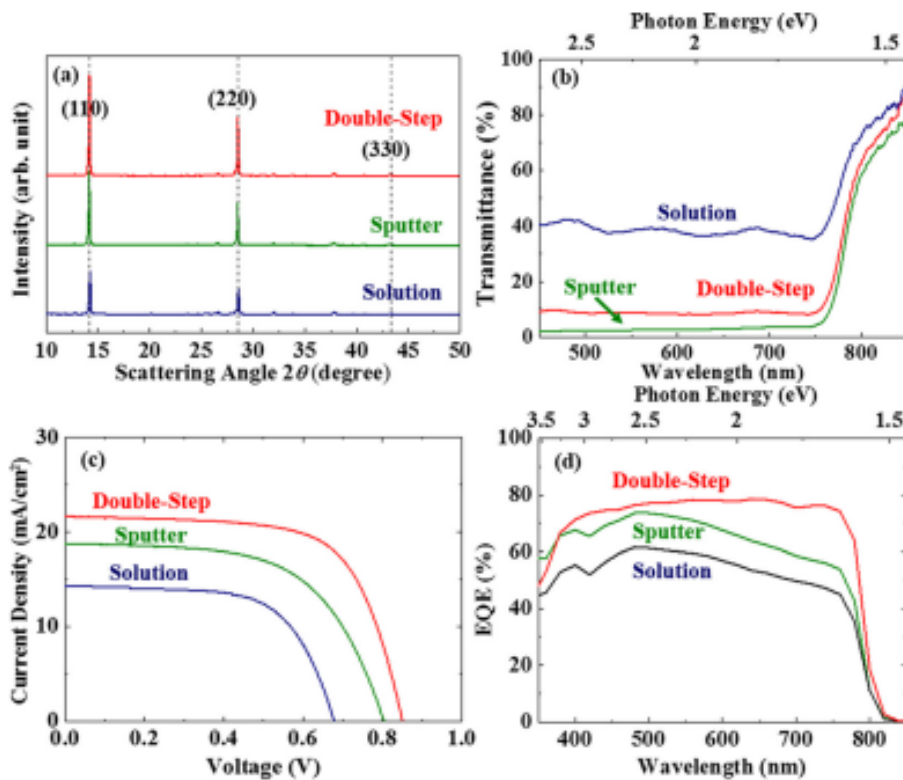
Fig. 3-8. Crystallinity and optoelectrical properties of MAPbI$_3$ devices on various blocking layers: (a) X-ray diffraction, (b) transmittance of MAPbI$_3$ films, (c) *J-V* curves (a scan rate of 10 V/s), and (d) EQE spectra of the perovskite solar cells.

	Sputter	Solution	Double-step
Grain size (nm)	102	51	299

Table 3-2.   Calculated grain size of perovskite using Scherrer equation.

	V_{oc} (V)	J_{sc} (mA/cm^2)	FF	η (%)
Sputter	0.80	18.74	0.60	8.96
Solution	0.68	14.22	0.64	6.23
Double-step	0.85	21.60	0.67	12.31

Table 3-3. Photovoltaic parameters of the perovskite solar cells from the highest

efficiency device by more than 5 cells in each condition (with details in

Tables 3-1 and Fig. 3-4).

	Sputter	Solution	Double-Step
1	7.56%	5.90%	10.24%
2	8.51%	6.23%	12.31%
3	6.82%	4.37%	10.78%
4	8.96%	4.40%	9.40%
5	7.42%	6.18%	9.83%

Table 3-4.   PCEs of MAPbI$_3$ perovskite solar cells from the sputtering, solution, and double-step deposition.
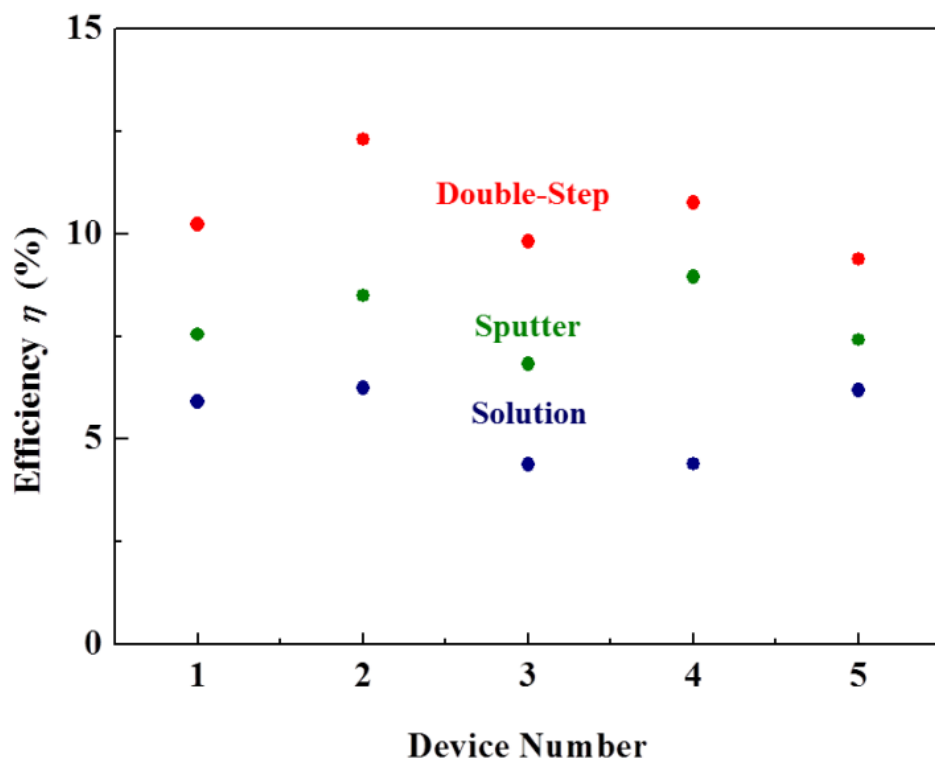
Fig. 3-9.   Device reproducibility of MAPbI$_3$ perovskite solar cells from the

sputtering, solution, and double-step deposition (as shown in Table 3-3).
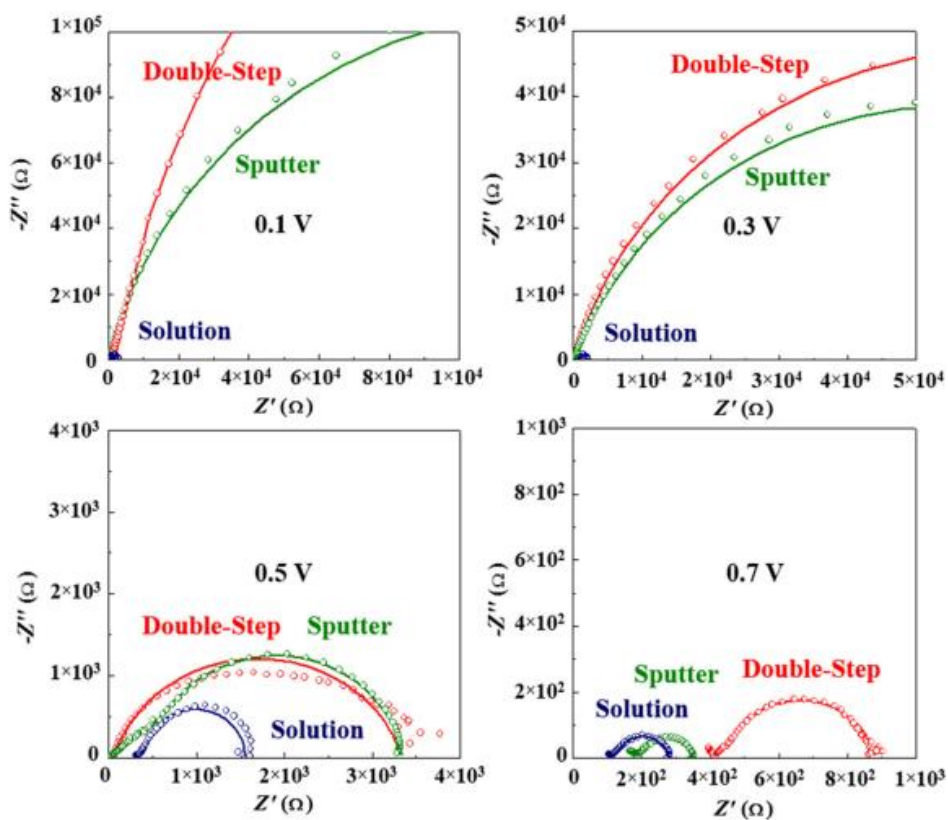
Fig. 3-10. Comparison of the impedance spectroscopy for differently fabricated perovskite solar cells (sputter, solution, and double-step methods) at various voltages (0.1, 0.3, 0.5, and 0.7 V under dark condition).
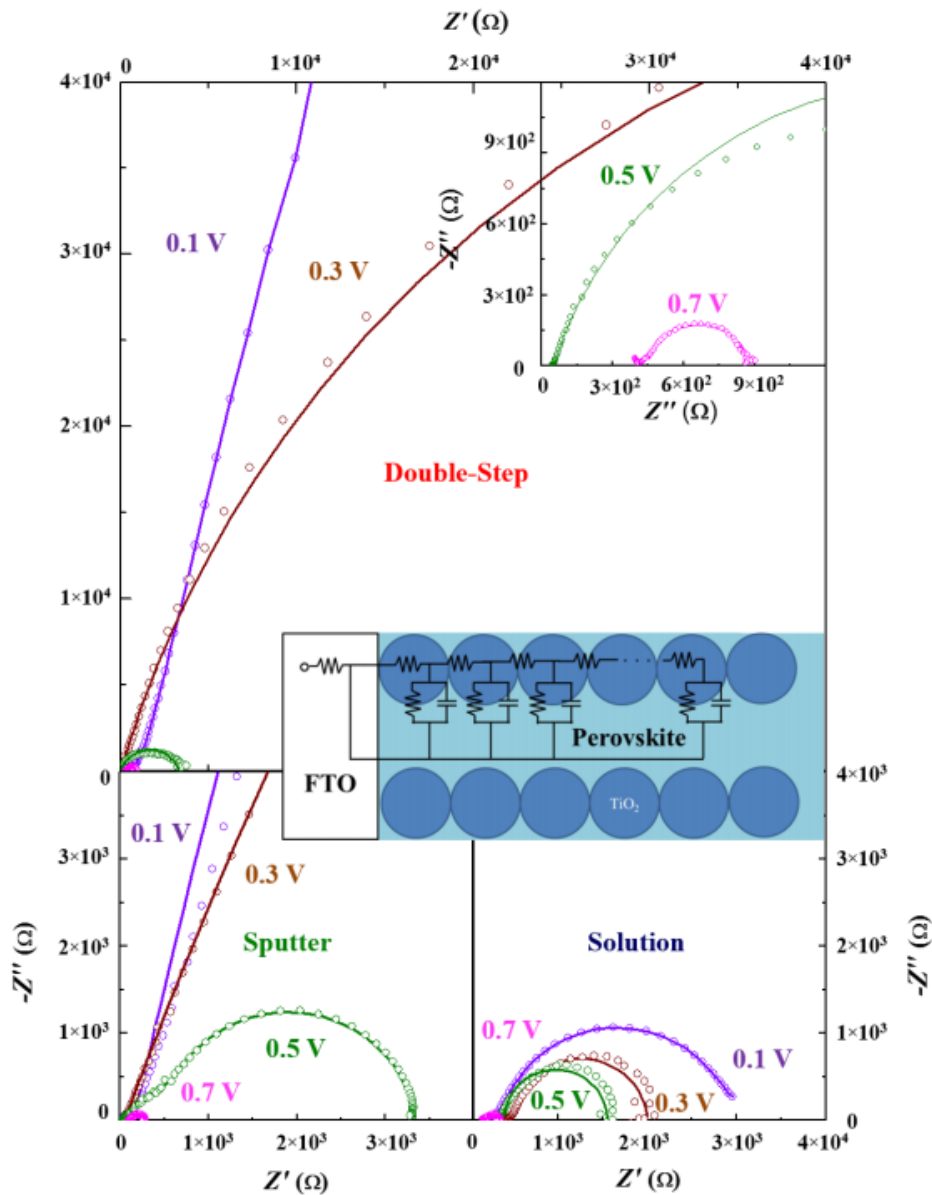
Fig. 3-11.   Nyquist plot and equivalent circuit model (under dark condition) of the
perovskite solar cells with different blocking layers (the inset presents a
magnified plot for the double-step blocking layer).
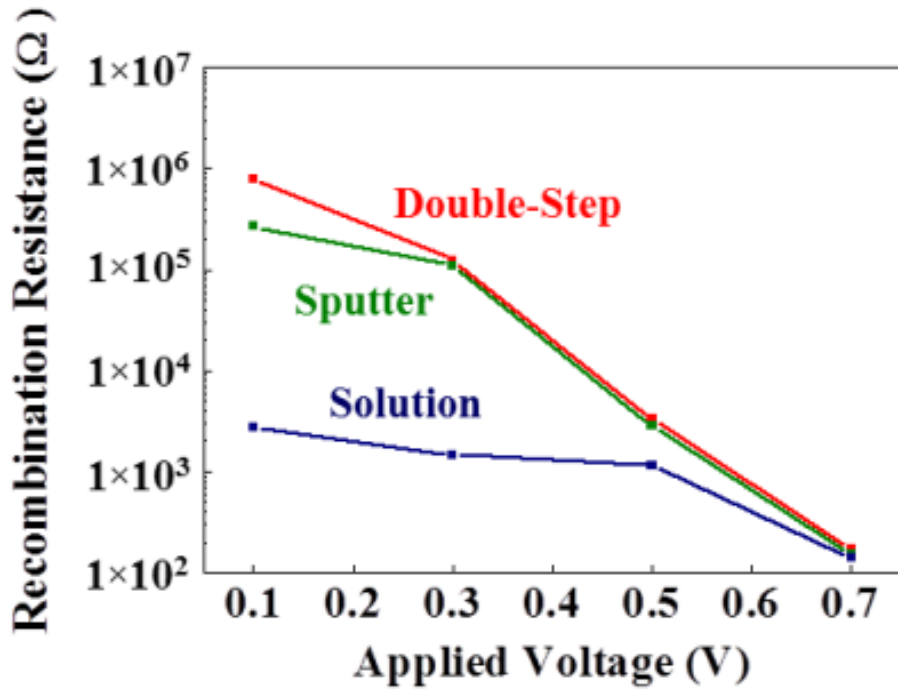
Fig. 3-12.　Recombination resistance (R_{rec}) of the perovskite solar cells under dark
　　　　condition.

3.4. Conclusions

In this article, we have proposed a straightforward double-step method, consisting sputter/solution deposition to synthesize highly compact blocking layer. As a result, the deposition achieved the highest recombination resistance and PCE when it was compared with the individual sputtering or solution scheme. With the outstanding transmittance of the double-step blocking layer, the improved crystallinity and morphology of the perovskite layer provided a positive impact on the solar cell performance. We are further investigating the utilization of smaller TiO_2 nanoparticles and uncomplicated route to construct more efficient blocking layer for higher solar-cell efficiency.

3.5. References

1. B. Shin, O. Gunawan, Y. Zhu, N. A. Bojarczuk, S. J. Chey, and S. Guha, "Thin Film Solar Cell with 8.4% Power Conversion Efficiency using an Earth-Abundant Cu_2ZnSnS_4 Absorber," *Prog. Photovoltaics* **21**, 72 (2013).

2. H. Choi, J. Kim, C. Nahm, C. Kim, S. Nam, J. Kang, B. Lee, T. Hwang, S. Kang, D. J. Choi, Y.-H. Kim, and B. Park, "The Role of ZnO-Coating-Layer Thickness on the Recombination in CdS Quantum-Dot-Sensitized Solar Cells," *Nano Energy* **2**, 1218 (2013).

3. D. U. Kim, C. M. Hangarter, R. Debnath, J. Y. Ha, C. R. Beauchamp, M. D. Widstrom, J. E. Guyer, N. Nguyen, B. Y. Yoo, and D. Josell, "Backcontact CdSe/CdTe Windowless Solar Cells," *Sol. Energy Mater. Sol. Cells* **109**, 246 (2013).

4. J. Kim, H. Choi, C. Nahm, C. Kim, S. Nam, S. Kang, D.-R. Jung, J. I. Kim, J. Kang, and B. Park, "The Role of a $TiCl_4$ Treatment on the Performance of CdS Quantum-Dot-Sensitized Solar Cells," *J. Power Sources* **220**, 108 (2012).

5. W. Lee, T. Hwang, S. Lee, S.-Y. Lee, J. Kang, B. Lee, J. Kim, T. Moon, and B. Park, "Organic-Acid Texturing of Transparent Electrodes toward Broadband Light Trapping in Thin-Film Solar Cells," *Nano Energy* **17**, 180 (2015).

6. H. Choi, C. Nahm, J. Kim, J. Moon, S. Nam, D.-R. Jung, and B. Park, "The Effect of $TiCl_4$-Treated TiO_2 Compact Layer on the Performance of Dye-Sensitized Solar Cell," *Curr. Appl. Phys.* **12**, 737 (2012).

7. B. Lee, S. Lee, D. Cho, J. Kim, T. Hwang, K. H. Kim, S. Hong, T. Moon, and B.

Park, "Evaluating the Optoelectronic Quality of Hybrid Perovskites by Conductive Atomic Force Microscopy with Noise Spectroscopy," *ACS Appl. Mater. Interfaces* **8**, 30985 (2016).

8. S. Lee, J. C. Flanagan, J. Kang, J. Kim, M. Shim, and B. Park, "Integration of $CdSe/CdSe_xTe_{1-x}$ Type-II Heterojunction Nanorods into Hierarchically Porous TiO_2 Electrode for Efficient Solar Energy Conversion," *Sci. Rep.* **5**, 17472 (2015).

9. B. Lee, J. I. Kim, S. Lee, T. Hwang, S. Nam, H. Choi, K. Kim, J. Kim, and B. Park, "Oriented Hierarchical Porous TiO_2 Nanowires on Ti Substrate: Evolution of Nanostructures for Dye-Sensitized Solar Cells," *Electrochim. Acta* **145**, 231 (2014).

10. H. Choi, T. Hwang, S. Lee, S. Nam, J. Kang, B. Lee, and B. Park, "The Construction of Tandem Dye-Sensitized Solar Cells from Chemically-Derived Nanoporous Photoelectrodes," *J. Power Sources* **274**, 937 (2015).

11. A. Kojima, K. Teshima, Y. Shirai, and T. Miyasaka, "Organometal Halide Perovskites as Visible-Light Sensitizers for Photovoltaic Cells," *J. Am. Chem. Soc*. **131**, 6050 (2009).

12. T. Moon, G. S. Shin, and B. Park, "Recent Advances in the Transparent Conducting ZnO for Thin-Film Si Solar Cells," *Electron. Mater. Lett.* **11**, 917 (2015).

13. H. Woo, J. Kang, J. Kim, C. Kim, S. Nam, and B. Park, "Development of Carbon-Based Cathodes for Li-Air Batteries: Present and Future," *Electron. Mater. Lett*.

12, 551 (2016).

14. H. J. Snaith, "Perovskites: The Emergence of a New Era for Low-Cost, High-Efficiency Solar Cells," *J. Phys. Chem. Lett*. **4**, 3623 (2013).

15. M. D. McGehee, "Materials science: Fast-track solar cells," *Nature* **501**, 323 (2013).

16. G. Hodes, "Perovskite-Based Solar Cells," *Science* **342**, 317 (2013).

17. C. S. Ponseca, Jr., T. J. Savenije, M. Abdellah, K. Zheng, A. Yartsev, T. Pascher, T. Harlang, P. Chabera, T. Pullerits, A. Stepanov, J.-P. Wolf, and V. Sundstrom, "Organometal Halide Perovskite Solar Cell Materials Rationalized: Ultrafast Charge Generation, High and Microsecond-Long Balanced Mobilities, and Slow Recombination," *J. Am. Chem. Soc*. **136**, 5189 (2014).

18. J. M. Frost, K. T. Butler, F. Brivio, C. H. Hendon, M. v. Schilfgaarde, and A. Walsh, "Atomistic Origins of High-Performance in Hybrid Halide Perovskite Solar Cells," *Nano Lett.* **14**, 2584 (2014).

19. R. F. Service, "Perovskite Solar Cells Gear up to go Commercial," *Science* **354**, 1214 (2016).

20. W.-J. Yin, J.-H. Yang, J. Kang, Y. Yan, and S.-H. Wei, "Halide Perovskite Materials for Solar Cells: a Theoretical Review," *J. Mater. Chem. A* **3**, 8926 (2015).

21. J. H. Heo, S. H. Im, J. H. Noh, T. N. Mandal, C.-S. Lim, J. A. Chang, Y. H. Lee, H.-J. Kim, A. Sarkar, M. K. Nazeeruddin, M. Grattzel, and S. I. Seok, "Efficient Inorganic-Organic Hybrid Heterojunction Solar Cells Containing Perovskite

Compound and Polymeric Hole Conductors," *Nat. Photonics* **7**, 486 (2013).

22. F. Wang, M. Endo, S. Mouri, Y. Miyauchi, Y. Ohno, A. Wakamiya, Y. Murata, and K. Matsuda, "Highly Stable Perovskite Solar Cells with an All-Carbon Hole Transport Layer," *Nanoscale* **8**, 11882 (2016).

23. J. Choi, S. Song, M. T. H€orantner, H. J. Snaith, and T. Park, "Well-Defined Nanostructured, Single-Crystalline TiO2 Electron Transport Layer for Efficient Planar Perovskite Solar Cells," *ACS Nano* **10**, 6029 (2016).

24. W. Ke, G. Fang, J. Wan, H. Tao, Q. Liu, L. Xiong, P. Qin, J. Wang, H. Lei, G. Yang, M. Qin, X. Zhao, and Y. Yan, "Efficient Hole-Blocking Layer-Free Planar Halide Perovskite Thin-Film Solar Cells," *Nat. Commun.* **6**, 6700 (2015).

25. J. Kim, T. Hwang, S. Lee, B. Lee, J. Kim, G. S. Jang, S. Nam, and B. Park, "Solvent and Intermediate Phase as Boosters for the Perovskite Transformation and Solar Cell Performance," *Sci. Rep.* **6**, 25648 (2016).

26. K. Wojciechowski, M. Saliba, T. Leijtens, A. Abate, and H. J. Snaith, "Sub-150 °C Processed Meso-Superstructured Perovskite Solar Cells with Enhanced Efficiency," *Energy Environ. Sci.* **7**, 1142 (2014).

27. H.-H. Wang, Q. Chen, H. Zhou, L. Song, Z. S. Louis, N. D. Marco, Y. Fang, P. Sun, T.-B. Song, H. Chen, and Y. Yang, "Improving the TiO_2 Electron Transport Layer in Perovskite Solar Cells using Acetylacetonate-Based Additives," *J. Mater. Chem. A* **3**, 9108 (2015).

28. S. Hong, A. Han, E. C. Lee, K.-W. Ko, J.-H. Park, H.-J. Song, M.-H. Han, and C.-H. Han, "A Facile and Low-Cost Fabrication of TiO_2 Compact Layer for

Efficient Perovskite Solar Cells," *Curr. Appl. Phys*. **15**, 574 (2015).

29. F. Giordano, A. Abate, J. P. C. Baena, M. Saliba, T. Matsui, S. H. Im, S. M. Zakeeruddin, M. K. Nazeeruddin, A. Hagfeldt, and M. Gratzel, "Enhanced Electronic Properties in Mesoporous TiO_2 via Lithium Doping for High-Efficiency Perovskite Solar Cells," *Nat. Commun*. **7**, 10379 (2016).

30. Y. Wu, X. Yang, H. Chen, K. Zhang, C. Qin, J. Liu, W. Peng, A. Islam, E. Bi, F. Ye, M. Yin, P. Zhang, and L. Han, "Highly Compact TiO_2 Layer for Efficient Hole-Blocking in Perovskite Solar Cells," *Appl. Phys. Express* **7**, 052301 (2014).

31. L. Chen, J.-R. Wang, L.-Q. Xie, C. Zhan, Z. Qiu, J.-Z. Zhou, J.-W. Yan, B.-W. Mao, and Z.-Q. Tian, "Compact Layer Influence on Hysteresis Effect in Organic-Inorganic Hybrid Perovskite Solar Cells," *Electrochem. Commun.* **68**, 40 (2016).

32. H. Hu, B. Dong, H. Hu, F. Chen, M. Kong, Q. Zhang, T. Luo, L. Zhao, Z. Guo, J. Li, Z. Xu, S. Wang, D. Eder, and L. Wan, "Atomic Layer Deposition of TiO_2 for a High-Efficiency Hole-Blocking Layer in Hole-Conductor-Free Perovskite Solar Cells Processed in Ambient Air," *ACS Appl. Mater. Interfaces* **8**, 17999 (2016).

33. M. Leskela and M. Ritala, "Atomic Layer Deposition Chemistry: Recent Developments and Future Challenges," *Angew. Chem. Int. Ed.* **42**, 5548 (2003).

34. S. Ge, H. Xu, W. Wang, R. Cao, Y. Wu, W. Xu, J. Zhu, F. Xue, F. Hong, R. Xu, F. Xu, L. Wang, and J. Huang, "The Improvement of Open Circuit Voltage by the Sputtered TiO_2 Layer for Efficient Perovskite Solar Cell," *Vacuum* **128**, 91 (2016).

35. S. H. Kang, J.-W. Lim, H. S. Kim, J.-Y. Kim, Y.-H. Chung, and Y.-E. Sung, "Photo and Electrochemical Characteristics Dependent on the Phase Ratio of Nanocolumnar Structured TiO2 Films by RF Magnetron Sputtering Technique," *Chem. Mater*. **21**, 2777 (2009).

36. T. Hwang, D. Cho, J. Kim, J. Kim, S. Lee, B. Lee, K. H. Kim, S. Hong, C. Kim, and B. Park, "Investigation of Chlorine-Mediated Microstructural Evolution of $CH_3NH_3PbI_3(Cl)$ Grains for High Optoelectronic Responses," *Nano Energy* **25**, 91 (2016).

37. V. Stranak, J. Kratochvil, J. Olejnicek, P. Ksirova, P. Sezemsky, M. Cada, and Z. Hubicka, "Enhanced Oxidation of TiO_2 Films Prepared by High Power Impulse Magnetron Sputtering Running in Metallic Mode," *J. Appl. Phys*. **121**, 171914 (2017).

38. P. Wang, Z. Shao, M. Ulfa, and T. Pauporte, "Insights into the Hole Blocking Layer Effect on the Perovskite Solar Cell Performance and Impedance Response," *J. Phys. Chem. C* **121**, 9131 (2017).

39. C. Nahm, H. Choi, J. Kim, S. Byun, S. Kang, T. Hwang, H. H. Park, J. Ko, and B. Park, "A Simple Template-Free 'Sputtering Deposition and Selective Etching' Process for Nanoporous Thin Films and Its Application to Dye-Sensitized Solar Cells," *Nanotechnology* **24**, 365604 (2013).

40. N. J. Jeon, J. H. Noh, Y. C. Kim, W. S. Yang, S. Ryu, and S. I. Seok, "Solvent engineering for high-performance inorganic-organic hybrid perovskite solar cells," *Nat. Mater*. **13**, 897 (2014).

41. R. Swanepoel, "Determination of Surface Roughness and Optical Constants of Inhomogeneous Amorphous Silicon Films," *J. Phys. E: Sci. Instrum.* **17**, 896 (1984).

42. C. A. Gueymard, "The Sun's Total and Spectral Irradiance for Solar Energy Applications and Solar Radiation Models," *Sol. Energy* **76**, 423 (2004).

43. J. Burschka, N. Pellet, S.-J. Moon, R. Humphry-Baker, P. Gao, M. K. Nazeeruddin, and M. Gratzel, "Sequential Deposition as a Route to High-Performance Perovskite-Sensitized Solar Cells," *Nature* **499**, 316 (2013).

44. L. Huang, J. Xu, X. Sun, Y. Du, H. Cai, J. Ni, J. Li, Z. Hu, and J. Zhang, "Toward Revealing the Critical Role of Perovskite Coverage in Highly Efficient Electron-Transport Layer-Free Perovskite Solar Cells: An Energy Band and Equivalent Circuit Model Perspective," *ACS Appl. Mater. Interfaces* **8**, 9811 (2016).

45. Z. Ren, A. Ng, Q. Shen, H. C. Gokkaya, J. Wang, L. Yang, W.-K. Yiu, G. Bai, A. B. Djurisic, W. W.-f. Leung, J. Hao, W. K. Chan, and C. Surya, "Thermal Assisted Oxygen Annealing for High Efficiency Planar $CH_3NH_3PbI_3$ Perovskite Solar Cells," *Sci. Rep.* **4**, 6752 (2014).

Chapter 4.

An Aromatic Diamine Molecule as the *A*-Site Solute for Highly Durable and Efficient Perovskite Solar Cells

4.1. Introduction

Perovskite solar cells (PSCs) have been introduced with enormous attention due to its advantages of low fabrication cost and high efficiencies, with intrinsic characteristics of appropriate electronic structures, small exciton binding energy, and balanced ambipolar charge transport properties, yielding a high power conversion efficiency (PCE) of 23.3% in 2018 [1–11]. Although pioneer researches have established high PCEs which can be competitive with commercialized solar cells, device and materials stabilities of PSCs are not yet satisfactory. $CH_3NH_3PbI_3$ (MAPbI$_3$) is one of the most studied perovskite materials, and the degradation mechanisms of MAPbI$_3$ extend to several factors. First, moisture from atmosphere destroys the perovskite structure due to the high organic reactivity of MAPbI$_3$, which implies that devices cannot operate under highly humid conditions [12–15]. Second, light is a critical degradation factor for the PSC operation. With photons absorbed, several chemical modifications occur inside the perovskite material, such as and peroxide formation, leading to degradations of the perovskite material and devices [1,15,16]. Lastly, thermally induced degradation can occur while the device is under operation conditions (≈ 90 °C), because MA$^+$ in MAPbI$_3$ is sensitive

to heat energy due to its high reactivity and volatility [17–21].

To prevent the degradation of MAPbI$_3$, various techniques have been introduced by the modification of halide, metal, and organic substitutions. Sang Il Seok's group introduced halide substitution with Br to obtain high stability of PSC by increased bond energy and reduced distortion of the octahedron framework [21]. Since then, various anions, such as Cl, NO$_3$, OAc (OAc = CH$_3$CH$_2$COO$^-$), etc., have been introduced into the perovskite to reduce material defects and enhance the device stability [22–25]. Moreover, metal substitution in the perovskite has been widely investigated using Bi, Sn, Sb, etc [26–29].

While organic-cation modifications have been actively explored to improve the stability of PSCs [30–34], substitution of the cation is relatively limited due to its size within the ABX$_3$ lattice, sometimes leading to phase transformations from a 3D to 2D perovskite, and resulting in a high band gap and poor solar cell device performances [34–36]. Therefore, exploring an ideal cation with superior stability and device performance is a key challenge at the current stage. While passivation of imidazolium cation in perovskite has been recently reported to improve the crystallinity and light stability [37], alloying effect and device stability are to be explored and improved. Herein, we demonstrate imidazole-soluted perovskites to increase both the PCE and stability of PSCs. Imidazole (IZ) has a reasonable ionic radius of 258 pm with an aromatic structure, allowing good solid solution with MAPbI$_3$.

Moreover, the diammonium molecule can provide additional hydrogen

bonding for a stable material [38–40], and due to the delocalized π orbital of IZ with hydrogen bonding in a I–Pb cage, it may allow low reactivity with its surroundings leading to additional electrical conductivity. Thereby, the devices with IZ-alloyed MAPbI$_3$ have achieved reverse PCEs up to 20.2% with outstanding stability from light-, air-, and heat-induced environments. Furthermore, devices with IZ solute in MAPbI$_3$ are measured with a large active area of 2 cm^2 and exhibited a high PCE of 16.8%, suggesting IZ alloying is an ideal strategy for high quality devices.

4.2. Experimental Section

Synthesis of Imidazole-Soluted Perovskite: Imidazole ($C_3H_4N_2$, Aldrich) was mixed with a hydrogen iodide solution (Aldrich) with a 3:1 molar ratio in a round-bottom flask at 0°C for 2 h under stirring. After the solvent was evaporated at 70°C for 12 h, the precipitate was washed with diethyl ether (Daejung) for six times. The precipitate was dried at 60°C for 24 h in a vacuum oven to complete the synthesis of imidazolium iodide (C3H5N2I).

1.5 m of imidazolium iodide and PbI_2 (Alfa Aesar) were mixed in N,Ndimethylformamide (DMF, Aldrich)/dimethyl sulfoxide (DMSO, Aldrich) solution (volume ratio of 9:1) to prepare the stock solution of IZ_2PbI_4. Then, 1.5 m of MAI (Solaronix) and PbI_2 were mixed in the DMF/ DMSO solution (volume ratio of 9:1) to prepare the solution of $MAPbI_3$. Lastly, 2.5%, 5.0%, and 7.5% (molar percent) of the IZ_2PbI_4 solution were added to the $MAPbI_3$ solution to complete the preparation of the IZ-alloyed $MAPbI_3$ precursor solution.

Device Fabrication: For the TiO_2-based mesoscopic devices, fluorine-doped tin oxide substrates (FTO, TEC 8:Pilkington) were cleaned by sonication in acetone (Daejung), ethanol (Daejung), and deionized (DI) water sequentially. The TiO_2 blocking layer (bl-TiO_2) was deposited by spin-coating a mixture solution of 0.15 M titanium diisopropoxide bis(acetylacetonate) (75.0 wt% in isopropanol, Aldrich) and 1-butanol (Aldrich), and the films were annealed at 150°C for 30 min. Mesoporous TiO_2 (mp-TiO_2) paste (30NR-D, Solaronix) was diluted in ethanol (150 mg mL^{-1}), and then spin-coated on a bl-TiO_2/FTO substrate, and the films were annealed at

500°C for 60 min. For the SnO₂-based planar devices, indium-doped tin oxide substrates (ITO) were cleaned with the same step as FTO. Afterwards, a SnO_2 colloidal particle solution (15 wt% in water, Alfa Aesar) was diluted to 2.5% with DI water, and then spin coated on the ITO substrate followed by annealing at 130°C for 30 min. The prepared IZ-alloyed $MAPbI_3$ solution was then spinc-oated at 3000 rpm for 20 s (with diethyl ether used as an antisolvent). The HTM was prepared by mixing 72.3 mg mL^{-1} of spiro-OMeTAD (Lumtec) in chlorobenzene (Aldrich) with 28.8 µL of tert-butylpyridine (Aldrich). Separately, another solution was prepared by dissolving bis(trifluoromethylsulfonyl)imide salt (Aldrich) in acetonitrile (Aldrich) with 520 mg mL^{-1} concentration. Then, 17.5 µL of prepared lithium bis(trifluoromethylsulfonyl)imide salt solution was transferred to spiro-OMeTAD solution to complete the preparation of hole transporting material. The solution was deposited on a film with a spin-coating method. Finally, 100 nm thick Au electrodes were thermally evaporated.

Characterization: The field-emission scanning electron microscope (Merlin-Compact: Carl Zeiss) was used to observe the morphologies of $MAPbI_3$. The phases of the synthesized samples were characterized by X-ray diffraction (XRD; D8 Advance: Bruker). FTIR (Nicolet iS50: Thermo Fisher Scientific) was conducted to characterize the organic bonding nature of the perovskite. To determine the work function of IZ-soluted perovskites, UPS was measured at beamline 4D of Pohang Light Source II (PLS II), Korea. The conductivity measurements were carried out by 4-point probe (CMT-SR1000N: Chang Min Co. LTD.) on the perovskite/glass

substrate.   The photocurrent–voltage (J–V) curves and steady-state current of MAPbI$_3$ perovskite solar cells were obtained with a potentiostat (CHI 608C; CH Instrumental Inc.) under AM 1.5 at $100\,\mathrm{mW\,cm^{-2}}$ (K3000; McScience Inc.).   Active area of devices were defined using Al mask with $0.09\,\mathrm{cm^2}$ square aperture, and an Si reference cell (K801S-K15; McScience Inc.) was used for calibration.   The absorbance spectra of MAPbI$_3$ was recorded on a UV–vis spectrophotometer (Lambda 20; Perkin Elmer, calibrated with TiO$_2$/glass substrate), and an external quantum efficiency (EQE) measurement system (K3100; McScience Inc.) was used to obtain the EQE spectra (calibrated with Si reference cell, S1337; Hamamatsu Photonics).   Heat-induced degradation was measured with TGA (Discovery TGA: TA Instruments). Initial condition of samples and experiments were set as 25°C with ≈55% humidity in air.

4.3. Results and Discussion

Stability issues of organometallic perovskite cells are one of the major limitations for commercialization, due to the volatile and reactive nature of organic cation MA [17–19]. Imidazole (IZ) has an aromatic structure, which allows high stability due to the delocalized bonding within the molecule. Also, IZ contains diammonium network, allowing additional hydrogen bonding within the PbI_6^{4-} framework (N-H-I-Pb), and can stabilize the perovskite structure [40]. However, the size of IZ^+ (258 pm) is larger than MA^+ (217 pm), possibly leading to 2D perovskite formation [37]. Previously reported large cations (phenylethylamine, ethylamine, etc.) lead to the formation of 2D perovskites with poor device performance and high band gaps [33–36]. To synthesize 3D perovskite structure, IZ should be properly alloyed with smaller molecules (MA) to satisfy Goldschmidt Tolerance Factor [41]. Additionally, recent studies suggesting the ideal design of perovskite for solar cells have shown that cation-alloyed perovskite provides improved optoelectronic behavior with the advantages of bonding and conductive nature [30,43a,b]. Likewise, IZ has diamine and aromatic framework, guaranteeing the hydrogen bonding and conductivity improvements to increase the device performance [30,42,44,45]. Therefore, IZ-alloyed $MAPbI_3$ has a potential to outperform the pristine $MAPbI_3$.

Figure 4-1 schematically illustrates the formation of IZ-based perovskite (IZ_2PbI_4) and IZ-alloyed $MAPbI_3$ (with diffraction and Fourier-transform infrared spectroscopy (FTIR) in Fig. 4-2; synthesis temperature of $\approx$ 60 °C). Although

IZ$_2$PbI$_4$ exhibits a reasonable work function to operate the device, the perovskite turns into a 2D structure, and exhibits a very high band gap (≈ 2.88 eV) which is not suitable as a light absorbing material (Fig. 4-3). Therefore, IZ alloying (2.5%, 5.0%, and 7.5% IZ, molar percent) with MAPbI$_3$ leads to the formation of a new category of perovskite light absorbers with high stability and optoelectronic properties, while 10% of IZ has produced a secondary phase, as shown in Fig. 4-4. It should be noted that IZ was also soluted in FAPbI$_3$ and compared with the MAPbI$_3$ alloy (Fig. 4-5). As shown in Fig. 4-5, diffraction peaks of FAPbI$_3$ and MAPbI$_3$ substituted with higher content of IZ are separated into individual peaks of ABX$_3$ and IZ$_2$PbI$_4$, indicating that alloying with high content of IZ is limited. Due to the high thermodynamic barrier of FAPbI$_3$, [40] an FA-alloyed IZ$_2$PbI$_4$ phase is likely to be produced, not IZ-alloyed FAPbI$_3$ (which is an unfavorable phase in photovoltaic research due to the production of a high band gap material).

Diffraction data confirm proper alloying of IZ in MAPbI$_3$, with increment of the lattice parameter without any secondary phases (Fig. 4-6(a); Fig. 4-7). Moreover, the FTIR peaks in Fig. 4-6(b) address the existence of IZ in the lattice. Since bond strengths of aromatic compounds are stronger than linear structures, N–H (stretch) of IZ is detected in a frequency region of ≈ 3330 cm^{-1}, where the N–H (stretch) of MA is reported in a region of ≈ 3250 cm^{-1} (Fig. 4-8). Moreover, the peak intensities of C=C and N=C are also increased in a frequency region of ≈ 1580 cm^{-1} due to the presence of delocalized π bonding in IZ. Interestingly, major peaks of MAPbI$_3$ in FTIR, C–N (stretch) at ≈ 900 cm^{-1} and NH$_3$ (bend) at ≈ 1500 cm^{-1} in

Fig. 4-8, have shifted to higher energy with IZ alloying, indicating that the bond strength of the organic cation within the perovskite structure has increased. Moreover, less volatile IZ^+ (compared to MA^+) can provide better phase stabilization with reduced evaporation of organic cations (under the annealing step), while the molar ratios of carbon versus lead have dominant carbon contents when IZ is soluted in $MAPbI_3$ (Fig. 4-9).
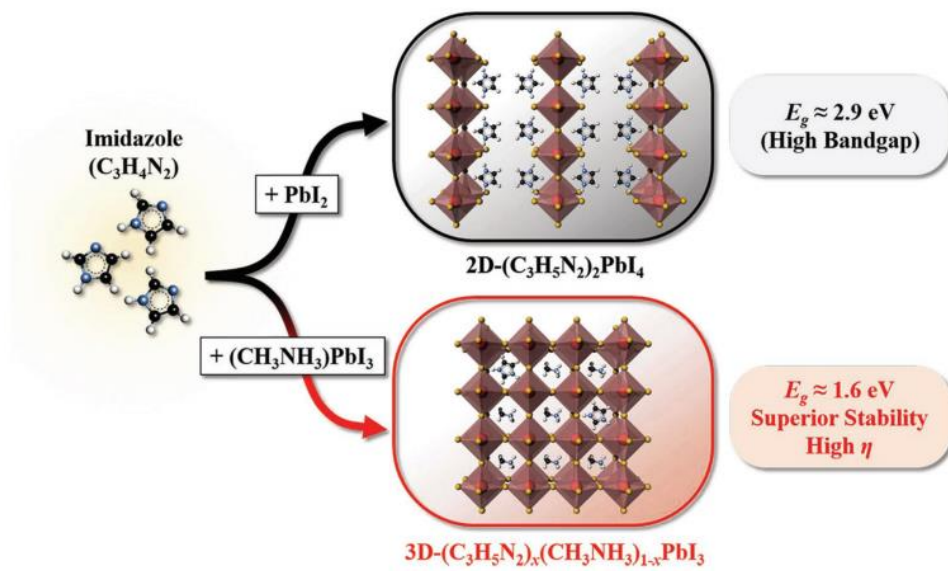
Fig. 4-1. Schematic illustration for structural transformations in the imidazole incorporated perovskite. Perovskite with 100% imidazole cation leads 2.9 eV of high band gap, which is not sufficient for solar-light absorber. Therefore, imidazole is soluted in $CH_3NH_3PbI_3$ to satisfy the requirements for perovskite solar cells.
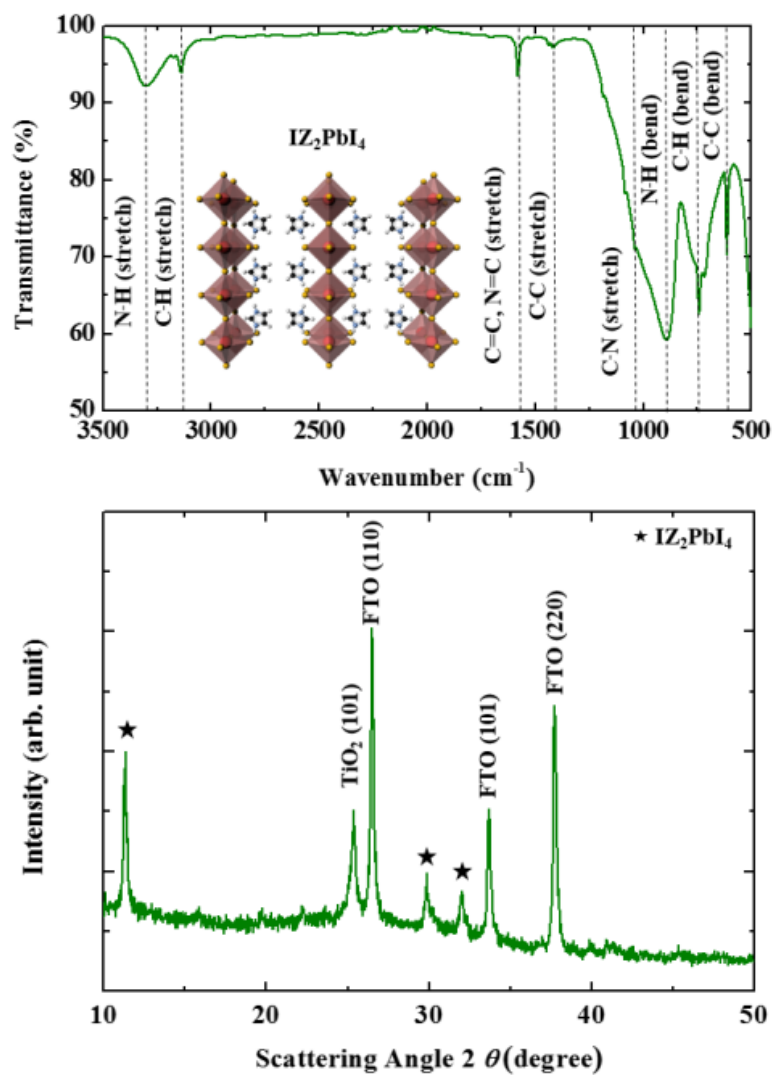
Fig. 4-2. FTIR spectra and x-ray diffraction analysis for the characterization of IZ$_2$PbI$_4$.
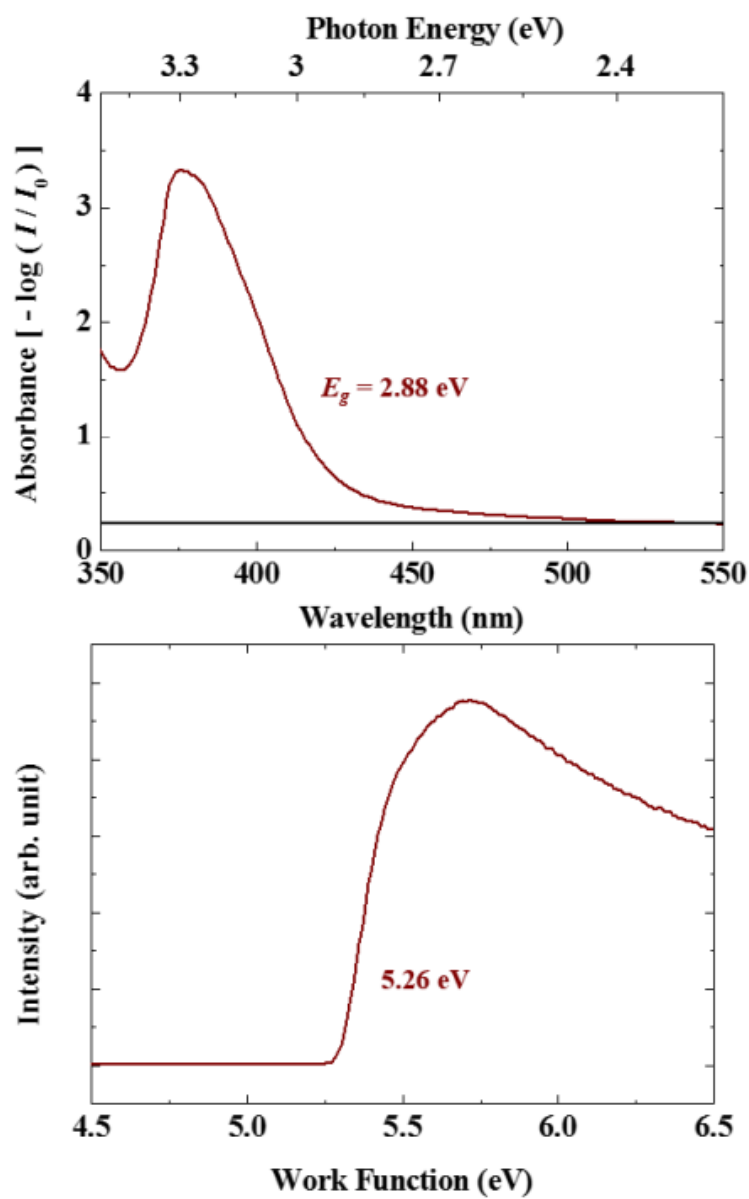
Fig. 4-3.   Absorbance and work function of IZ_2PbI_4 on a TiO_2/FTO substrate.
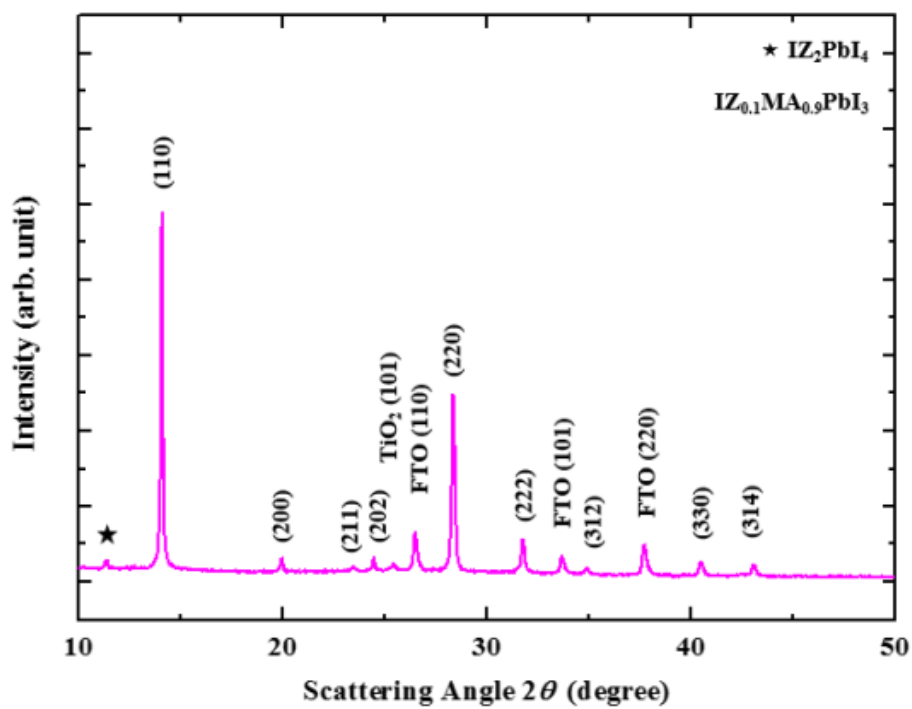
Fig. 4-4.   X-ray diffraction of the $IZ_{0.1}MA_{0.9}PbI_3$ film.
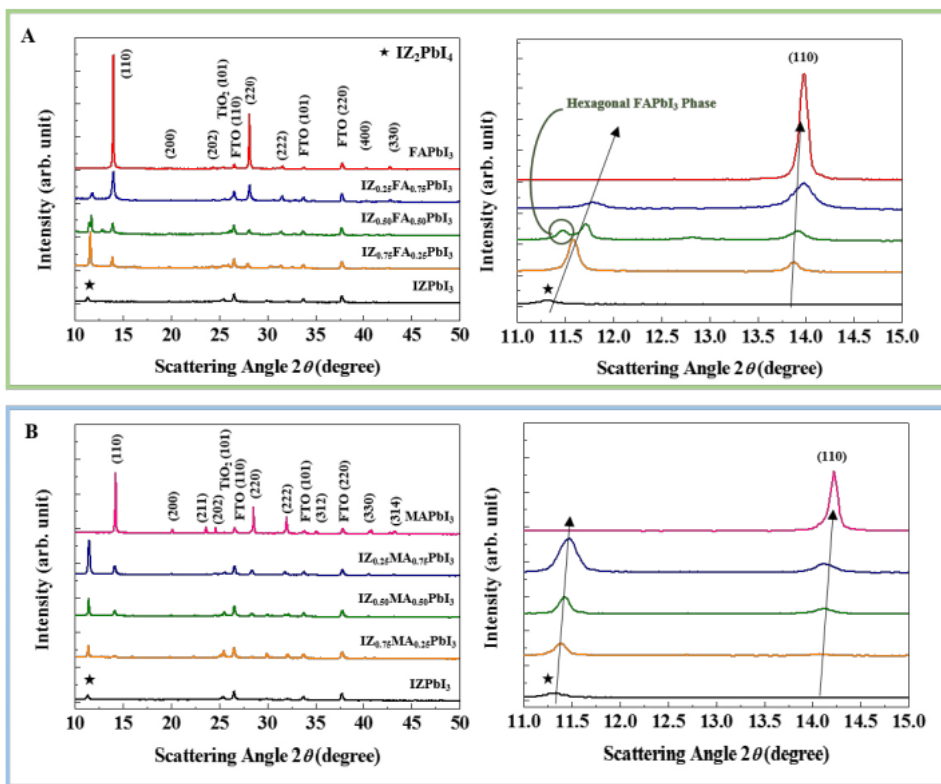
Fig. 4-5. Identification of perovskite alloying with large IZ contents (0%, 25%, 50%, 75%, and 100%): (a) 150°C-annealed FAPbI$_3$, and (b) 100°C-annealed MAPbI$_3$.
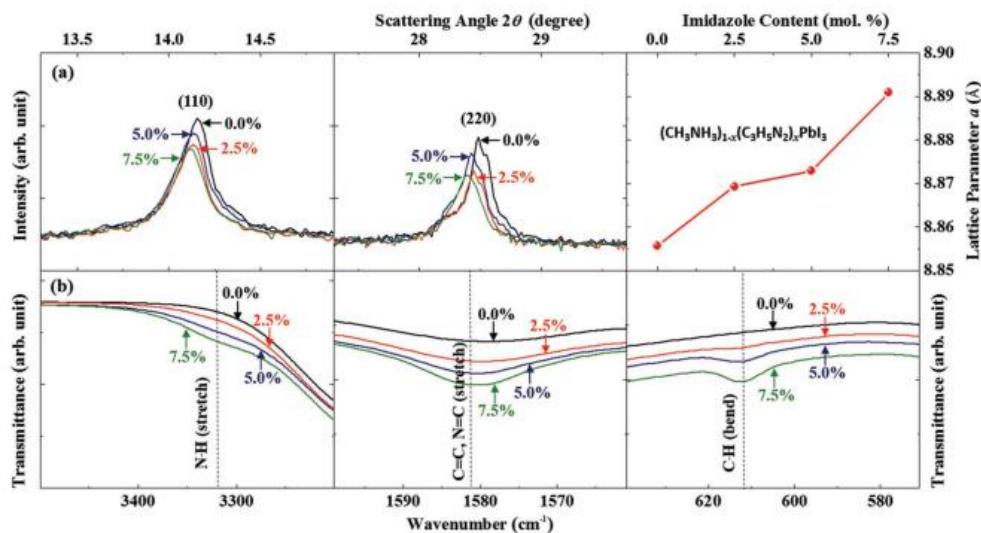
Fig. 4-6.   Characterization of imidazole-alloyed perovskite films with varying alloying contents of 0.0%, 2.5%, 5.0%, and 7.5%.   (a) Peak shifts in X-ray diffraction scans and effect on the lattice parameter ($a = b$ in tetragonal phase).   (b) Relative transmittance of imidazole-alloyed MAPbI$_3$ through FTIR.
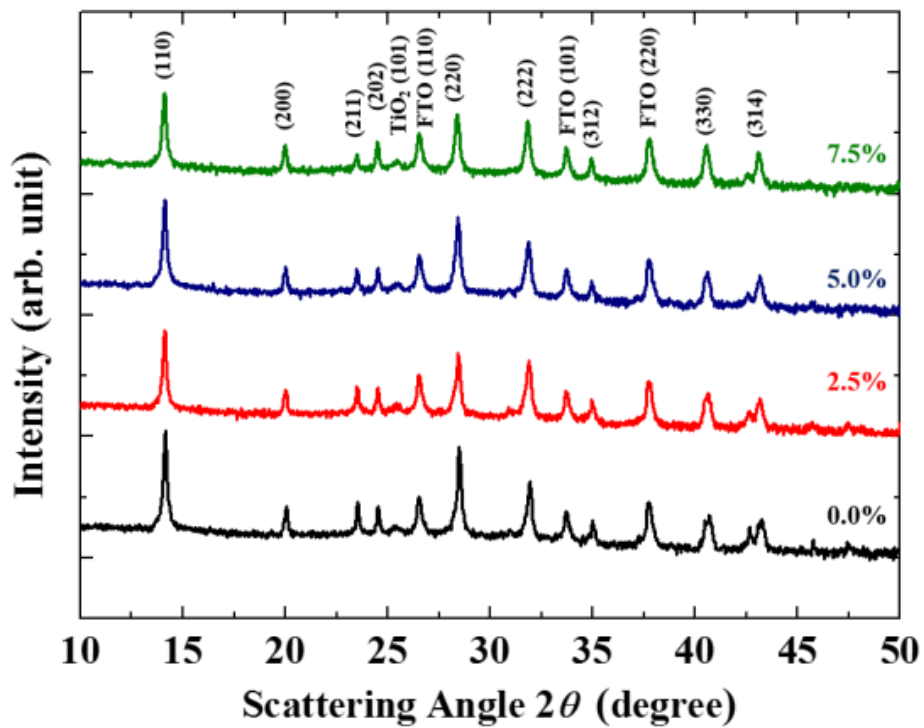
Fig. 4-7. X-ray-diffraction characterization of IZ-alloyed perovskite (0.0%, 2.5%, 5.0%, and 7.5%) in MAPbI₃.
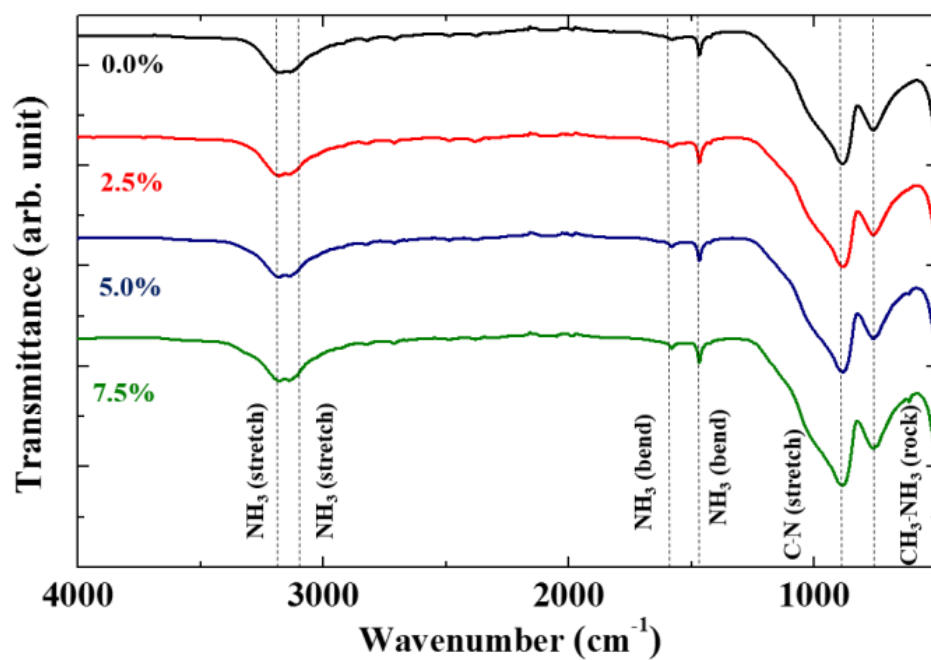
Fig. 4-8.   Transmittance of imidazole-alloyed MAPbI$_3$ using FTIR (with major peaks

of MAPbI$_3$ labeled).
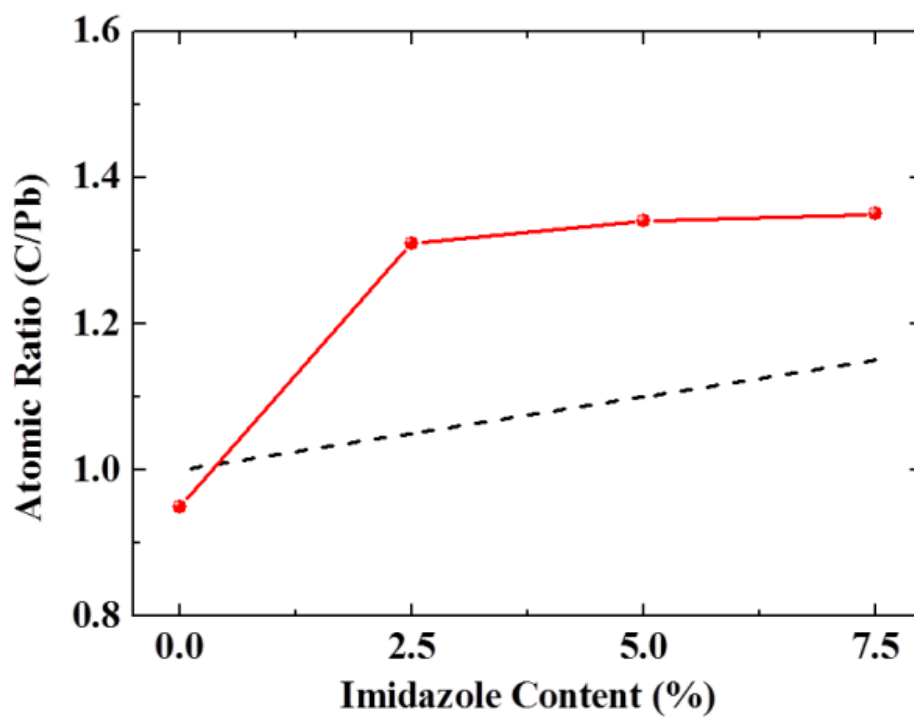
Fig. 4-9. Atomic ratio of carbon and lead by EDS at different IZ contents in
MAPbI$_3$, compared to the ideal concentration (dashed line).

After IZ is successfully alloyed in MAPbI$_3$, optical properties and grain sizes are analyzed in Fig. 4-10(a) and (b).   While all the alloyed perovskites exhibit similar band gap, the highest absorption coefficient is obtained with the 2.5%-IZ alloying, which is correlated with the grain size (with scanning electron microscope (SEM) images illustrated in Fig. 4-11).   We believe that IZ has not only increased the unit cell volume, but also possibly formed a 2D/3D hybrid structure, resulting in smaller grain sizes when the IZ content is higher than 2.5% [43(a,b)].   The aromatic structure of IZ is more electrically conductive than linear ones [43], leading to the enhanced electrical conductivity by the incorporation of IZ, as shown in Fig. 4-11(c) (also in Fig. 4-12), which guarantees sufficient charge transport and device operation. Furthermore, ultraviolet photoelectron spectroscopy (UPS) was conducted to understand the electronic structures of IZ-alloyed MAPbI$_3$ (Fig. 4-11(d)).   The work function decreases with the addition of IZ, which can provide a positive effect resulting in the increased open-circuit voltage (V_{oc}).

Devices with different contents of IZ alloying in MAPbI$_3$ are analyzed to demonstrate the effect of IZ on the solar cell performance by using a TiO$_2$-based mesoscopic device structure.   The J–V curve with 2.5% IZ exhibits the highest PCE of 17.6 ± 0.3% by more than ten cells (Fig. 4-13(a)) (with the minimized J–V hysteresis from the 2.5%-IZ-soluted device in Fig. 4-14).   Even though samples with 5.0% and 7.5% of IZ have also revealed promising improvements (with η = 17.0% and 14.7%, respectively), the enhanced electrical and optical properties have allowed the highest PCE with 2.5% IZ. (Median PCE values are presented above,

and reproducibility of devices are illustrated in Fig. 4-15 (scan rate = 10 mV s^{-1}). The EQE results in Figure 4b again confirm the highest efficiency from improved carrier transport, and the integrated currents of all devices get close to their short-circuit current values.

Device stability under degrading conditions is another critical issue for practical perovskite solar cells. Air stability was tested for 30 days ($\approx$ 55% relative humidity, without encapsulation) under dark (Fig. 4-13(c)), and as confirmed in Fig. 4-6 (proper alloying) and Fig. 4-8 (bonding nature), nonvolatile and strongly-bonded IZ molecules protect the devices under the open O_2 and H_2O degradation conditions [12–14]. Interestingly, Fig. 4-16 illustrates the diffraction of IZ-soluted perovskite films after 30 days, and it shows traces of IZ_2PbI_4 when 5.0% or 7.5% of IZ is soluted in MAPbI$_3$. It is very exciting that small amounts of IZ_2PbI_4 do not significantly reduce the device stability. The voltage- and light-induced degradation is also tested for 1000 s (Fig. 4-13(d), measured in air without encapsulation), due to the halide migration and electron/hole-transport layers [1, 15, 16]. Devices with 2.5%, 5.0%, 7.5% of IZ-alloyed MAPbI$_3$ exhibit $\approx$ 80%, $\approx$ 85%, and $\approx$ 90% of the initial current, where the unalloyed device has only sustained $\approx$ 60%, again confirming the stability of IZ alloying in MAPbI$_3$. Moreover, thermal stability of perovskite solar cells is measured at 100°C for 6 h (Fig. 4-13(e) and 4-17), heated in air without encapsulation). It should be noted that normal operating temperature of solar cells is $\approx$ 70°C [46]. However, devices heating in air could be damaged by several factors, such as heated H_2O and O_2. Therefore, experiment is designed to an extreme

condition (100°C) to maximize the heat-induced environment within short time in air. In order to confirm the nonvolatile nature of IZ (boiling temperature of ≈ 240°C) and strong bonding of IZ within the PbI_6^{4-} framework, bare and IZ alloyed perovskite powder are further analyzed with thermogravimetric analysis (TGA). Figure 4-18 confirms that IZ-alloyed perovskite retains the robust perovskite nanostructures from the heat. While the absence of IZ in $MAPbI_3$ is one major reason in the PCE reduction, Fig. 4-19 additionally confirms that there are visible deformations in hole-transport material (HTM) and Au.

For higher performance and stability, architectural modification of the device with SnO_2 (instead of TiO_2 as the electron transport layer for higher electron mobility) [15,16,47] is adapted, exhibiting an improved reverse PCE of 20.2% with a forward PCE of 19.0% in a planar structure, as shown in Figure 4f. Also, this device exhibits high stability over 120 s under steady-state current conditions. Moreover, a large area device [48] (cell area: 2 cm^2) is tested with 2.5% IZ, exhibiting a PCE of 16.8%, and the device stability is confirmed over 120 s under steady-state current conditions in Fig. 4-20. We believe that the aromatic molecule comprised of a multiamine-based cation can be one leading strategy for highly stable- and efficient perovskite solar cells.
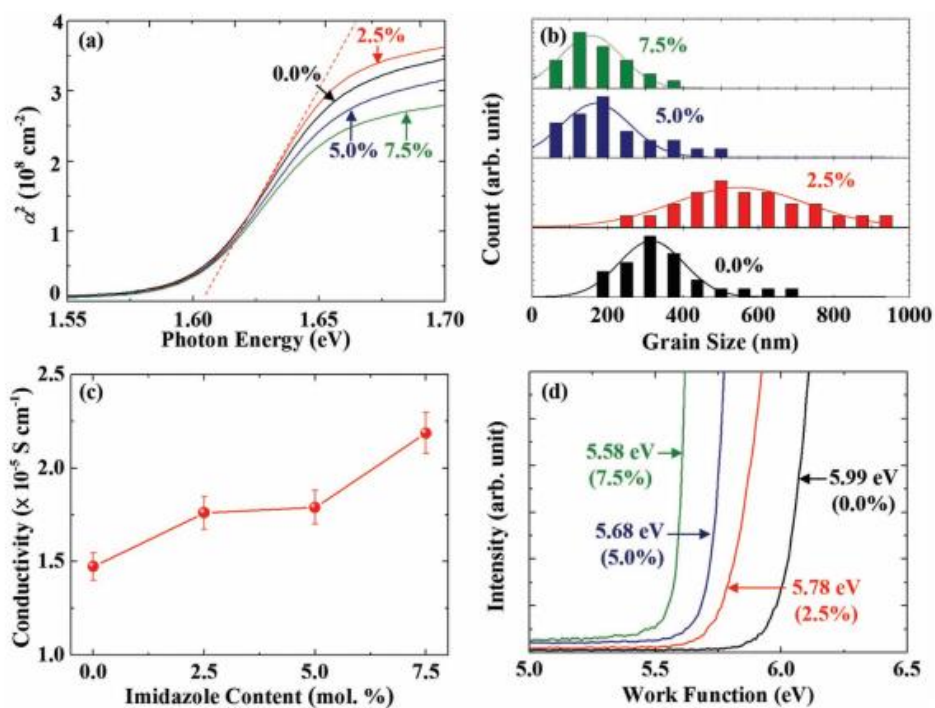
Fig. 4-10. Optical and electronic characteristics of imidazole-alloyed MAPbI$_3$ films. (a) Band gap change, (b) grain-size distributions, (c) electrical conductivity, and d) work function.
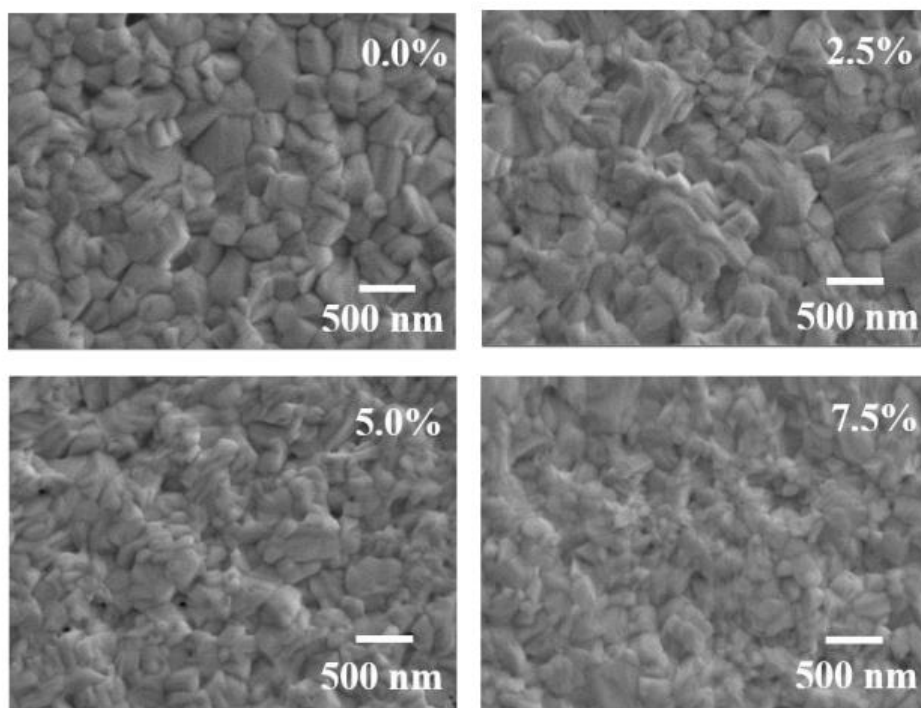
Fig. 4-11.   SEM images of different IZ contents in MAPbI$_3$.
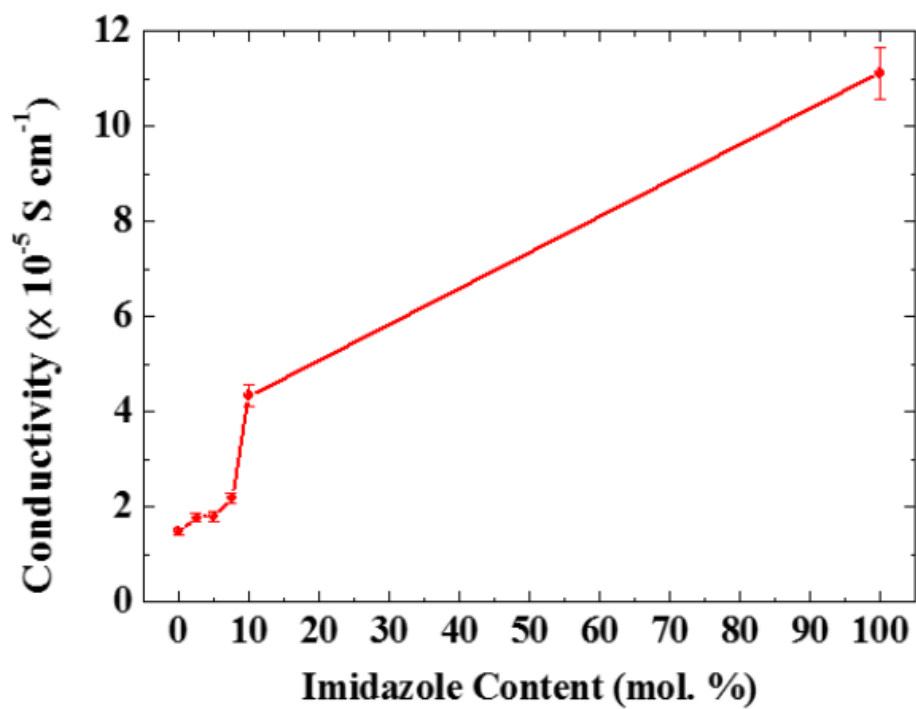
Fig. 4-12.　Electrical conductivity of films with various IZ contents in MAPbI$_3$
(with 100% indicating IZ$_2$PbI$_4$).
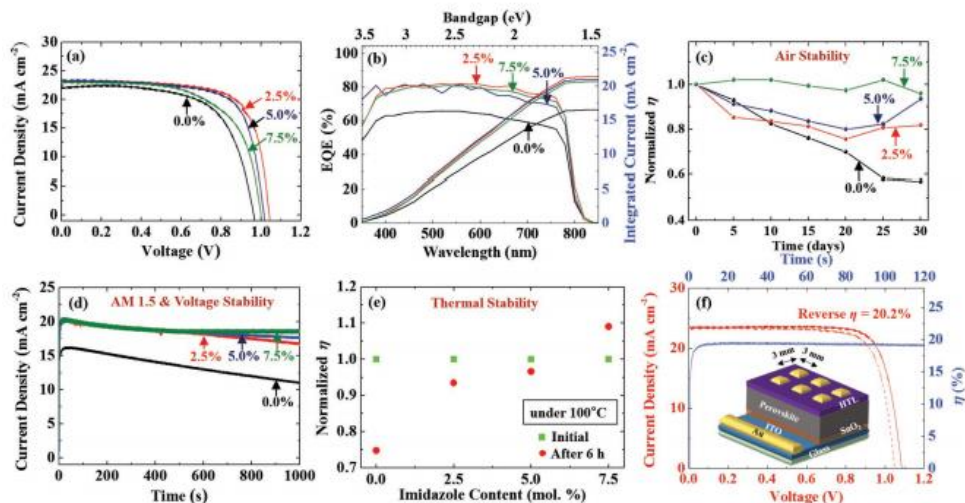
Fig. 4-13. Device performance and stability Test. (a) *J–V* curves (scan rate of 10 mV s^{-1}) and b) EQE spectra of imidazole-alloyed MAPbI$_3$. (c) Degradation of devices up to 30 days when cells are stored in air ($\approx 55\%$ humidity and dark). (d) Steady-state current for a 1000 s time scale to confirm the light- and voltage-induced degradation of the solar cells. (e) Heat-induced degradation of devices under 100°C for 6 h. (f) *J–V* curve of the champion device in this study (with 2.5% imidazole, and forward and reverse *J–V* shown as dotted and solid lines, respectively) and its steady-state current (at 0.90 V) using a SnO$_2$/ITO substrate.
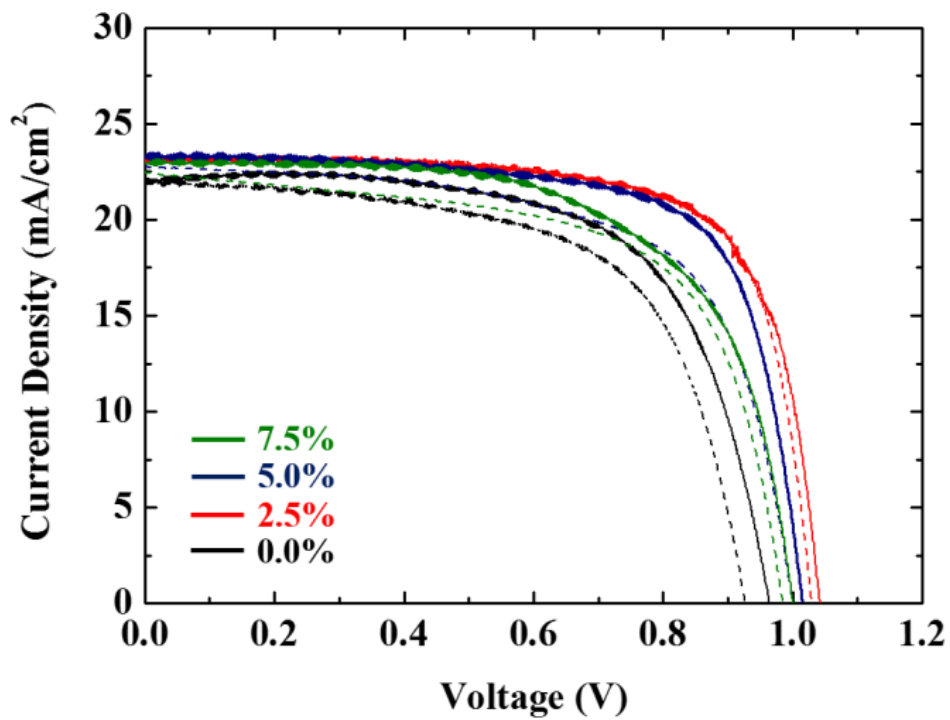
Fig. 4-14.   *J-V* curves for various contents of imidazole-alloyed MAPbI₃ (dotted and solid lines for forward and reverse scans, respectively) on TiO₂/FTO substrates.
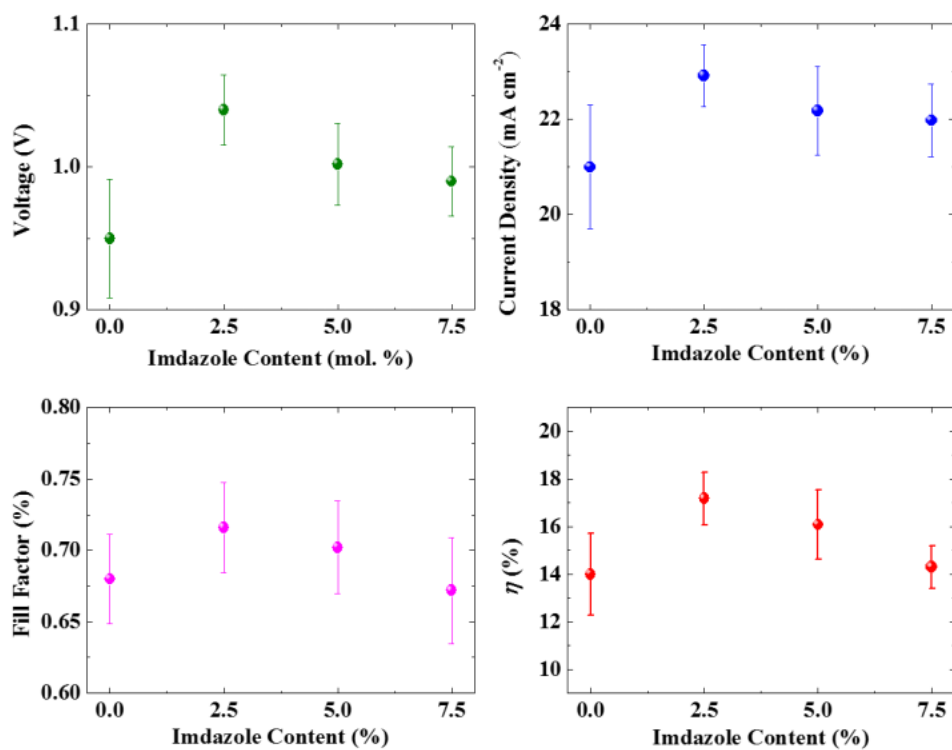
Fig. 4-15. Reproducibility of perovskite solar cells for various contents of imidazole-alloyed MAPbI$_3$ on TiO$_2$/FTO substrates.
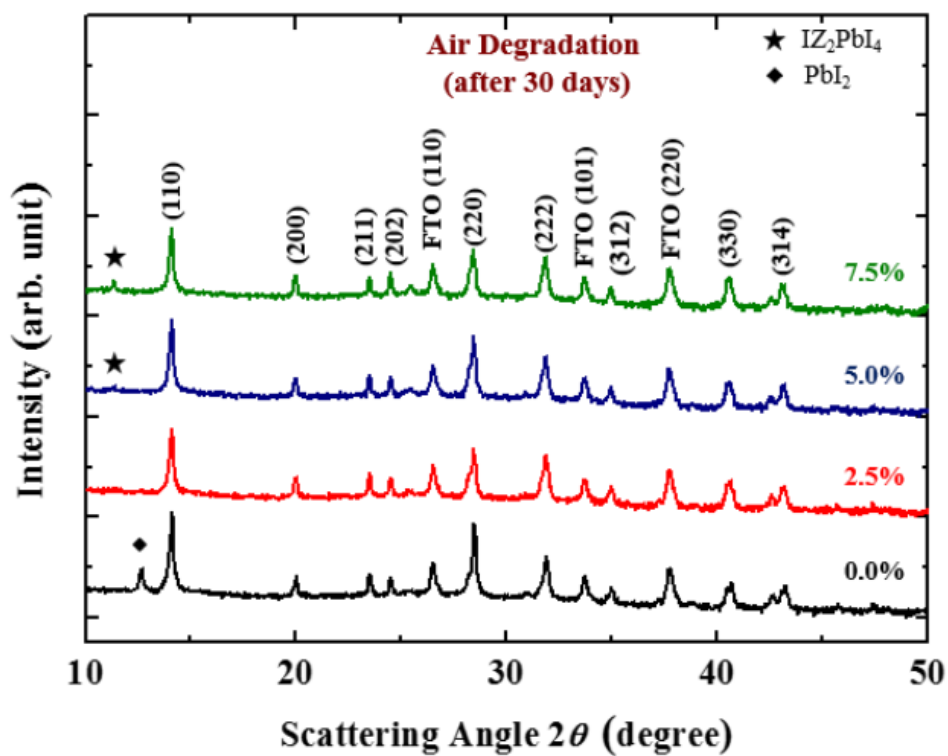
Fig. 4-16.   X-ray-diffraction characterization of perovskite films after 30 days in air.
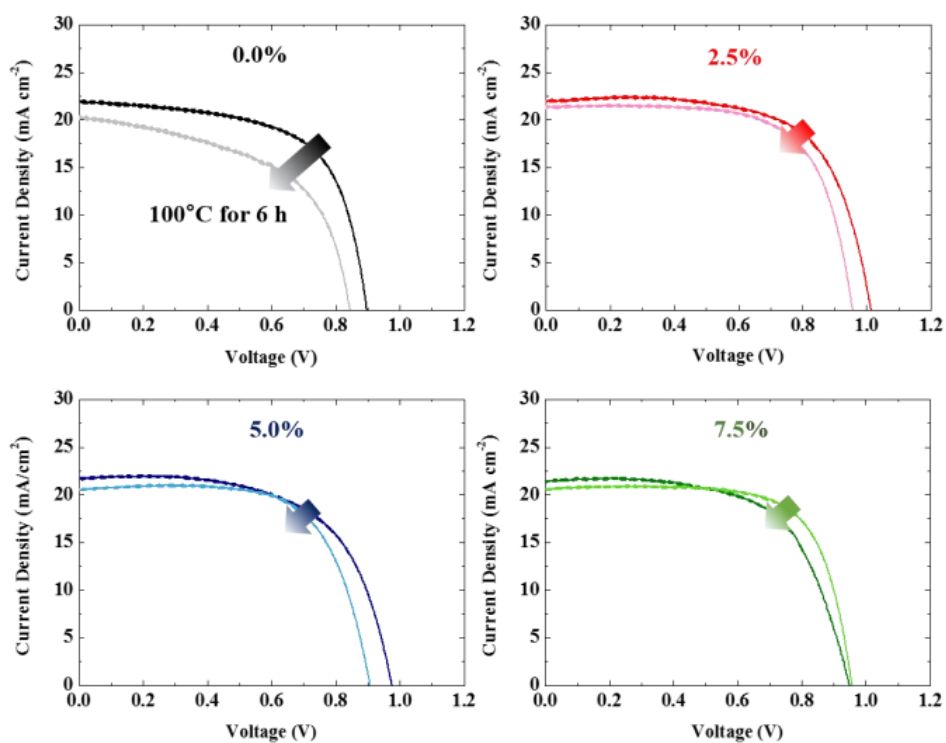
Fig. 4-17.   *J-V* curves of fresh vs. aged (100°C for 6 h) devices.
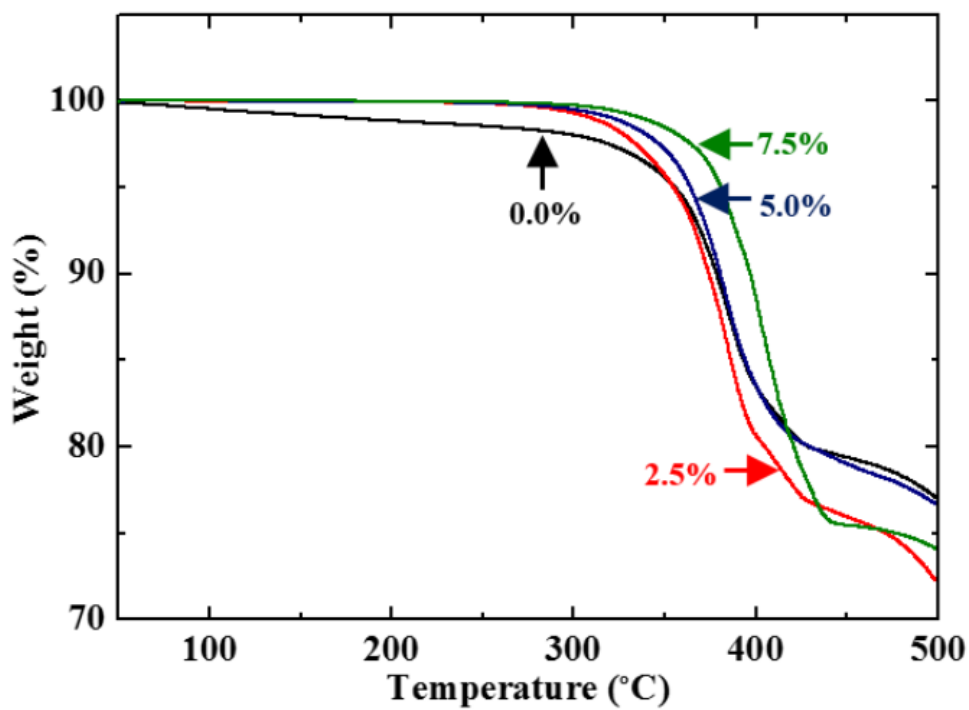
Fig. 4-18.　Thermogravimetric analysis (TGA) for characterization of the thermal

stability of perovskite powders.
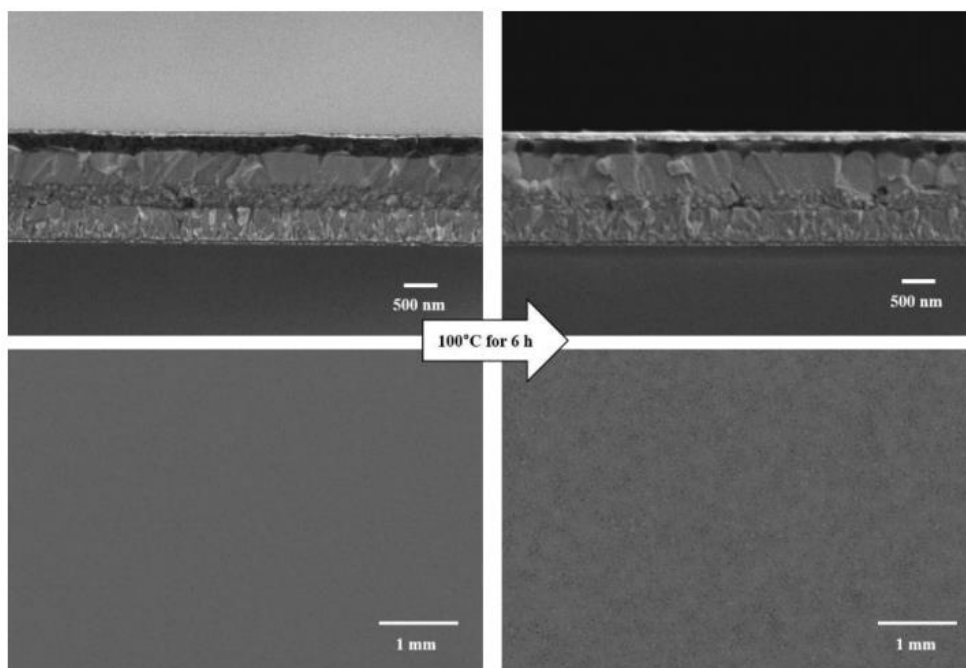
Fig. 4-19.   Cross-sectional and plan-view SEM images for fresh and thermal-
induced devices (100°C for 6 h).
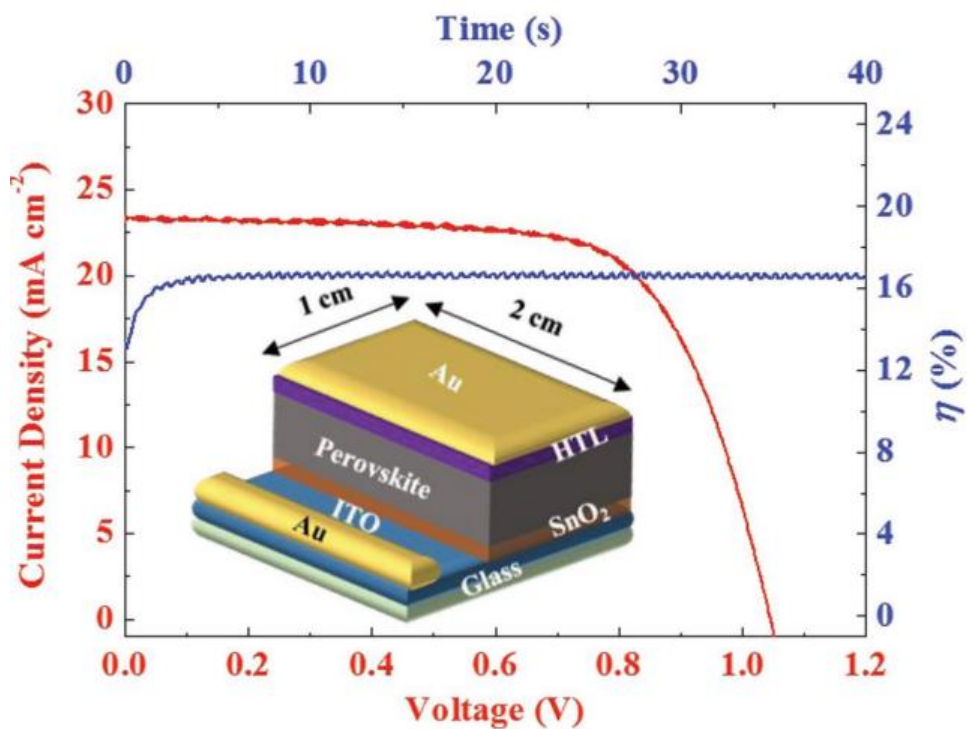
Fig. 4-20.   *J–V* curve and steady-state current results with a large active area of 2

cm^2 (2.5% imidazole) by using a SnO$_2$/ITO substrate.

4.4. Conclusions

Although perovskite solar cells have gathered enormous attention as next generation photovoltaics, stability issues should be resolved for future commercialization to become possible.   Here, we straightforwardly introduced IZ as an attractive cation solute to obtain both high PCE and stability of the devices. Due to the unique properties, such as the aromatic and diamine network of IZ, it exhibited superior stability with improved electronic structures, allowing phase stabilization, and high electrical/optical properties.   Also, devices with a large active area of 2 cm^2 exhibited PCEs as high as 16.8%.   This facile diamine-based cation-alloying technique integrated into the well-known MAPbI$_3$ perovskite surely improved several critical requirements that the device requires to be practical for future potential photovoltaics.

4.4. References

1. T. Hwang, B. Lee, J. Kim, S. Lee, B. Gil, A. J. Yun, and B. Park, "From Nanostructural Evolution to Dynamic Interplay of Constituents: Perspectives for Perovskite Solar Cells," *Adv. Mater.* **30**, 1704208 (2018).

2. S. R. Pae, S. Byun, J. Kim, M. Kim, I. Gereige, and B. Shin, "Improving Uniformity and Reproducibility of Hybrid Perovskite Solar Cells via a Low-Temperature Vacuum Deposition Process for NiO_x Hole Transport Layers," *ACS Appl. Mater. Interfaces* **10**, 534 (2018).

3. H. H. Park, R. Heasley, L. Sun, V. Steinmann, R. Jaramillo, K. Hartman, R. Chakraborty, P. Sinsermsuksakul, D. Chua, T. Buonassisi, and R. G. Gordon, "Co-Optimization of SnS Absorber and Zn(O,S) Buffer Materials for Improved Solar Cells," *Prog. Photovoltaics* **23**, 901 (2015).

4. Y. I. Lee, N. J. Jeon, B. J. Kim, H. Shim, T.-Y. Yang, S. I. Seok, J. Seo, and S. G. Im, "A Low-Temperature Thin-Film Encapsulation for Enhanced Stability of a Highly Efficient Perovskite Solar Cell," *Adv. Energy Mater.* **8**, 1701928 (2017).

5. J. Kim, T. Hwang, S. Lee, B. Lee, J. Kim, J. Kim, B. Gil, and B. Park, "Synergetic Effect of Double-Step Blocking Layer for the Perovskite Solar Cell," *J. Appl. Phys.* **122**, 145106 (2017).

6. J. Grandidier, D. M. Callahan, J. N. Munday, and H. A. Atwater, "Light Absorption Enhancement in Thin-Film Solar Cells Using Whispering Gallery Modes in Dielectric Nanospheres," *Adv. Mater.* **23**, 1272 (2011).

7. W.-C. Chen, C.-Y. Chen, V. Tunuguntla, S. H. Lu, C. Su, C.-H. Lee, K.-H. Chen,

and L.-C. Chen, "Enhanced Solar Cell Performance of $Cu_2ZnSn(S,Se)_4$ Thin Films through Structural Control by using Multi-Metallic Stacked Nanolayers and Fast Ramping Process for Sulfo-Selenization," *Nano Energy* **30**, 762 (2016).

8. J. Chen, J. Xu, S. Zhang, S. Zhou, K. Zhou, B. Zhang, X. Xia, Y. Liu, S. Dai, and J. Yao, "Halogen versus Pseudo-Halogen Induced Perovskite for Planar Heterojunction Solar Cells: Some New Physical Insights," *J. Phys. Chem. C* **121**, 28443 (2017).

9. T. Todorov, T. Gershon, O. Gunawan, Y. S. Lee, C. Sturdevant, L.-Y. Chang, and S. Guha, "Monolithic Perovskite-CIGS Tandem Solar Cells via In Situ Band Gap Engineering," *Adv. Energy Mater.* **5**, 1500799 (2015).

10. V. Steinmann, R. Jaramillo, K. Hartman, R. Chakraborty, R. E. Brandt, J. R. Poindexter, Y. S. Lee, L. Sun, A. Polizzotti, H. H. Park, R. G. Gordon, and T. Buonassisi, "3.88% Efficient Tin Sulfide Solar Cells using Congruent Thermal Evaporation," *Adv. Mater.* **26**, 7488 (2014).

11. C. Zuo, H. J. Bolink, H. Han, J. Huang, D. Cahen, and L. Ding, "Advances in Perovskite Solar Cells," *Adv. Sci.* **3**, 1500324 (2016).

12. C. Clegg, and I. G. Hill, "Systematic Study on the Impact of Water on the Performance and Stability of Perovskite Solar Cells," *RSC Adv.* **6**, 52448 (2016).

13. J. Yang, B. D. Siempelkamp, D. Liu, and T. L. Kelly, "Investigation of $CH_3NH_3PbI_3$ Degradation Rates and Mechanisms in Controlled Humidity Environments Using in Situ Techniques," *ACS Nano* **9**, 1955 (2015).

14. P. Bhatt, M. Kumar, C. Kant, M. K. Pandey, and B. Tripathi, "Optoelectronic

Modelling of Perovskite Solar Cells under Humid Conditions and their Correlation with Power Losses to Quantify Material Degradation," *Org. Electron*. **39**, 258 (2016).

15. B. Li, Y. Li, C. Zheng, D. Gao, and W. Huang, "Advancements in the Stability of Perovskite Solar Cells: Degradation Mechanisms and Improvement Approaches," *RSC Adv*. **6**, 38079 (2016).

16. T. Leijtens, G. E. Eperon, S. Pathak, A. Abate, M. M. Lee, and H. J. Snaith, "Overcoming Ultraviolet Light Instability of Sensitized TiO_2 with Meso-Superstructured Organometal Tri-Halide Perovskite Solar Cells," *Nat. Commun*. **4**, 2885 (2013).

17. G. Divitini, S. Cacovich, F. Matteocci, L. Cinà, A. D. Carlo, and C. Ducati, "In Situ Observation of Heat-Induced Degradation of Perovskite Solar Cells," *Nat. Energy* **1**, 15012 (2016).

18. N.-K. Kim, Y. H. Min, S. Noh, E. Cho, G. Jeong, M. Joo, S.-W. Ahn, J. S. Lee, S. Kim, K. Ihm, H. Ahn, Y. Kang, H.-S. Lee, and D. Kim, "Investigation of Thermally Induced Degradation in $CH_3NH_3PbI_3$ Perovskite Solar Cells using In-situ Synchrotron Radiation Analysis," *Sci. Rep*. **7**, 4645 (2017).

19. W. Peng, X. Miao, V. Adinolfi, E. Alarousu, O. E. Tall, A.-H. Emwas, C. Zhao, G. Walters, J. Liu, O. Ouellette, J. Pan, B. Murali, E. H. Sargent, O. F. Mohammed, and O. M. Bak, "Engineering of $CH_3NH_3PbI_3$ Perovskite Crystals by Alloying Large Organic Cations for Enhanced Thermal Stability and Transport Properties," *Angew. Chem., Int. Ed.* **55**, 10686 (2016).

20. T. Leijtens, G. E. Eperon, N. K. Noel, S. N. Habisreutinger, A. Petrozza, and H. J. Snaith, "Stability of Metal Halide Perovskite Solar Cells," *Adv. Energy Mater.* **5**, 1500963 (2015).

21. J. H. Noh, S. H. Im, J. H. Heo, T. N. Mandal, and S. I. Seok, "Chemical Management for Colorful, Efficient, and Stable Inorganic–Organic Hybrid Nanostructured Solar Cells," *Nano Lett*. **13**, 1764 (2013).

22. T. Hwang, D. Cho, J. Kim, J. Kim, S. Lee, B. Lee, K. H. Kim, S. Hong, C. Kim, and B. Park, "Investigation of Chlorine-Mediated Microstructural Evolution of $CH_3NH_3PbI_3(Cl)$ Grains for High Optoelectronic Responses," *Nano Energy* **25**, 91 (2016).

23. F. K. Aldibaja, L. Badia, E. Mas-Marza, R. S. Sanchez, E. M. Barea, and I. Mora-Sero, "Effect of Different Lead Precursors on Perovskite Solar Cell Performance and Stability," *J. Mater. Chem. A* 3, 9194 (2015).

24. D. V. Shinde, L. Pyeon, M. Pei, G.-W. Kim, H. Yang, and T. Park, "Enhanced Efficiency and Stability of an Aqueous Lead-Nitrate-Based Organometallic Perovskite Solar Cell," *ACS Appl. Mater. Interfaces* **9**, 14023 (2017).

25. J. Kim, T. Hwang, S. Lee, B. Lee, J. Kim, G. S. Jang, S. Nam, and B. Park, "Solvent and Intermediate Phase as Boosters for the Perovskite Transformation and Solar Cell Performance," *Sci. Rep*. **6**, 25648 (2016).

26. B.-W. Park, B. Philippe, X. Zhang, H. Rensmo, G. Boschloo, and E. M. J. Johansson, "Bismuth Based Hybrid Perovskites $A_3Bi_2I_9$ (A: Methylammonium or Cesium) for Solar Cell Application," *Adv. Mater*. **27**, 6806 (2015).

27. J.-C. Hebig, I. Kühn, J. Flohre, and T. Kirchartz, "Optoelectronic Properties of $(CH_3NH_3)_3Sb_2I_9$ Thin Films for Photovoltaic Applications," *ACS Energy Lett*. **1**, 309 (2016).

28. T. Leijtens, R. Prasanna, A. Gold-Parker, M. F. Toney, and M. D. McGehee, "Mechanism of Tin Oxidation and Stabilization by Lead Substitution in Tin Halide Perovskites," *ACS Energy Lett.* 2, 2159 (2017).

29. X. Qiu, Y. Jiang, H. Zhang, Z. Qiu, S. Yuan, P. Wang, and B. Cao, "Lead-Free Mesoscopic Cs_2SnI_6 Perovskite Solar Cells using Different Nanostructured ZnO Nanorods as Electron Transport Layers," *Phys. Status Solidi RRL* **10**, 587 (2016).

30. A. D. Jodlowski, C. Roldán-Carmona, G. Grancini, M. Salado, M. Ralaiarisoa, S. Ahmad, N. Koch, L. Camacho, G. d. Miguel, and M. K. Nazeeruddin, Large Guanidinium Cation Mixed with Methylammonium in Lead Iodide Perovskites for 19% Efficient Solar Cells, *Nat. Energy* 2, 972 (2017).

31. J. Lu, L. Jiang, W. Li, F. Li, N. K. Pai, A. D. Scully, C.-M. Tsai, U. Bach, A. N. Simonov, Y.-B. Cheng, and L. Spiccia, "Diammonium and Monoammonium Mixed-Organic-Cation Perovskites for High Performance Solar Cells with Improved Stability," *Adv. Energy Mater.* **7**, 1700444 (2017).

32. T. Zhang, M. I. Dar, G. Li, F. Xu, N. Guo, M. Grätzel, and Y. Zhao, "Bication Lead Iodide 2D Perovskite Component to Stabilize Inorganic $α$-$CsPbI_3$ Perovskite Phase for High-Efficiency Solar Cells," *Sci. Adv*. **3**, e1700841 (2017).

33. I. C. Smith, E. T. Hoke, D. Solis-Ibarra, M. D. McGehee, and H. I. Karunadasa, "A Layered Hybrid Perovskite Solar-Cell Absorber with Enhanced Moisture

Stability," *Angew. Chem.* **126**, 11414 (2014).

34. W Jiang, J. Ying, W. Zhou, K. Shen, X. Liu, X. Gao, F. Guo, Y. Gao, and T. Yang, "A New Layered Nano Hybrid Perovskite Film with Enhanced Resistance to Moisture-Induced Degradation," *Chem. Phys. Lett.* **658**, 71 (2016).

35. J.-H. Im, J. Chung, S.-J. Kim, and N.-G. Park, "Synthesis, Structure, and Photovoltaic Property of a Nanocrystalline 2H Perovskite-Type Novel Sensitizer $(CH_3CH_2NH_3)PbI_3$," *Nanoscale Res. Lett.* **7**, 353 (2012).

36. C. Huo, B. Cai, Z. Yuan, B. Ma, and H. Zeng, "Two-Dimensional Metal Halide Perovskites: Theory, Synthesis, and Optoelectronics," *Small Methods* **1**, 1600018 (2017).

37. Q. Wang, F. Lin, C.-C. Chueh, T. Zhao, M. Eslamian, and A. K.-Y. Jen, "Enhancing Efficiency of Perovskite Solar Cells by Reducing Defects through Imidazolium Cation Incorporation," *Mater. Today Energy* **7**, 161 (2018).

38. M. Becker, T. Klüner, and M. Wark, "Formation of Hybrid ABX_3 Perovskite Compounds for Solar Cell Application: First-Principles Calculations of Effective Ionic Radii and Determination of Tolerance Factors," *Dalton Trans.* **46**, 3500 (2017).

39. G. Kieslich, S. Sun, and A. K. Cheetham, "Solid-state principles applied to organic–inorganic perovskites: new tricks for an old dog," *Chem. Sci.* 5, 4712 (2014).

40. M. T. Weller, O. J. Weber, J. M. Frost, and A. Walsh, "Cubic Perovskite Structure of Black Formamidinium Lead Iodide, α-[$HC(NH_2)_2$]PbI_3, at 298 K," *J. Phys.*

Chem. Lett. **6**, 3209 (2015).

41. Z. Li, M. Yang, J.-S. Park, S.-H. Wei, J. J. Berry, and K. Zhu, "Stabilizing Perovskite Structures by Tuning Tolerance Factor: Formation of Formamidinium and Cesium Lead Iodide Solid-State Alloys," *Chem. Mater.* **28**, 284 (2016).

42. W.-G. Li, H.-S. Rao, B.-X. Chen, X.-D. Wanga, and D.-B. Kuang, "A Formamidinium–Methylammonium Lead Iodide Perovskite Single Crystal Exhibiting Exceptional Optoelectronic Properties and Long-Term Stability," *J. Mater. Chem. A* **5**, 19431 (2017).

43. a) M. Abdi-Jalebi, M. I. Dar, A. Sadhanala, S. P. Senanayak, M Franckevicius, N. Arora, Y. Hu, M. K. Nazeeruddin, S. M. Zakeeruddin, M Grätzel, and R. H. Friend, "Impact of Monovalent Cation Halide Additives on the Structural and Optoelectronic Properties of $CH_3NH_3PbI_3$ Perovskite," *Adv. Energy Mater.* **6**, 1502472 (2016); b) J. Fan, Y. Ma, C. Zhang, C. Liu, W. Li, R. E. I. Schropp, and Y. Mai, "Thermodynamically Self-Healing 1D–3D Hybrid Perovskite Solar Cells," *Adv. Energy Mater.* **8**, 1703421 (2018).

44. A. Mahendran, P. Gopinath, and R. Breslow, "Single Molecule Conductance of Aromatic, Nonaromatic, and Partially Antiaromatic Systems," *Tetrahedron Lett.* **56**, 4833 (2015).

45. J. V. Passarelli, D. J. Fairfield, N. A. Sather, M. P. Hendricks, and H. Sai, "Enhanced Out-of-Plane Conductivity and Photovoltaic Performance in $n = 1$ Layered Perovskites through Organic Cation Design," *J. Am. Chem. Soc.* **140**, 7313 (2018).

46. A. D. Sheikh, R. Munir, M. A. Haque, A. Bera, W. Hu, P. Shaikh, A. Amassian, and T. Wu, "Effects of High Temperature and Thermal Cycling on the Performance of Perovskite Solar Cells: Acceleration of Charge Recombination and Deterioration of Charge Extraction," *ACS Appl. Mater. Interfaces* **9**, 35018 (2017).

47. Q. Jiang, L. Zhang, H. Wang, X. Yang, J. Meng, H. Liu, Z. Yin, J. Wu, X. Zhang, and J. You, "Enhanced Electron Extraction using SnO_2 for High-Efficiency Planar-Structure $HC(NH_2)_2PbI_3$-based Perovskite Solar Cells," *Nat. Energy* **2**, 16177 (2017).

48. H. Chen, F. Ye, W. Tang, J. He, M. Yin, Y. Wang, F. Xie, E. Bi, X. Yang, M. Grätzel, and L. Han, "A Solvent- and Vacuum-Free Route to Large-Area Perovskite Films for Efficient Solar Modules," *Nature* **550**, 92 (2017).

Chapter 5.

Origins of Efficient Perovskite Solar Cells with Low-Temperature Processed SnO$_2$ Electron Transport Layer

5.1. Introduction

Organometal halide perovskite (OHP) is regarded as one of the most promising candidate for next-generation photovoltaic materials in the aspects of both cost and efficiency. Intense research on the applications of OHP to solar cell has achieved remarkable progress, increasing the power conversion efficiency (PCE) up to ～23% in just several years, as a result of accomplishments in the compositional engineering and morphology/crystallization control of OHP [1-3]. Recent studies have improved both the photovoltaic property and stability of perovskite solar cells by modifying and optimizing the perovskite films [2-8]. However, limitations still remain within the conventional electron/hole transport layers (ETL/HTL) and interfaces, and so does demand for further advances [9].

The perovskite solar cell (PSC) with current world-record efficiency adopts mesoscopic TiO$_2$ as an electron-transport layer. Though mesoscopic structure of TiO$_2$ can boost electron extraction from the perovskite layer to anode, it has a drawback requiring high-temperature process around 500°C that hinders the commercialization of PSC [10-13]. On the other hand, planar PSC requires simple and economic fabrication processes compared to the mesoscopic PSC, and thus has

attracted huge attention [14-16]. For planar PSC, SnO_2 film has been recently noticed to be one of the most promising ETL with high charge mobility and low photoactivity [17-22].

Several researches have observed the effect of SnO_2 annealing temperature on the solar cell performance [23-25]. For example, Fang et al. fabricated SnO_2-based ETL by spin-coating $SnCl_2$ precursor solution at several temperatures (185-500°C), and Docampo et al. used ALD-processed SnO_x ETL (room temperature (RT) to 300°C) appointing the Fermi-level change to be an origin of the device properties [23,24]. Nevertheless, the exact correlation between the SnO_2-film characteristics and solar-cell performance are not yet fully understood, especially with nanoparticle-based SnO_2 ETL.

In this work, dependence of the device performance on the SnO_2 annealing temperature is observed with *n-i-p* planar PSCs using nanoparticle-based SnO_2 layer as an ETL. In order to understand the annealing effects on the SnO_2 properties and declare the factors contributing to the photovoltaic performance, nanoscopic morphology and optical/electronic properties of SnO_2 films are scrutinized with various annealing temperatures (RT to 200°C). In addition, because the solar cell performance is strongly correlated to various factors including the properties of perovskite, electron/hole transporting materials, and interfaces [9,26-34], the deep-trap states and band alignment are also discussed. With explication on how SnO_2 annealing temperature affects the film property and sequentially the solar cell performance, insights to realize efficient perovskite solar cell with low-temperature process are provided, expanding the perspective of its commercial applications.

5.2. Experimental Section

SnO₂ Film Deposition.   ITO substrate (Wooyang GMS) was etched by zinc powder (TCI Chemicals) and cleansed under sonication in acetone, ethanol, and deionized water.   The substrate was used after 15 min of UV-ozone treatment.   In order to prevent agglomeration of nanoparticles, 15 wt% SnO_2 nanoparticle dispersion in H_2O (Alfa-Aesar) was stirred and sonicated before dilution. Then the suspension was diluted to 3.4 wt %, filtered by PTFE membrane (CHMLAB), and spin-coated on the ITO substrate at 3000 rpm for 30 s.   Subsequently, SnO_2 layer was annealed at various temperature (RT, 80°C, 120°C, 160°C, and 200°C) for 30 min on a hot plate, and UV-ozone treated for 15 min afterward.

Solar Cell Fabrication.   For the $Cs_{0.05}(FA_{0.83}MA_{0.17})_{0.95}Pb(I_{0.83}Br_{0.17})_3$ perovskite (CsFAMA) film, 1.3 M $(FA_{0.83}MA_{0.17})Pb(I_{0.83}Br_{0.17})_3$ perovskite precursor solution was prepared by dissolving formamidinium iodide (FAI; Great Solar Laboratory), methylammonium bromide (MABr; Great Solar Laboratory), lead iodide (PbI₂; TCI Chemicals), and lead bromide (PbBr₂; TCI Chemicals) in a mixture of N,N-dimethylformamide (DMF; Sigma-Aldrich) and dimethyl sulfoxide (DMSO; Sigma-Aldrich) with the volume ratio of 4:1. For Cs doping, 1.0 M CsI (TCI Chemicals) solution dissolved in the same solvent was added.   The perovskite solution was stirred for 2 h and then spin-coated on the as-prepared SnO_2 layer in two steps of spinning program: 1000 rpm for 10 s for the first step and 5000 rpm for 20 s for the second step.   Three hundred microliters of chlorobenzene (Sigma-Aldrich) was dropped 3 s before the second spin-step ended, and the substrate was annealed at

100°C for 30 min on a hot plate.   Hole transporting material was prepared by dissolving 72.3 mg of spiro-MeOTAD (Lumtec) in 1 mL of chlorobenzene (Sigma-Aldrich), and 28.8 μL of 4-tert-butylpyridine (Sigma-Aldrich) and 17.5 μL of bis(trifluoromethane)sulfonimide lithium salt (SigmaAldrich) in acetonitrile (520 mg/mL) were added as additives.   The HTM solution was spin-coated on the substrate, and finally Au electrode was thermally evaporated.

Characterization.   The surface topography of SnO_2 layer was observed by using atomic force microscopy (NX-10; Park Systems). Each measurement was conducted for the area of either 1×1 μm^2 or 10×10 μm^2.   Four-point probe was utilized to measure electric conductivity of SnO_2 films deposited on a glass substrate.   Work function and valence band maximum of each deposited SnO2 layer were measured via multipurpose X-ray photoelectron spectroscopy (Sigma Probe; Thermo VG Scientific) with argon sputtering.   Light with energy $hv = 21.22$ eV was used in the ultraviolet photoelectron spectroscopy (UPS) measurement.   Optical properties of SnO_2 films were measured with UV/vis spectroscopy (V-770; JASCO) with an integrating sphere. Incident photon to current efficiency (IPCE) measurements were performed by solar cell IPCE system (K3100; McScience). Photocurrent density-voltage (*J-V*) curves were achieved via solar cell measurement system (K-3000; McScience) for an active area of 0.09 cm^2.   During the measurement, the voltage was swept from the reverse to forward direction (from 1.2 to 0.1 V with a scan rate of 100 mV/s).   One sun light was illuminated using a solar simulator (xenon lamp, air mass 1.5 G).   For impedance analysis, a potentiostat (Zive SP-1; WonATech)

was adopted, and the impedance of photovoltaic device was measured with 10 mV AC perturbation in the frequency range from 10 mHz to 100 kHz under zero bias in dark condition.   Before this measurement, all the devices had been relaxed in the dark until voltage drops below 3 mV [35].   To observe film morphology of perovskite layers and cross-sectional image of devices, a field-emission scanning electron microscope (Merlin Compact; Zeiss) was used. Crystal structures were examined by an X-ray diffractometer (New D-8 Advance; Bruker).

5.3. Results and Discussion

To investigate the effect of SnO_2 annealing temperature on the solar cell performance, SnO_2 films are annealed at various temperatures with the resultant cell parameters including power-conversion efficiency (η), open-circuit voltage (V_{OC}), fill factor (*FF*), short-circuit current density (J_{SC}), and hysteresis index (*HI*) (Fig. 5-1). Though the optimum annealing temperature of nanoparticle-based SnO_2 ETL has been previously regarded to exceed 150°C [18,21], the most efficient solar cell is acquired at 120°C with the highest η of 19.0%. The η presents a trend of arch upward, and it is mainly attributed to the V_{OC} and *FF* that show similar dependences with peaks at the 120°C condition as well (Fig. 5-1(a-c)). Interestingly, the low-temperature processed SnO_2 annealed below 150°C or even at RT outperforms the high-temperature processed SnO_2 in the aspects of V_{OC}, *FF*, and consequently η. Furthermore, as shown in Fig. 5-1(d), the J_{SC} is measured to increase as SnO_2 annealing temperature decreases. This annealing effect on J_{SC} is consistent with the IPCE measurement in Fig. 5-2, of which the integrated J_{SC} also increases with the lower-temperature processed SnO_2. On the other hand, hysteresis is reduced for the SnO_2 ETLs annealed at lower temperatures (Fig. 5-1(e)). The *J-V* curve of a champion cell for each annealing condition is shown in Fig. 5-3(a,b) with the corresponding cell parameters referred in Table 5-1. The upper layers including perovskite layer, HTL, and metal electrode are fabricated by the same procedures. The differences in both crystallinity and microscopic morphology of perovskite upper layers are also negligible (Figs. 5-4 and 5-5), and thereby we assume that these

observed tendencies in Fig. 5-1 originate only from the features of SnO_2 ETL and its interface. Further analyses on the SnO_2 films and interfaces are conducted to understand the correlation between their properties and the solar cell performance, as well as to reveal the origins of outstanding performance by low-temperature processed SnO_2 ETL.
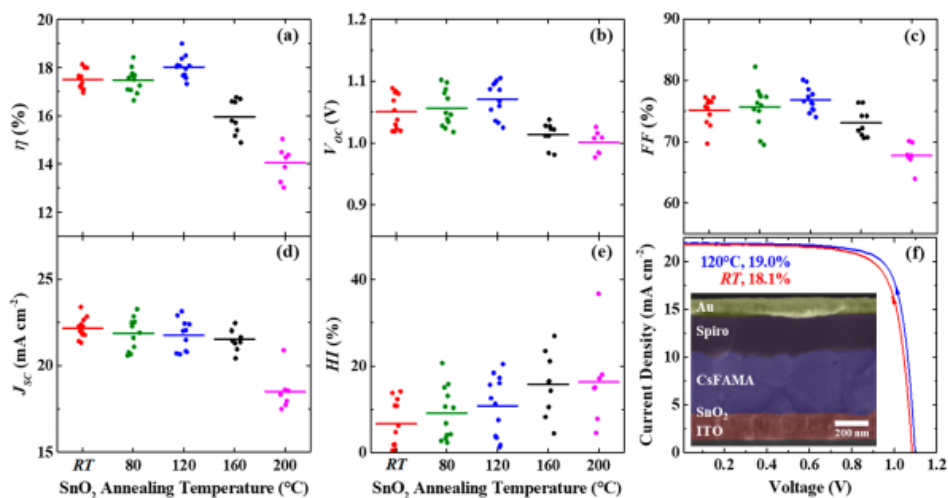
Fig. 5-1. Device performance versus SnO_2 annealing temperature. (a) η, (b) V_{OC}, (c) FF, (d) J_{SC}, and (e) $HI = (\eta_{rev} - \eta_{for})/\eta_{rev}$ of solar cells as a function of SnO_2 annealing temperature. Each data point demonstrates the representative device of one experimental batch. (f) J-V curves of champion cells at room temperature and 120°C with the cell geometry by SEM (CsFAMA = Cs-doped $(FA_{0.83}MA_{0.17})Pb(I_{0.83}Br_{0.17})_3$).
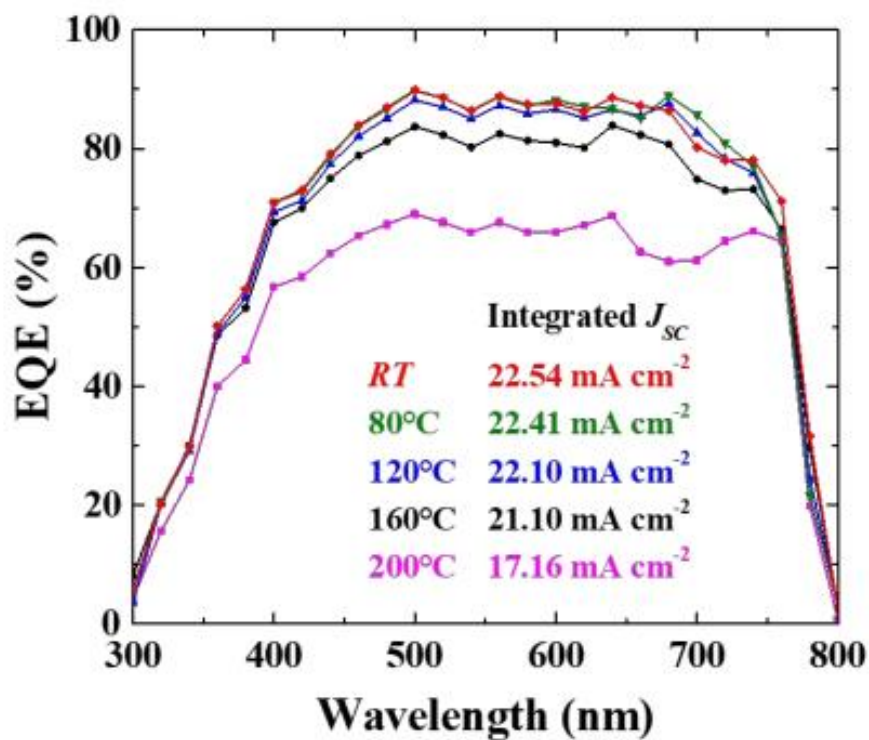
Fig. 5-2. IPCE spectra of the perovskite solar cells. The IPCE measurements of PSCs with various SnO_2 annealing temperatures. The integrated JSC are indicated.
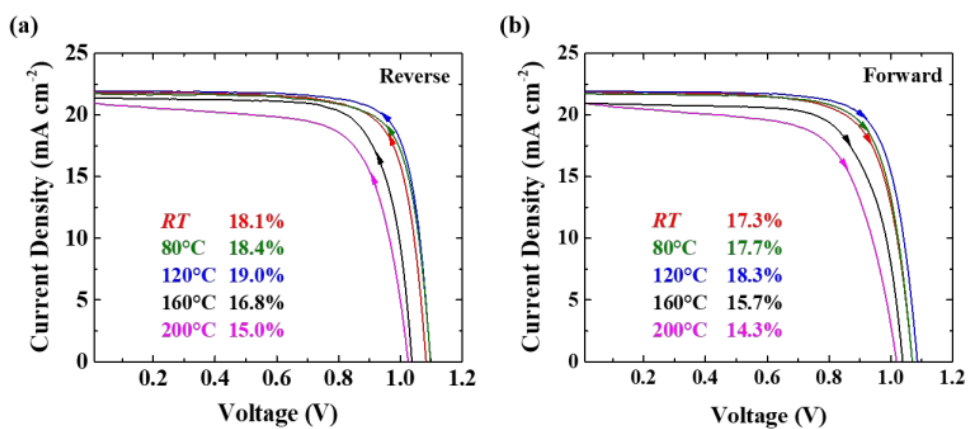
Fig. 5-3. *J-V* curve of the champion cell for each SnO$_2$ annealing temperature. Solar cells are examined by (a) reverse scan and (b) forward scan, respectively. The corresponding cell parameters are referred in Table 5-1.

Annealing Temperature	J_{SC} (mA cm^{-2})	V_{OC} (V)	FF (%)	η (%)
RT	21.8	1.084	76.7	18.1
80°C	21.6	1.098	77.6	18.4
120°C	22.0	1.098	78.5	19.0
160°C	21.2	1.038	76.2	16.8
200°C	20.9	1.026	70.1	15.0

Table 5-1. Device performance vs. SnO$_2$ annealing temperature. Short-circuit current (J_{SC}), open-circuit voltage (V_{OC}), fill factor (FF), and power-conversion efficiency (η) of the champion cells (reverse direction). Full J-V characteristics are shown in Fig. 5-3.
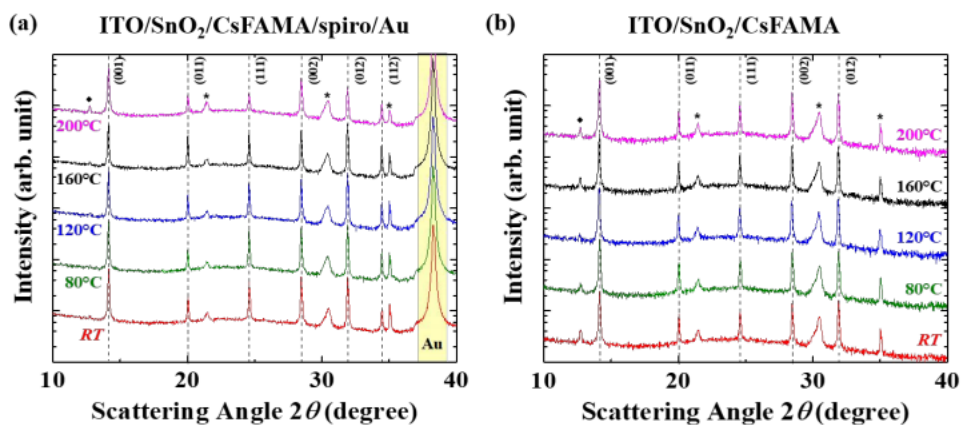
Fig. 5-4. X-ray diffraction patterns of perovskite solar cells, with and without HTL/Au. XRD patterns of (a) full devices and (b) perovskite films, fabricated on a SnO_2 layer annealed at various temperatures. Peaks are indexed assuming perovskite crystal in a cubic structure. The diamond and asterisk symbols represent the peak positions of PbI_2 and ITO, respectively.
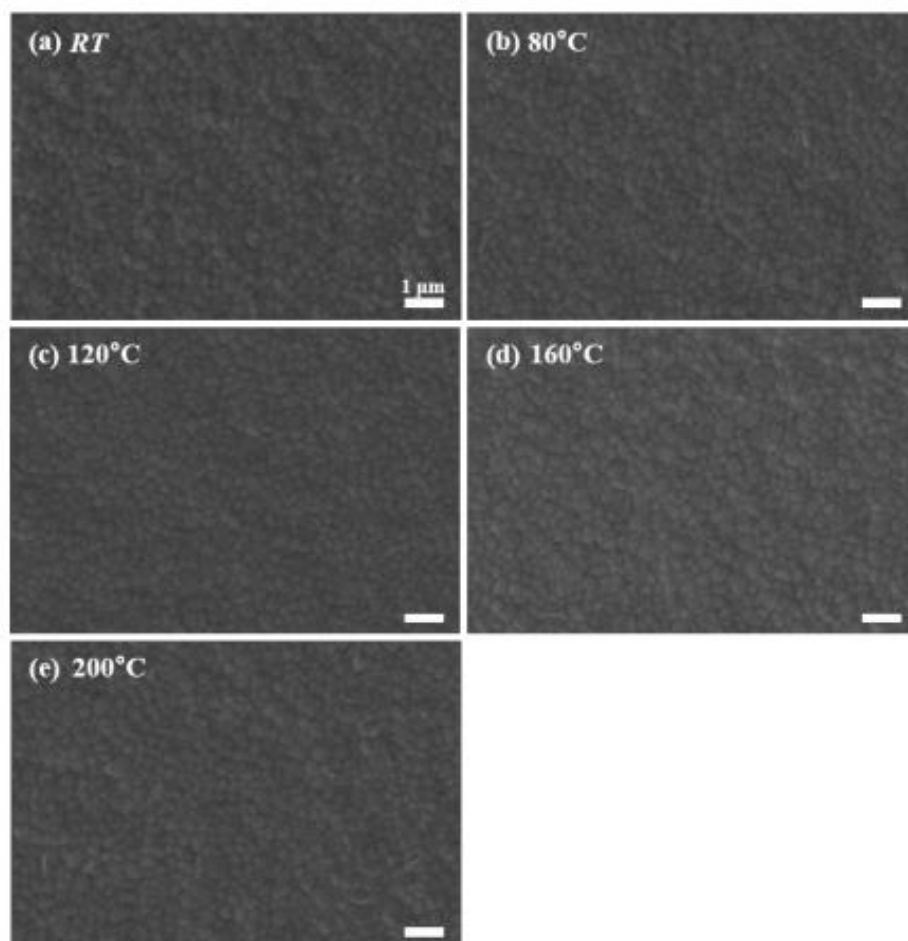
Fig. 5-4. SEM images of perovskite film surfaces. Surface morphology of perovskite film deposited on a SnO2 layer annealed at (a) RT, (b) 80°C, (c) 120°C, (d) 160°C, and (e) 200°C.

First, the surface morphology of SnO_2 film has been observed to understand how uniformity of the surface changes by the annealing condition and affects the solar cell performance. Considering the size of SnO_2 nanoparticles (3-5 nm) [18] and thickness of film ($\sim$20 nm in Fig. 5-6(a)), surface morphology has been observed in nanoscale using atomic force microscopy (AFM) rather than scanning electron microscopy (SEM) (Fig. 5-6(b)). Topographies of bare ITO and various SnO_2 films are shown in Fig. 5-7(a-f). In general, the deposited SnO_2 films demonstrate considerably smoother surface than bare ITO, confirming that SnO_2 nanoparticle layers are successfully formed regardless of the annealing temperature. In addition, the surface roughness is measured quantitatively in peak-to-valley average and root-mean-squared value (σ_{rms}), respectively (Fig. 5-7(g)), confirming that the SnO_2 nanoparticle layer shapes more uniformly and smoothly when annealed at lower temperature below 150°C. The σ_{rms} for SnO_2 annealed at 160 and 200°C are larger than 0.8 nm in average, while those of low-temperature processed SnO_2 are $\sim$20% smaller. Similarly, the peak-to-valley roughnesses soar at 160 and 200°C.

The morphology of SnO_2 nanoparticle layer depends on its annealing temperature, and the rate of solvent evaporation is presumed to be responsible. Regarding that the thickness of deposited SnO2 layer is observed to be $\sim$20 nm, the measured roughnesses of SnO_2 annealed at 160 and 200°C are of notable scale to deteriorate the contact with perovskite upper layer by forming shunting paths such as pinholes. It is well known that the charge collection efficiency and the shunt resistance of solar cells are deeply involved with nanoscopic morphology of ETL and the formation of shunting paths [20,22,36,37], and hence the uniformity of SnO_2

ETL is expected to influence both J_{SC} and *FF* of the perovskite solar cell. Accordingly, the rough surface of high-temperature processed SnO_2 is reproached for its reduced J_{SC} and *FF*. Though the electrical conductivity is greater for higher annealing temperature (Fig. 5-7(h)), it seems not critical for the charge transport within only ～20 nm thick ETL.

To further scrutinize the correlations between the annealing temperature of SnO_2 and cell parameters, work function and valence band maximum (VBM) of SnO_2 are evaluated from the secondary electron edge and valence band spectrum (Figs. 5-8(a,b), respectively). As SnO_2 annealing temperature increases, the work function of SnO_2 film first rises from 4.14 eV at RT to 4.39 eV at 120°C, and then drops to 4.19 eV at 200°C. The VBM with respect to the Fermi level (VBM = E_{offset} − E_F) is observed to increase as SnO_2 annealing temperature decreases. To compare the band diagrams, the optical bandgap of each SnO_2 film was measured (shown in Fig. 5-8(c)), exhibiting from 3.96 to 3.92 eV as the annealing temperature increases from RT to 200°C. The band diagrams of SnO_2 films depicted in Fig. 5-8(d) (based on the values of Table 5-2) indicates that the high-temperature processed SnO_2 has relatively high conduction band maximum (CBM) with the perovskite upper layer. With the driving force of electron extraction from the perovskite layer to ETL, the lowtemperature processed SnO_2 is likely to exhibit more preferred band alignment in short-circuit condition for efficient electron transport (Fig. 5-1(d)).

Observing the shifts of band levels, we suspect that the defect formation, especially at the ETL/perovskite interface, also depends on the SnO_2 annealing temperature. To explore the defects of SnO_2-based solar cells, the impedance

analysis is performed for capacitance as $C \equiv 1/i\omega Z$ (Fig. 5-9). The capacitive feature of perovskite solar cell at high frequency is determined by geometrical and depletion-layer capacitance of perovskite [38,39], whereas the low-frequency capacitance is claimed to originate from the charging/discharging of electronic traps at the interfaces [40-43]. In Fig. 5-9(a), the capacitances at high frequency over 100 Hz are almost indistinguishable, but on the other hand the low-frequency capacitances show clear differences depending on the SnO_2 annealing temperature. Considering that the fabrication procedures except for the SnO_2-annealing temperatures are identical for the examined devices, the differences in the low frequency capacitances reflects the contributions of only from the ETLs and/or ETL/perovskite interfaces, rather than other constituents such as perovskite layers and HTLs. This argument is also supported by the analyses including X-ray diffraction and SEM on the perovskite layers with negligible differences (Figs. 5-4 and 5-5).

Deep-level traps at the interfaces contribute to the device capacitance under low-frequency perturbation by being charged and discharged repeatedly [40,44,45]. From the capacitance-frequency plot, the trap-density state nt versus E_ω (= E − $E_{bandedge}$) can be calculated [45,46]. In Fig. 5-9(b), nt for different SnO_2 annealing temperatures are compared and the deep-trap distribution noticeably varies, indicating that the defect formation at the interface between the SnO_2 ETL and perovskite layer is influenced by the SnO_2-annealing temperature. From the Gaussian fitting of trap-density state, the trap density (N_t) and trap level (E_0) have been evaluated quantitatively (Fig. 5-9(c) and Table 5-3). As shown in Fig. 5-9(c),

N_t draws an arch downward with the lowest trap density at 120°C, of which the trend is opposite to that of the observed V_{OC}.

These results confirm that the interfacial deep-traps play a significant role determining the V_{OC} of the solar cell, and the schematics are in Fig. 5-9(d). When PSC is illuminated, the photogenerated electrons fill the electronic traps, and when an electron is trapped in a deep-level state, a nonradiative recombination process is likely to occur. The recombination is believed to be the main factor undermining V_{OC} of the solar cell, which is verified by these SnO_2 devices with low Nt exhibiting high V_{OC} and vice versa (Fig. 5-9(c)). Various defects in the perovskite solar cells are the main reasons causing *J-V* hysteresis or irreversible degradation in the device performance. Plausibly, the low-temperature processed SnO_2 devices demonstrate small hysteresis effects, and their reduced traps are thought to be one of the reasons. Yet, other factors including shallow-traps are also underlying, making tendency of hysteresis slightly different with that of the interfacial deep-traps (Figs. 5-1(e) and 5-9(c)). Meanwhile, as we have tested the thermal stability of the as-fabricated devices, these less-defective solar cells with SnO_2 annealed at 120°C sustain 90% of their initial PCEs after being kept in the 85°C/ 85% relative-humidity (RH) environment for over 300 h, as shown in Fig. 5-10. Deeper studies are to be performed on these stability results, including the roles of various traps at each layer and interfaces in the long term degradation mechanisms.
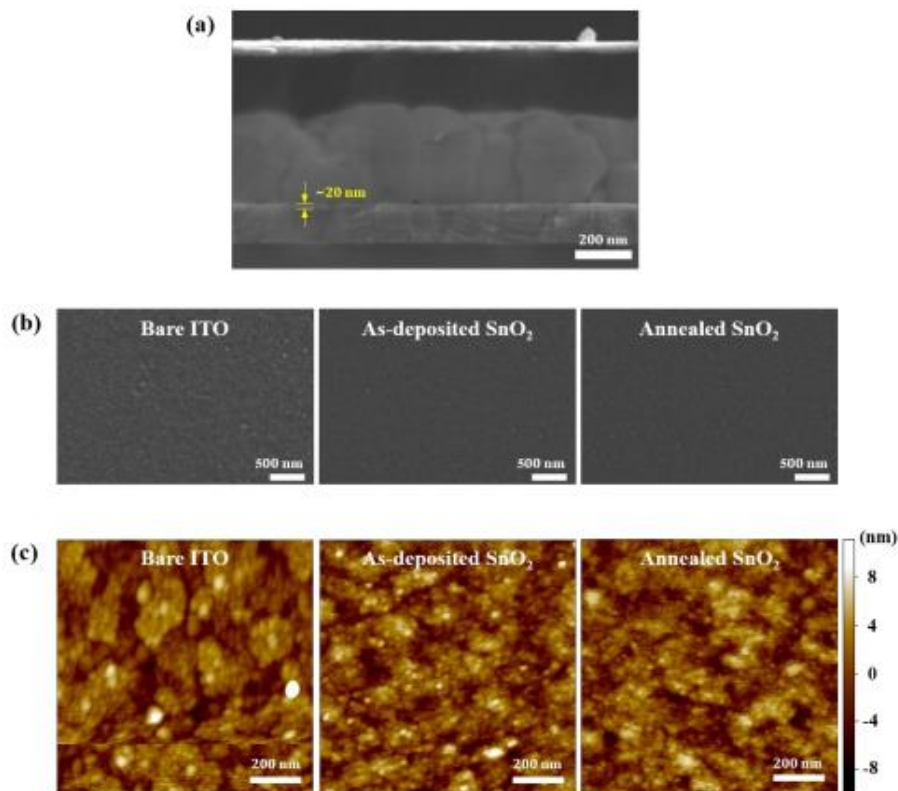
Fig. 5-6. Basic characterizations of SnO$_2$ thin films. (a) Cross-sectional SEM image of the device (ITO/SnO$_2$/CsFAMA/spiro/Au) with a thickness estimation of SnO$_2$ layer. (b) Planar SEM image and (c) AFM topography of bare ITO and ITO/SnO$_2$ surfaces. The AFM images are shown in the same color scale. For (b) and (c), SnO$_2$ films are characterized before and after annealing at 120°C.
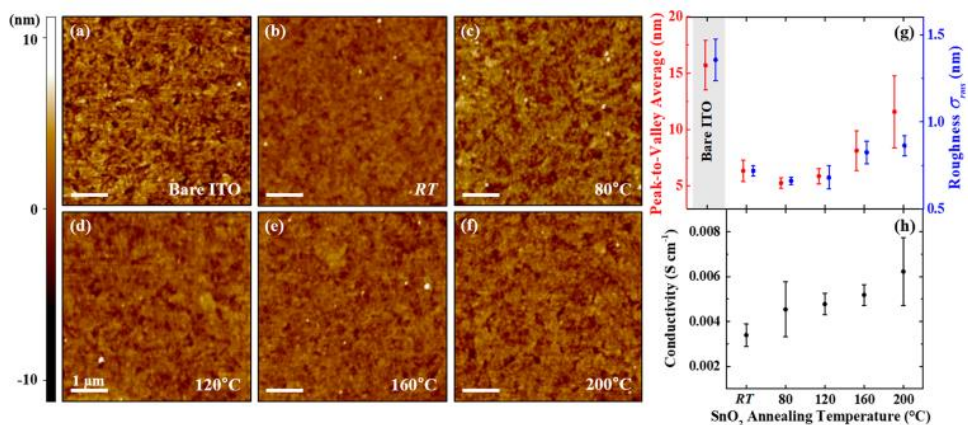
Fig. 5-7. Morphological features and electrical properties of SnO₂ films. Surface topography of (a) bare ITO substrate, and (b-f) SnO₂ layer annealed at different temperatures. The AFM images are shown in the same color scale. (g) Roughnesses by peak-to-valley and root-mean-squared values as a function of annealing temperature with bare ITO as a reference. (h) Electric conductivity of SnO₂ thin films.
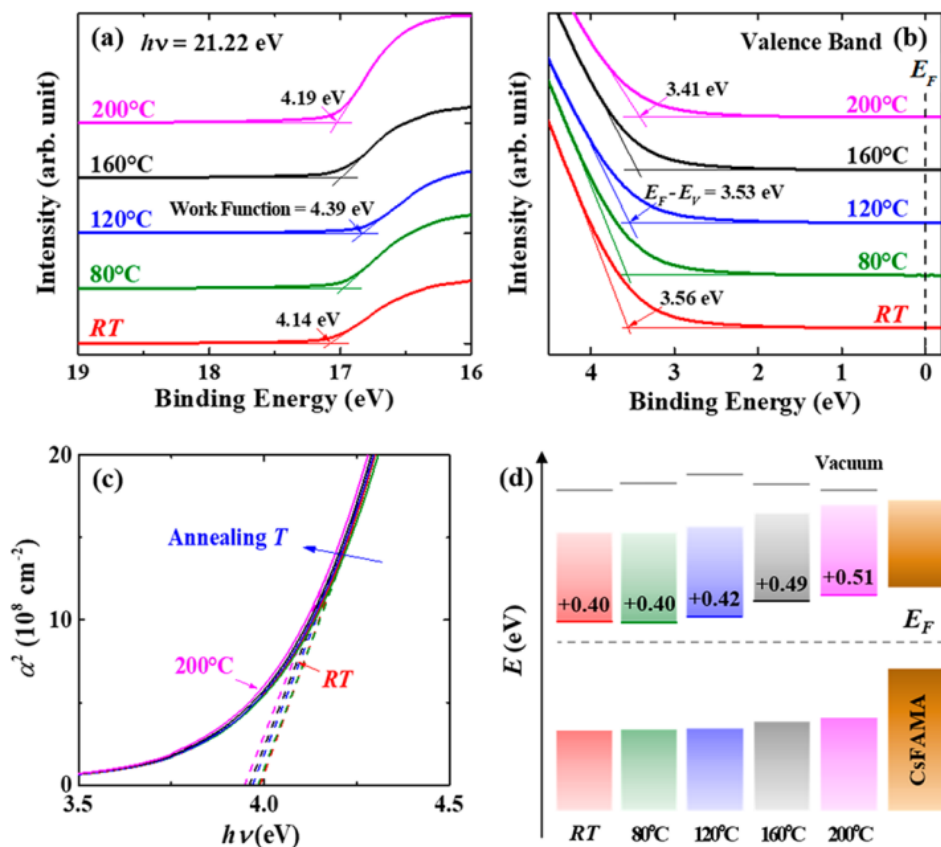
Fig. 5-8. Energy level diagram of SnO_2 electron-transport layer. (a) Secondary electron edge and (b) valence-band maximum of SnO_2 layer at each annealing temperature (as measured by UPS). (c) Tauc plot of SnO_2 films for the bandgap energy (E_g). The blue arrow indicates the shift of bandgap as the annealing temperature increases (Detailed fitting parameters for panels a-c are in Table 5-3). (d) Schematic band diagram of each SnO_2 layer with the perovskite as a reference.

Annealing Temperature	Work Function (eV)	VBM (eV)	E_g (eV)
RT	4.14	-3.56	3.96
80°C	4.25	-3.56	3.96
120°C	4.39	-3.53	3.95
160°C	4.23	-3.45	3.94
200°C	4.19	-3.41	3.92

Table 5-2.   Work function, valence band maximum, and bandgap of each SnO_2 layer.

Fermi level of SnO_2 film is calculated from E_F (= work function) = hv -

E_{cutoff} with hv = 21.22 eV.   Bandgap of SnO_2 has been estimated from

the Tauc plot in Fig. 5-8(c).
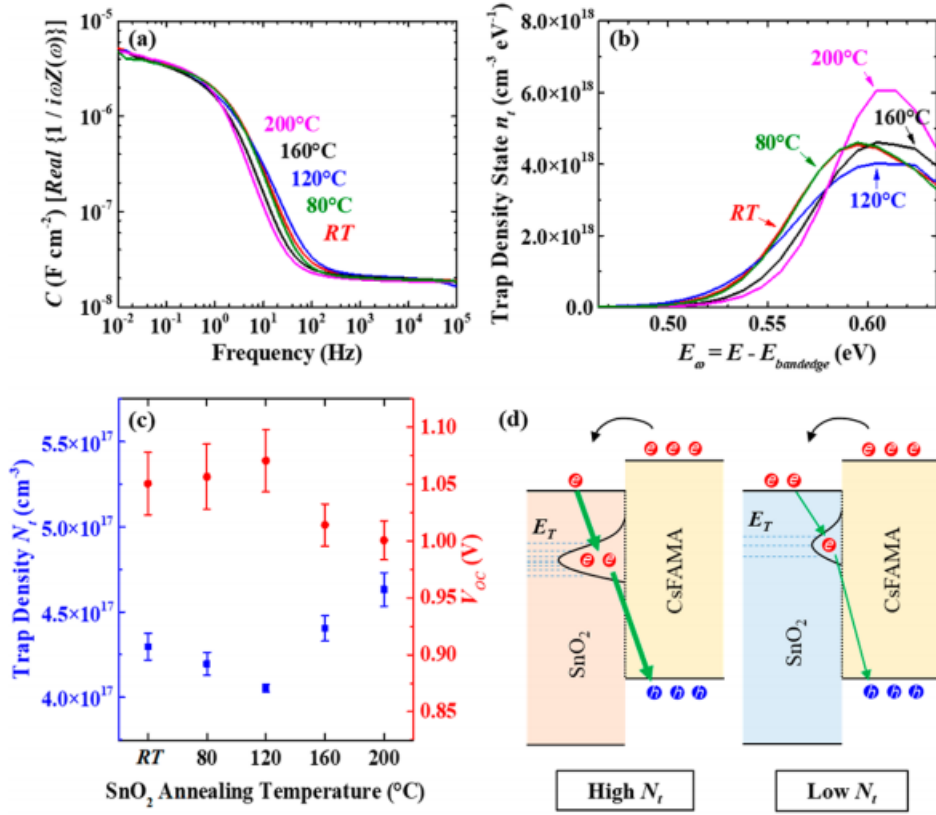
Fig. 5-9.   Effects of annealing temperature on the electronic trap states.   (a)
Capacitance-frequency plot and (b) trap distribution spectra of solar cells.
(c) Trap density per volume (N_t) and V_{OC} of each solar cell. N_t is obtained
by fitting the trap density state in (b) using a Gaussian function.   (d)
Schematics for the role of interfacial traps in recombination.

Annealing Temperature	Trap Density N_t (cm^{-3})	E_0 (eV)
RT	$4.30 \pm 0.08 \times 10^{17}$	0.602
80°C	$4.20 \pm 0.07 \times 10^{17}$	0.601
120°C	$4.05 \pm 0.02 \times 10^{17}$	0.605
160°C	$4.40 \pm 0.07 \times 10^{17}$	0.613
200°C	$4.63 \pm 0.10 \times 10^{17}$	0.615

Table 5-3.   Electronic trap density and defect energy level E_0 (Fig. 5-9).
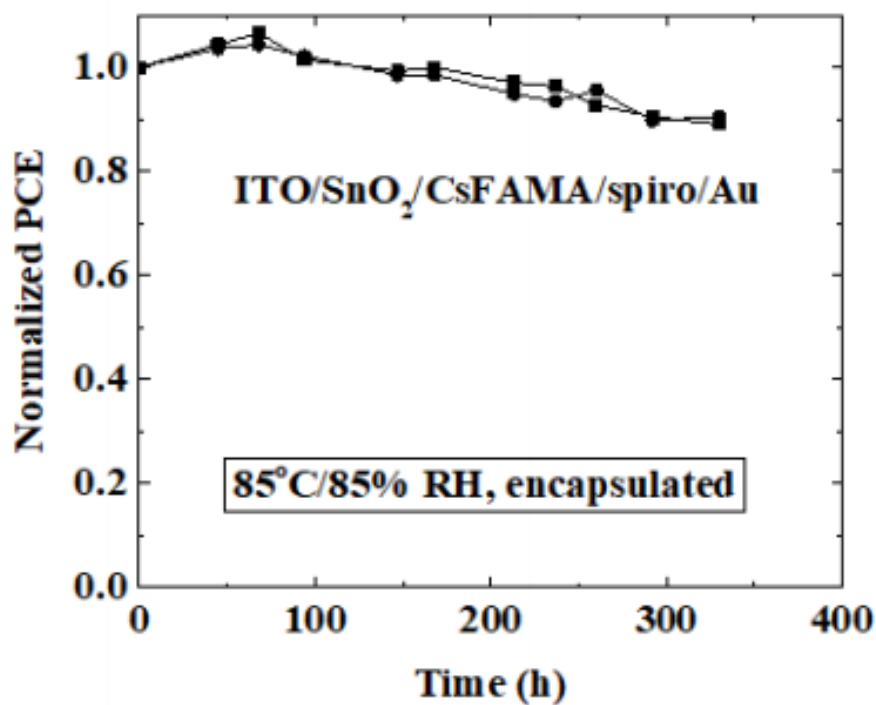
Fig. 5-10.   Thermal stability of perovskite solar cells.   Stability of encapsulated

perovskite solar cells with SnO_2 ETL annealed at 120°C, stored in 85°C

environment with 85% relative humidity (RH) in dark.   Two devices

are shown in a normalized PCE (reverse scan).

5.4. Conclusions

Uniform electron-transport layer using SnO_2 nanoparticles is systematically investigated. By varying the annealing temperature from RT to 200°C, the best efficiency of 19.0% has been obtained from annealing at 120°C. The morphological, optical, and electronic properties of SnO_2 layers are investigated, and the interfacial trap states between SnO_2 and perovskite layers are analyzed. Efficient perovskite solar cells with low-temperature processed SnO_2 ETL are realized by uniform/smooth SnO_2 surface, favorable band alignment, and reduced trap density plus shifting toward the bandedge. These less-defective solar cells can sustain 90% of their initial PCEs from the 85°C/85%-RH environment for over 300 h. Our straightforward work offers insights to realize more efficient and stable perovskite solar cells with lower cost, enlarging the potential of commercial applications.

5.5. References

1. A. Kojima, K. Teshima, J. Shirai, and T. Miyasaka, "Organometal Halide Perovskites as Visible-Light Sensitizers for Photovoltaic Cells," *J. Am. Chem. Soc*. **131**, 6050 (2009).

2. N. J. Jeon, J. H. Noh, W. S. Yang, Y. C. Kim, S. Ryu, J. Seo, and S. I. Seok, "Compositional Engineering of Perovskite Materials for High-Performance Solar Cells," *Nature* **517**, 476 (2015).

3. W. S. Yang, J. H. Noh, N. J. Jeon, Y. C. Kim, S. Ryu, J. Seo, and S. I. Seok, "High-Performance Photovoltaic Perovskite Layers Fabricated through Intramolecular Exchange," *Science* **348**, 1234 (2015).

4. H. P. Zhou, Q. Chen, G. Li, S. Luo, T. B. Song, H. S. Duan, Z. R. Hong, J. B. You, Y. S. Liu, and Y. Yang, "Interface Engineering of Highly Efficient Perovskite Solar Cells," *Science* **345**, 542 (2014).

5. J. Kim, T. Hwang, B. Lee, S. Lee, K. Park, H. H. Park, and B. Park, "An Aromatic Diamine Molecule as the *A*-Site Solute for Highly Durable and Efficient Perovskite Solar Cells," *Small Methods* **3**, 1800361 (2019).

6. S. Wieghold, J.-P. Correa-Baena, L. Nienhaus, S. Sun, K. E. Shulenberger, Z. Liu, J. S. Tresback, S. S. Shin, M. G. Bawendi, and T. Buonassisi, "Precursor Concentration Affects Grain Size, Crystal Orientation, and Local Performance in Mixed-Ion Lead Perovskite Solar Cells," *ACS Appl. Energy Mater*. **1**, 6801 (2018).

7. J. Berry, T. Buonassisi, D. A. Egger, G. Hodes, L. Kronik, Y.-L. Loo, I. Lubomirsky, S. R. Marder, Y. Mastai, J. S. Miller, D. B. Mitzi, Y. Paz, A. M.

Rappe, I. Riess, B. Rybtchinski, O. Stafsudd, V. Stevanovic, M. F. Toney, D. Zitoun, A. Kahn, D. Ginley, and D. Cahen, "Hybrid Organic-Inorganic Perovskites (HOIPs): Opportunities and Challenges," *Adv. Mater*. **27**, 5102 (2015).

8. D. Kim, G. Y. Kim, C. Ko, S. R. Pae, Y. S. Lee, O. Gunawan, D. F. Ogletree, W. Jo, and B. Shin, "Effects of Postsynthesis Thermal Conditions on Methylammonium Lead Halide Perovskite: Band Bending at Grain Boundaries and Its Impacts on Solar Cell Performance," *J. Phys. Chem. C* **120**, 21330 (2016).

9. S. Sun, T. Buonassisi, and J.-P. Correa-Baena, "State-of-the-Art Electron-Selective Contacts in Perovskite Solar Cells," *Adv. Mater. Interfaces* **5**, 1800408 (2018).

10. J. Burschka, N. Pellet, S.-J. Moon, R. Humphry-Baker, G. Peng, N. K. Nazeeruddin, and M. Gratzel, "Sequential Deposition as a Route¨ to High-Performance Perovskite-Sensitized Solar Cells," *Nature* **499**, 316 (2013).

11. T. Hwang, D. Cho, J. Kim, J. Kim, S. Lee, B. Lee, K. H. Kim, S. Hong, C. Kim, and B. Park, "Investigation of Chlorine-Mediated Microstructural Evolution of $CH_3NH_3PbI_3(Cl)$ Grains for High Optoelectronic Responses," *Nano Energy* **25**, 91 (2016).

12. J. Kim, T. Hwang, S. Lee, B. Lee, J. Kim, J. Kim, B. Gil, and B. Park, "Synergetic Effect of Double-Step Blocking Layer for the Perovskite Solar Cell." *J. Appl. Phys.* **122**, 145106 (2017).

13. T. Hwang, S. Lee, J. Kim, J. Kim, C. Kim, B. Shin, and B. Park, "Tailoring the Mesoscopic TiO_2 Layer: Concomitant Parameters for Enabling High-

Performance Perovskite Solar Cells," *Nanoscale Res. Lett*. **12**, 57 (2017).

14. M. Liu, M. B. Johnston, and H. J. Snaith, "Efficient Planar Heterojunction Perovskite Solar Cells by Vapour Deposition," *Nature* **501**, 395 (2013).

15. G. E. Eperon, V. M. Burlakov, P. Docampo, A. Goriely, and H. J. Snaith, "Morphological Control for High Performance, Solution Processed Planar Heterojunction Perovskite Solar Cells," *Adv. Funct. Mater*. **24**, 151 (2014).

16. D. Yang, X, Zhou, R. Yang, Z. Yang, W. Yu, X. Wang, C. Li, S. Liu, and R. P. H. Chang, "Surface Optimization to Eliminate Hysteresis for Record Efficiency Planar Perovskite Solar Cells," *Energy Environ. Sci*. **9**, 3071 (2016).

17. Z. M. Jarzebski, and J. P. Marton, "Physical Properties of SnO_2 Materials," *J. Electrochem. Soc*. **123**, 299C (1976).

18. Q. Jiang, L. Zhang, H. Wang, X. Yang, J. Meng, H. Liu, Z. Yin, J. Wu, X. Zhang, and J. You, "Enhanced Electron Extraction Using SnO_2 for High-Efficiency Planar-Structure $HC(NH_2)_2PbI_3$-Based Perovskite Solar Cells," *Nat. Energy* **2**, 16177 (2017).

19. E. H. Anaraki, A. Kermanpur, L. Steier, K. Domanski, T. Matsui, W. Tress, M. Saliba, A. Abate, M. Gratzel, A. Hagfeldt, and J.-P. Correa-Baena, "Highly Efficient and Stable Planar Perovskite Solar Cells by Solution-Processed Tin Oxide," *Energy Environ. Sci*. **9**, 3128 (2016).

20. D. Yang, R. Yang, K. Wang, C. Wu, X. Zhu, J. Feng, X. Ren, G. Fang, S. Priya, and S. Liu, "High Efficiency Planar-Type Perovskite Solar Cells with Negligible Hysteresis using EDTA-Complexed SnO_2," *Nat. Commun*. **9**, 3239 (2018).

21. G. Yang, C. Chen, F. Yao, Z. Chen, Q. Zhang, X. Zheng, J. Ma, H. Lei, P. Qin, L. Xiong, W. Ke, G. Li, Y. Yan, and G. Fang, "Effective Carrier-Concentration Tuning

of SnO$_2$ Quantum Dot Electron-Selective Layers for High-Performance Planar Perovskite Solar Cells," *Adv. Mater.* **30**, 1706023 (2018).

22. C. Huang, P. Lin, N. Fu, K. Sun, M. Ye, C. Liu, X. Zhou, L. Shu, X. Hao, B. Xu, X. Zeng, Y. Wang, and S, Ke, "Ionic Liquid Modified SnO$_2$ Nanocrystals as the Robust Electron Transporting Layer for Efficient Planar Perovskite Solar Cells," *J. Mater. Chem. A* **6**, 22086 (2018).

23. W. Ke, D. Zhao, A. J. Cimaroli, C. R. Grice, P. Qin, Q. Liu, L. Xiong, Y. Yan, and G. Fang, "Effects of Annealing Temperature of Tin Oxide Electron Selective Layers on the Performance of Perovskite Solar Cells," *J. Mater. Chem. A* **3**, 24163 (2015).

24. M. F. Aygüler, A. G. Hufnagel, P. Rieder, M. Wussler, W. Jaegermann, T. Bein, V. Dyakonov, M. L. Petrus, A. Baumann, and P. Docampo, "Influence of Fermi Level Alignment with Tin Oxide on the Hysteresis of Perovskite Solar Cells," *ACS Appl. Mater. Interfaces* **10**, 11414 (2018).

25. Y. Lee, S. Lee, G. Seo, S. Paek, K. T. Cho, A. J. Huckaba, M. Calizzi, D.-W. Choi, J.-S. Park, D. Lee, H. J. Lee, A. M. Asiri, and M. K. Nazeeruddin, "Efficient Planar Perovskite Solar Cells Using Passivated Tin Oxide as an Electron Transport Layer," *Adv. Sci*. **5**, 1800130 (2018).

26. C. Xiao, C. Wang, W. Ke, B. P. Gorman, J. Ye, C.-S. Jiang, Y. Yan, and M. M. Al-Jassim, "Junction Quality of SnO$_2$-Based Perovskite Solar Cells Investigated by Nanometer-Scale Electrical Potential Profiling," *ACS Appl. Mater. Interfaces* **9**, 38373 (2017).

27. S. Ravishankar, S. Gharibzadeh, C. Roldan-Carmona, G.´ Grancini, Y. Lee, M. Ralaiarisoa, A. M. Asiri, N. Koch, J. Bisquert, and M. K. Nazeeruddin, "Influence

of Charge Transport Layers on Open-Circuit Voltage and Hysteresis in Perovskite Solar Cells," *Joule* **2**, 788 (2018).

28. B. Lee, S. Lee, D. Cho, J. Kim, T. Hwang, K. H. Kim, S. Hong, T. Moon, and B. Park, "Evaluating the Optoelectronic Quality of Hybrid Perovskites by Conductive Atomic Force Microscopy with Noise Spectroscopy," *ACS Appl. Mater. Interfaces* **8**, 30985 (2016).

29. T. Hwang, B. Lee, J. Kim, S. Lee, B. Gil, A. J. Yun, and B. Park, "From Nanostructural Evolution to Dynamic Interplay of Constituents: Perspectives for Perovskite Solar Cells," *Adv. Mater*. **30**, 1704208 (2018).

30. D. Cho, T. Hwang, D.-G. Cho, B. Park, and S. Hong, "Photoconductive Noise Microscopy Revealing Quantitative Effect of Localized Electronic Traps on the Perovskite-Based Solar Cell Performance," *Nano Energy* **43**, 29 (2018).

31. D.-Y. Son, S.-G. Kim, J.-Y. Seo, S.-H. Lee, H. Shin, D. Lee, and N.-G. Park, "Universal Approach toward Hysteresis-Free Perovskite Solar Cell via Defect Engineering," *J. Am. Chem. Soc.* 140, 1358 (2018).

32. Y. Hu, E. M. Hutter, P. Rieder, I. Grill, J. Hanisch, M. F. Aygüler, A. G. Hufnagel, M. Handloser, T. Bein, A. Hartschuh, K. Tvingstedt, V. Dyakonov, A. Baumann, T. J. Savenije, M. L. Petrus, and P. Docampo, "Understanding the Role of Cesium and Rubidium Additives in Perovskite Solar Cells: Trap States, Charge Transport, and Recombination," *Adv. Energy Mater.* **8**, 1703057 (2018).

33. H. J. Jung, D. Kim, S. Kim, J. Park, V. P. Dravid, and B. Shin. "Stability of Halide Perovskite Solar Cell Devices: In Situ Observation of Oxygen Diffusion under Biasing," *Adv. Mater*. **30**, 1802769 (2018).

34. S. S. Wilson, J. P. Bosco, Y. Tolstova, D. O. Scanlon, G. W. Watson, and H. A.

Atwater, "Interface Stoichiometry Control to Improve Device Voltage and Modify Band Alignment in ZnO/Cu$_2$O Heterojunction Solar Cells," *Energy Environ. Sci*. **7**, 3606 (2014).

35. A. Pockett, G. E. Eperon, N. Sakai, H. J. Snaith, L. M. Peter, and P. J. Cameron, "Microseconds, Milliseconds and Seconds: Deconvoluting the Dynamic Behaviour of Planar Perovskite Solar Cells," *Phys. Chem. Chem. Phys*. **19**, 5959 (2017).

36. H. H. Park, R. Heasley, L. Sun, V. Steinmann, R. Jaramillo, K. Hartman, R. Chakraborty, P. Sinsermsuksakul, D. Chua, T. Buonassisi, and R. G. Gordon, "Co-Optimization of SnS Absorber and Zn(O,S) Buffermaterials for Improved Solar Cells," *Prog. Photovolt*aics **23**, 901 (2015).

37. J. Dagar, S. Castro-Hermosa, G. Lucarelli, F. Cacialli, and T. M. Brown, "Highly Efficient Perovskite Solar Cells for Light Harvesting under Indoor Illumination via Solution Processed SnO$_2$/MgO Composite Electron Transport Layers," *Nano Energy* **49**, 290 (2018).

38. I. Zarazua, G. Han, P. P. Boix, S. Mhaisalkar, F. FabregatSantiago, I. Mora-Sero, J. Bisquert, G. Garcia-Belmonte, "Surface Recombination and Collection Efficiency in Perovskite Solar Cells from Impedance Analysis," *J. Phys. Chem. Lett*. **7**, 5105 (2016).

39. O. Almora, C. Aranda, E. Mas-Marza, G. Garcia-Belmonte, "On Mott-Schottky Analysis Interpretation of Capacitance Measurements in Organometal Perovskite Solar Cells," *Appl. Phys. Lett*. **109**, 173903 (2016).

40. T. Walter, R. Herberholz, C. Müller, and H. W. Schock, "Determination of Defect Distributions from Admittance Measurements and Application to Cu(In,Ga)Se$_2$

Based Heterojunctions," *J. Appl. Phys*. **80**, 4411 (1996).

41. O. Almora, A. Guerrero, and G. Garcia-Belmonte, "Ionic Charging by Local Imbalance at Interfaces in Hybrid Lead Halide Perovskites," *Appl. Phys. Lett*. **108**, 043903 (2016).

42. I. Zarazua, J. Bisquert, and G. Garcia-Belmonte, "Light-Induced Space-Charge Accumulation Zone as Photovoltaic Mechanism in Perovskite Solar Cells," *J. Phys. Chem. Lett*. **7**, 525 (2016).

43. S. A. L. Weber, I. M. Hermes, S.-H. Turren-Cruz, C. Gort, V. W. Bergmann, L. Gilson, A. Hagfeldt, M. Gratzel, W. Tress, and R. Berger, "How the Formation of Interfacial Charge Causes Hysteresis in Perovskite Solar Cells," *Energy Environ. Sci*. **11**, 2404 (2018).

44. J.-W. Lee, D.-H. Kim, H.-S. Kim, S.-W. Seo, S. Cho, and N.-G. Park, "Formamidinium and Cesium Hybridization for Photo- and Moisture-Stable Perovskite Solar Cell," *Adv. Energy Mater*. **5**, 1501310 (2015).

45. D. Prochowicz, P. Yadav, M. Saliba, M. Saski, S. M. Zakeeruddin, J. Lewinski, and M. Gratzel, "Reduction in the Interfacial Trap¨ Density of Mechanochemically Synthesized $MAPbI_3$," *ACS Appl. Mater. Interfaces* **9**, 28418 (2017).

46. M. Samiee, S. Konduri, B. Ganapathy, R. Kottokkaran, H. A. Abbas, A. Kitahara, P. Joshi, L. Zhang, M. Noack, and V. Dalal, "Defect Density and Dielectric Constant in Perovskite Solar Cells," *Appl. Phys. Lett*. **105**, 153502 (2014).

Chapter 6.

Triamine-Based Aromatic Cation as a Novel Stabilizer for Efficient Perovskite Solar Cells

6.1. Introduction

Organometallic perovskite is one of the most popular research areas, and the solar cell application of perovskite materials is gaining enormous attention with the rapid growth.   Throughout the extensive work, the power conversion efficiency (PCE) of perovskite solar cells is soaring up to 24.2%, and the stabilities are gradually improving [1,2].   Even though the PCE of the perovskite solar cell is already comparable to those of commercial demands, the stability is not satisfactory enough to replace the conventional photovoltaics.

Perovskite solar cells are generally designed to have device architectures of either *p-i-n* or *n-i-p* type.   The perovskite layer (*i*) plays very important role as the main light absorber, but it is highly reactive under heat, humidity, and light.   Although *n-* or *p-* type carrier transport layers of metal oxides, polymers, or small molecules also count for device properties [3-16], stabilizing the perovskite itself is the most important to realize stable solar-cell device.   It is well known that triple-cation perovskite {$Cs_{0.05}(FA_{0.85}MA_{0.15})_{0.95}Pb(I_{0.85}Br_{0.15})_3$, where FA is $(NH_2)_2CH^+$ and MA is $CH_3NH_3^+$} is one of the most stable perovskite materials [17-20].   However, FA and MA are

highly reactive under heat, humidity, and light, requiring additional modification to further improve the quality of perovskite [5,21-25].

Although the organic-based p-type materials (the most common one for the perovskite solar cells: spiro-OMeTAD) can have a stability problem [26,27], recent researches have revealed that ion doping or alloying of perovskite can largely improve the device stability, compensating the stability issues of spiro-OMeTAD.   In more detail, metal-halide doping or organic alloying surely help the device stability by forming a strong bonding within the lattice or passivating the defects [5,9,25,28-33]. The surface passivation on the perovskite is also introduced as an effective method to reduce the degradation of materials, even though it only stabilizes the interface, and the bulk properties of perovskite may still remain unstable [34-36].   Therefore, the doping or alloying of perovskite is highly practical and straightforward method to improve the materials stability, and thereby the performance of solar cells.

Herein, we introduce 1,2,4-triazole ($C_2H_3N_3$) as a cation solute in triple-cation perovskite, since 1,2,4-trizole is an aromatic compound that is extremely stable compared to FA or MA [37-41].   1,2,4-triazole is a triamine-based aromatic compound, having a strong interaction within the perovskite structure, and also improving the charge transport behavior of cation site of the perovskite [5,42-47]. However, because of its relatively large size (~258 pm), 1,2,4-triazole in perovskite is limited to a small amount in order to maintain satisfactory tolerance factor [48].   By optimizing the content of 1,2,4-triazole alloy, the optical and electronic properties are improved boosting the PCE up to 20.9%.   Furthermore, the thermal stability of the solar cell is confirmed under the extreme condition (85°C/85% relative humidity (RH)) for 700 h to address the optimum strategy of perovskite and device stabilization.

6.2. Experimental Section

Synthesis of Triazole-Soluted Perovskite: 1,2,4-triazole ($C_2H_3N_3$; Sigma-Aldrich) was mixed with hydrogen iodide solution (HI, Sigma-Aldrich) with 3:1 molar ratio in a round-bottom flask at 0°C for 2 h under stirring. After the solvent was evaporated at 70°C for 12 h, the precipitate was washed with diethyl ether (Daejung) for ten times. The precipitate was dried at 60°C for 24 h in a vacuum oven to complete the synthesis of triazolium iodide ($C_2H_4N_4I$).

For the perovskite film, 1.8 M $Cs_{0.05}(FA_{0.85}MA_{0.15})_{0.95}Pb(I_{0.85}Br_{0.15})_3$ perovskite precursor solution was prepared by dissolving formamidinium iodide (FAI; Great Solar Laboratory), methylammonium bromide (MABr; Great Solar Laboratory), lead iodide (PbI_2; TCI Chemicals), lead bromide ($PbBr_2$; TCI Chemicals), and cesium iodide (CsI; Great Solar Laboratory) into a mixture of *N,N*-dimethylformamide (DMF; Sigma-Aldrich) and dimethyl sulfoxide (DMSO; Sigma-Aldrich).

To prepare the 1,2,4-triazole-alloyed perovskite, 1.8 M of stock solution of 1,2,4-triazolium perovskite was made by mixing triazolium iodide, PbI_2, and $PbBr_2$ into DMF:DMSO mixture solution to make a $TAPbI_{0.85}Br_{0.15}$ (100% of triazole cation, where TA indicates triazolium ion), then the completed stock solution was stoichiometrically diluted (0, 2, 4, or 6 mol. %) in a solution of prepared $Cs_{0.05}(FA_{0.85}MA_{0.15})_{0.95}Pb(I_{0.85}Br_{0.15})_3$.

Device Fabrication: Indium-doped tin oxide (ITO; AMG) was cleaned under sonication in acetone, ethanol, and deionized water. Then SnO_2 was spin-coated on

a cleaned substrate with the previously developed method.[67]   The perovskite solution was sonicated for 30 min, and then spin-coated on the as-prepared SnO_2 layer in two steps of spinning program: 500 rpm for 5 s for the first step and 5000 rpm for 20 s for the second step.   1 mL of diethyl ether (Daejung) was dropped 5 s before the second spin-step ended, and the substrate was annealed at 105°C for 40 min on a hot plate.   Hole transporting material was prepared by dissolving 72.3 mg of spiro-OMeTAD (Lumtec) in 1 mL of chlorobenzene (Sigma-Aldrich), and 28.8 μL of 4-*tert*-butylpyridine (Sigma-Aldrich) and 17.5 μL of bis(trifluoromethane)sulfonimide lithium salt (Sigma-Aldrich) in acetonitrile (520 mg mL^{-1}) were added as additives.   The solution was spin-coated on the substrate, and finally 100-nm thick Au electrode was thermally evaporated.

Encapsulation: Fabricated device was sealed with encapsulation glass (AMG) by attaching getter (HD-S071313W-48; AD TECH) and dispensing the epoxy (XNR5570; Nagase) on an edge of the encapsulation glass.   UV-curing (OmniScience) system was applied for 10 min to an epoxy to complete the glass encapsulation.

Characterization: FTIR (Nicolet iS50; Thermo Fisher) was conducted to characterize the organic bonding nature of the perovskite.   Phases of the synthesized samples were characterized by XRD (D8 Advance; Scientific).   The field-emission scanning electron microscope (FE-SEM; Merlin-Compact; Carl Zeiss) was used to observe the morphologies of alloyed perovskite.   Work function and VBM of perovskite films were measured via multipurpose x-ray photoelectron spectroscopy (XPS; Sigma Probe; Thermo VG Scientific), conducted with argon

sputtering, and photon energy of $hv = 21.22$ eV was used in the ultraviolet photoelectron spectroscopy (UPS) measurement. Optical properties of the perovskite films were measured with UV-vis spectroscopy (V-770; JASCO) with an integrating sphere. PL (FlouTime300; PicoQuant) was conducted to understand the carrier recombination. Incident photon to current efficiency (IPCE) measurements were performed by solar cell IPCE system (K3100; McScience). For impedance analysis, a potentiostat (Zive SP-1; WonATech) was adopted, and the impedance of photovoltaic device was measured with 10 mV AC perturbation in the frequency range from 10 mHz to 100 kHz under zero bias in dark condition. Photocurrent density-voltage (J-V) curves were achieved via solar cell measurement system (K-3000; McScience) for an active area of 0.09 cm^2.

6.3. Results and Discussion

Concerns regarding the perovskite stability are widely discussed in the solar-cell field, and it is realized that the perovskite layer plays a critical role for the degradation of devices [5,21-25,49-51]. The major degradation sources of the perovskite are organic species of the cations which degrade under humidity, heat and light, and further modification of such species is required to design more practical perovskite materials [21-25,47]. 1,2,4-triazole has triamine-based aromatic structure, and it possibly allows a strong interaction within the lattice as well as the energy minimization by the tilting behavior of an organic cation, leading to the structural stabilization [5,51-53]. Also, orientation of amine groups in 1,2,4-triazole tends to make them repel one another, resulting in a reduced dipole moment compared with the 1,2,3-triazole or imidazole, obtaining strong advantages over different multiamine-based ring-shaped molecules [54-57]. The low dipole moment reduces the reactivity with water, guaranteeing the high stability under the humid condition. Furthermore, 1,2,4-triazole is less volatile species than imidazole, MA or FA, making it the ideal stabilizer for the perovskite solute under the operating conditions [58,59].

Figure 6-1(a) illustrates the schematics of 1,2,4-triazole alloying in triple-cation perovskite. By analyzing the 1,2,4-triazole-alloyed perovskite film, x-ray diffraction (XRD) shows (110) peak shift towards lower angle and (224) and (314) peaks to the opposite direction, due to the transition into tetragonal phase by the 1,2,4-triazole solute in a triple-cation perovskite (Fig. 6-1(b)). When the solute is added up to 6%, a PbI_2 peak is observed with the reduced peak intensities of triple-cation perovskite, indicating the structural instability by excessive alloying (Fig. 6-

2(a)).   In order to advocate the phenomena, tolerance factor is calculated to be ~1.01 for the 6% alloying (values between 0.9 - 1.0 as a stable structure) [19,48].   To identify the molecular structure of 1,2,4-triazole solute in the perovskite, Fourier-transform infrared (FTIR) analysis is further conducted for the alloyed perovskite film (Fig. 6-1(c)), where a clear peak of N=N in ~1600 cm^{-1} can be seen after the incorporation of aromatic cations (raw data presented in Fig. 6-2(b)).

Aside from the lattice change, film morphologies are also analyzed to address the advantages of 1,2,4-triazole alloying.   As shown in Fig. 6-3(a), 2% and 4% alloys exhibit uniformly sized grains, where 0% and 6% show multiple-size distributions which may be the imperfect grains or PbI$_2$, respectively.   In Fig. 6-3(b), the root-mean-square (rms) roughnesses and conductivities of perovskite films are addressed, confirming that the proper alloying in perovskite increases the quality of the perovskite films by the lattice stabilization.   Topological images from the atomic-force microscopy (AFM) and optical images are also presented in Figs. 6-4 and 6-5.   It can be seen that 6% alloy exhibits the highest conductivity, and this value originate from the mixed conductivity of PbI$_2$ and alloyed perovskite (Fig. 6-2(a)).   However, the improved conductivity of 2% or 4% alloy originates from the substitution of triazole, which contains delocalized aromatic structure to transport the charge efficiently within the perovskite lattice, contributing to the improved optoelectronic properties of perovskite materials [5,45].

Defects and traps of materials significantly affect the ion diffusion as well as charge carrier dynamics within the device, and the analyses and understanding of these defect states are undoubtedly important to improve both the device performance and stability.   In order to investigate the carrier dynamics and recombination behaviors in

the perovskite films, time-resolved photoluminescence (TRPL), photoluminescence (PL), and absorptance are measured.   As shown in Fig. 6-6(a), the alloy with 2% of 1,2,4-triazole exhibits the longest carrier lifetime, with the reduced traps expected. Interestingly, carrier lifetimes of 4% and 6% alloys are observed to be shorter than that of the bare perovskite, indicating the excessive alloying destabilizes the perovskite lattice.   To further obtain the insights, absorption coefficients and steady-state PL are measured, with the 2% alloy exhibiting the lowest defects with the highest absorption and PL intensities (evidences for the strong excitation and radiative recombination, respectively).   However, the PL of bare and 4% alloys are red shifted, indicating that the shallow traps are reduced in the 2% alloy (with small changes in the bandgap, as illustrated in Fig. 6-7(a)).   Comparison of PL and bandgap indicates the modified traps at the shallow level, which can be highly influenced by the quality of perovskite and interfaces.   Perovskite with 6% alloying forms PbI_2 (Fig. 6-2(a)), which ruins the proper recombination and weakens the optoelectronic properties. Based on the measured work function and valance band maximum (VBM) with the bandgap energy, the band structure of perovskite with proper 2% alloying is moving towards n-type, thereby enhancing the electron transport (Figs. 6-6(b) and 6-7(b)). However, excessive alloying is not proper due to the lattice defects, making the light absorber less n-type and leading to an ineffective charge transport for the device performance.
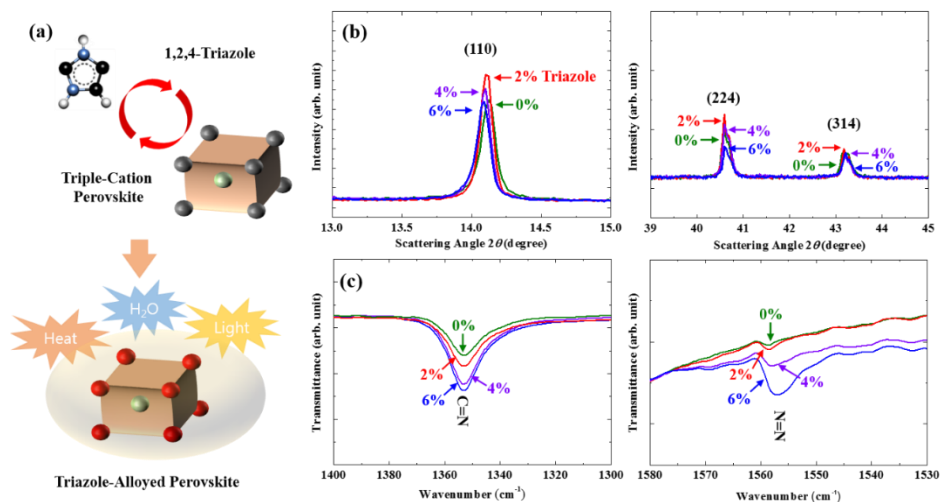
Fig. 6-1.   Schematics and characterization of perovskite films.   (a) Illustration for 1,2,4-triazole alloying in the triple-cation perovskite, and (b) the observed peak shift in XRD by alloying process.   (c) Typical functional groups (C=N and N=N) in the 1,2,4-triazole alloyed perovskite by FTIR analysis.
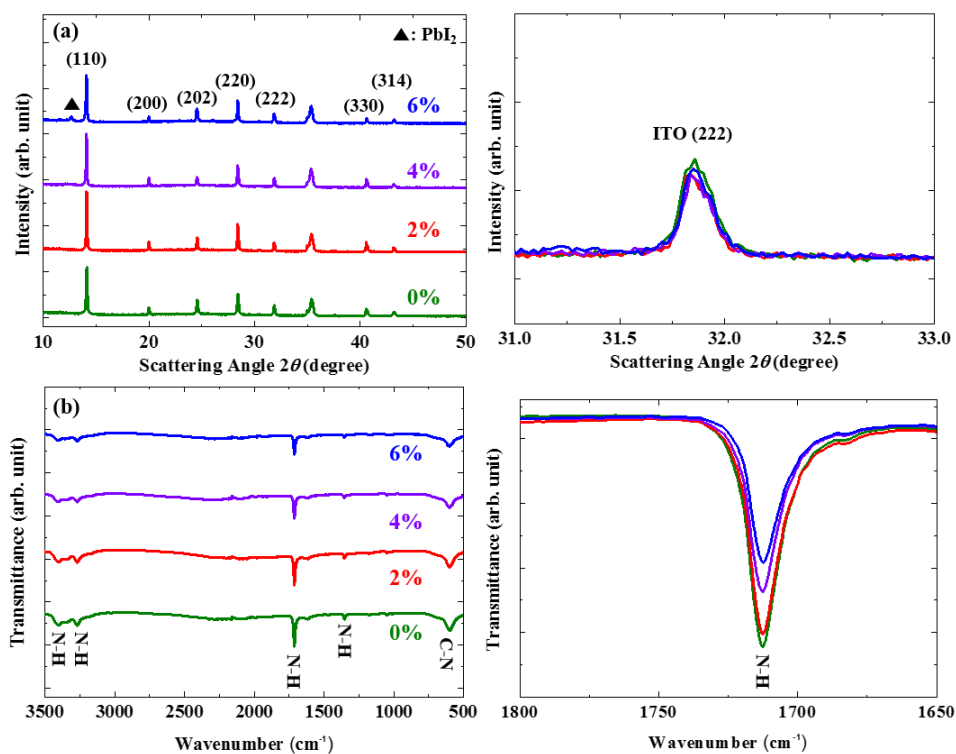
Fig. 6-2.   Characterization of perovskite films.   (a) XRD with the ITO peak to confirm the clear peak shifting due to the alloying (Fig. 6-1(b)).   (b) FTIR exhibiting the reduced N-H bonding by 1,2,4-triazole (Fig. 6-1(c)).
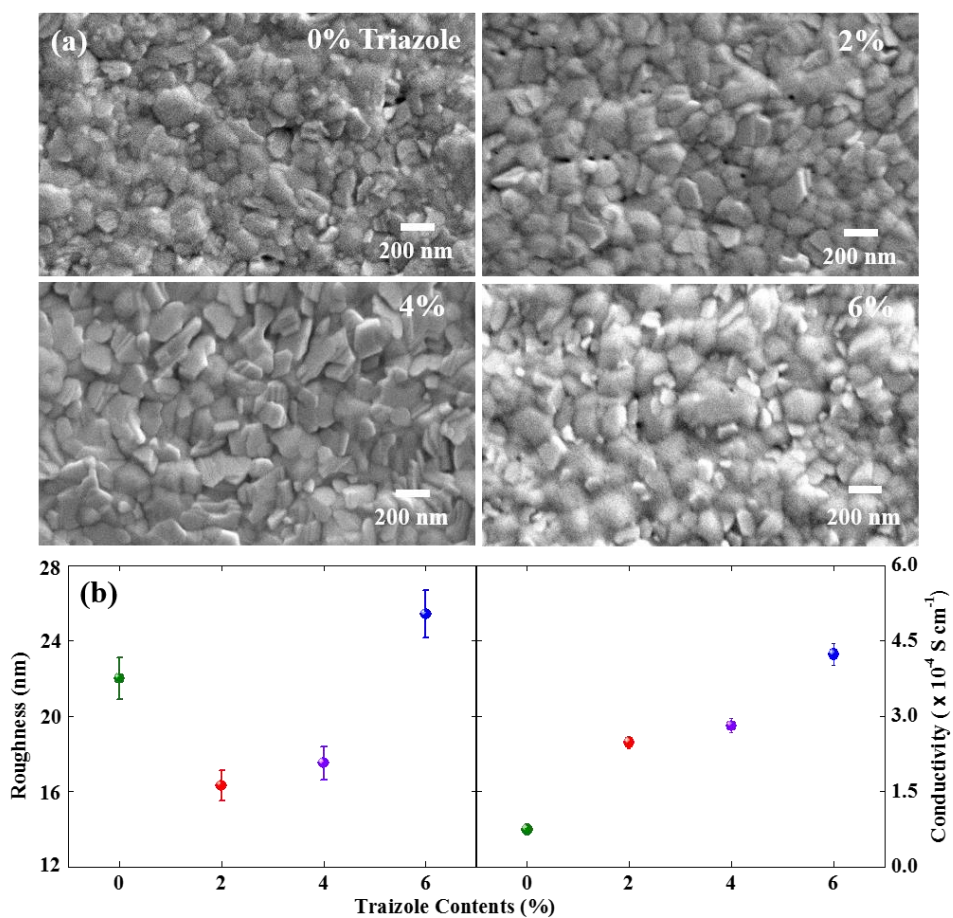
Fig. 6-3. Morphological and electrical characteristics of perovskite films. (a) SEM images of the 1,2,4-traizole-alloyed perovskite. (b) Film roughness and conductivity of 1,2,4-triazole-alloyed perovskite, as measured by AFM and 4-point probe. The 6%-alloyed film exhibits PbI_2 phase, leading to high roughness and conductivity.
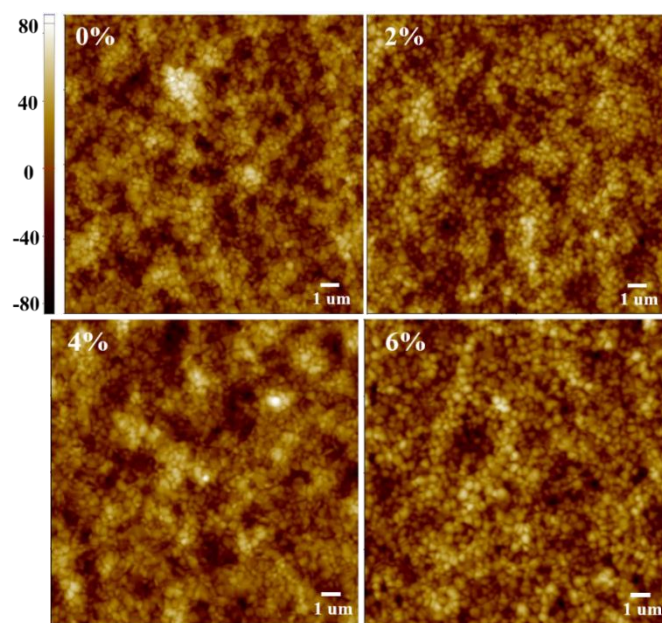
Fig. 6-4.　Roughness of perovskite films.　Topology of bare and 1,2,4-triazole-alloyed perovskite films.
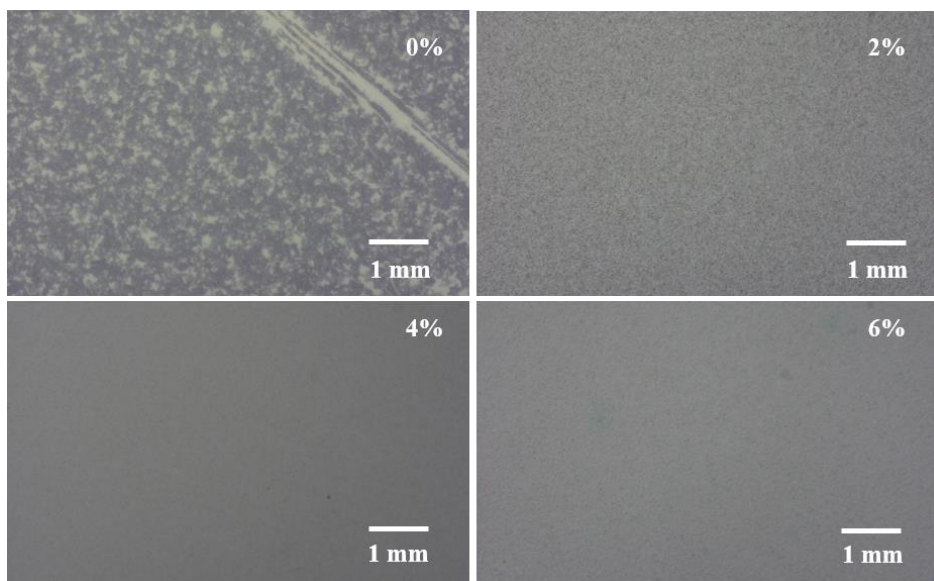
Fig. 6-5.   Optical images of bare and 1,2,4-triazole-alloyed perovskite.
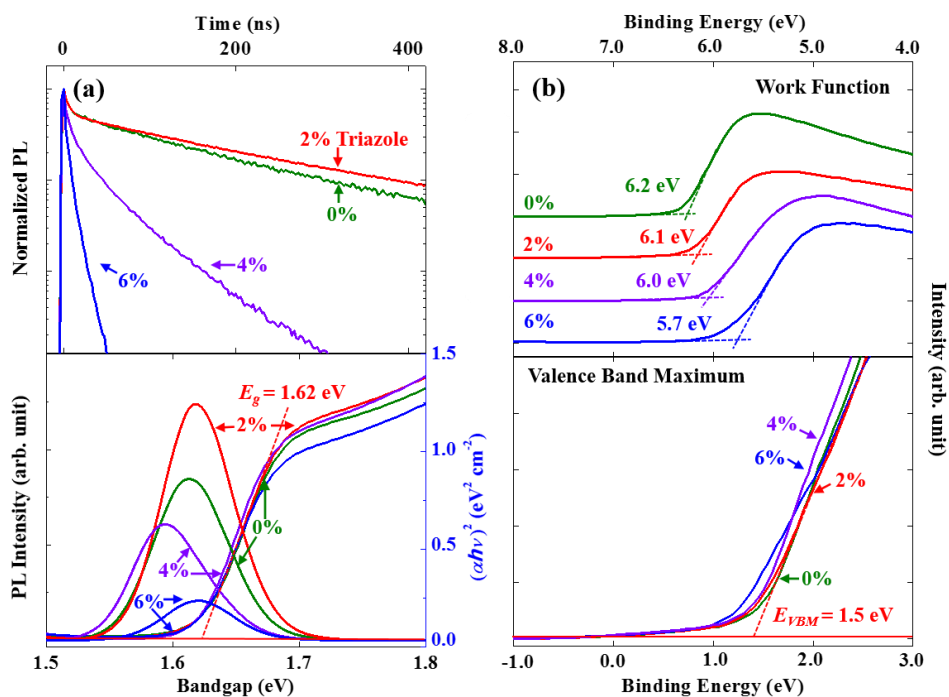
Fig. 6-6.   Carrier and optoelectronic properties of perovskite films.   (a) Carrier

lifetime of 1,2,4-triazole-alloyed perovskite: TRPL, PL data, and

bandgap determination by $(\alpha h\nu)^2$ vs. $h\nu$.   (b) Electronic structures of

1,2,4-triazole-alloyed perovskite by UPS: work function and VBM.
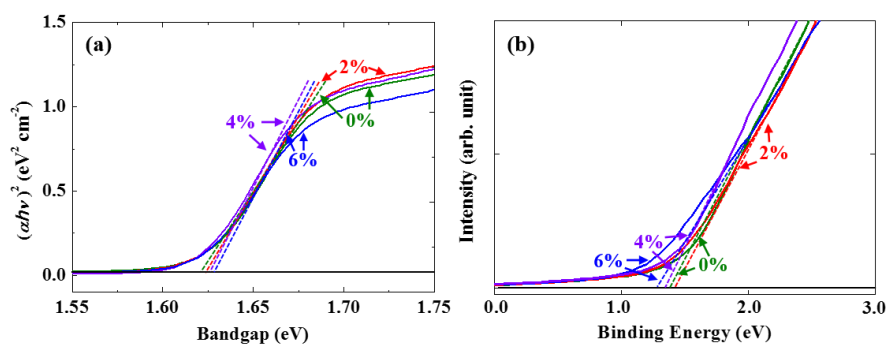
Fig. 6-7.   Changes in the (a) bandgap and (b) VBM of 1,2,4-triazole-alloyed perovskite.

To further explicate the characteristics of charge carriers and electronic structures, the electronic traps of the devices with various 1,2,4-triazole alloy contents are quantitatively analyzed. It is known that various phenomena including carrier accumulation and charging/discharging of electronic traps contribute to the capacitive feature of the device, and therefore a proper interpretation of the device capacitance can elucidate its defective characteristics in a perovskite solar cell [60-66]. The capacitance of a device is obtained from the impedance spectroscopy, and capacitance vs. frequency (C-f) is plotted in Fig. 6-8(a). While the capacitances of various alloys are all identical at high-frequency region, the low-frequency capacitances show differences indicating that the electronic trap states change by the addition of 1,2,4-triazole. For further understanding, deep-trap density is calculated from the C-f plot, and the distribution of trap states is depicted in Fig. 6-8(b) [17,67]. The 2%-alloyed device exhibits trap states shifting toward the bandedge plus reduced trap density compared to the bare-, 4%-, and 6%- alloyed perovskite solar cells, rationalizing its improved carrier transport observed by PL analysis. The shallow traps of 2% alloy possibly reduce the carrier recombination and provide facile charge transfer to the carrier-transport materials (SnO_2 and spiro-OMeTAD for electrons and holes, respectively). Schematics for carrier dynamics at the interfaces are drawn in Fig. 6-8(c) with the considerations of band diagram (from Figs. 6-6 and 6-7).

The photovoltaic performances of solar cells are illustrated in Fig. 6-9(a) and Table 6-1. While devices with 2% alloy exhibits the highest efficiencies with low hysteresis, devices with 4% and 6% alloys result in low reproducibility (Fig. S5) due

to the high concentration of deep-level defects and impurities (Figs. 6-2, 6-3, and 6-8).   Steady-state current and external quantum efficiency (EQE) are also shown (Figs. 6-9(b) and (c)), where the 2%-alloyed device exhibits stable current up to 1000 s with the highest EQE.   TRPL is once more conducted in SnO_2/perovskite/spiro-OMeTAD structure (Fig. 6-9(d)) to confirm how well carriers are transferable.   The tendencies are well matched with the performance of perovskite solar cells, exhibiting that the 2%-alloyed perovskite is the optimum light-absorber material for the device efficiency.

Lastly, to evaluate the effect of 1,2,4-triazole on the stability of the device, the alloyed perovskite solar cells are compared with the bare device under the extreme condition (85°C/85% RH).   While the perovskite solar cell without alloying sustains 90% of initial PCE for ~200 h (Fig. 6-11), 2%-alloyed perovskite solar cell sustains 90% PCE for more than 700 h, leading to a potential for the ultrastable perovskite materials. Thermally stable photovoltaic device is enabled thanks to the improved structural stability and passivated defects of 2%-alloyed perovskite, whereas 4%- and 6%- alloyed ones possess structural instability and deteriorative defect/trap characteristics as observed in this study.
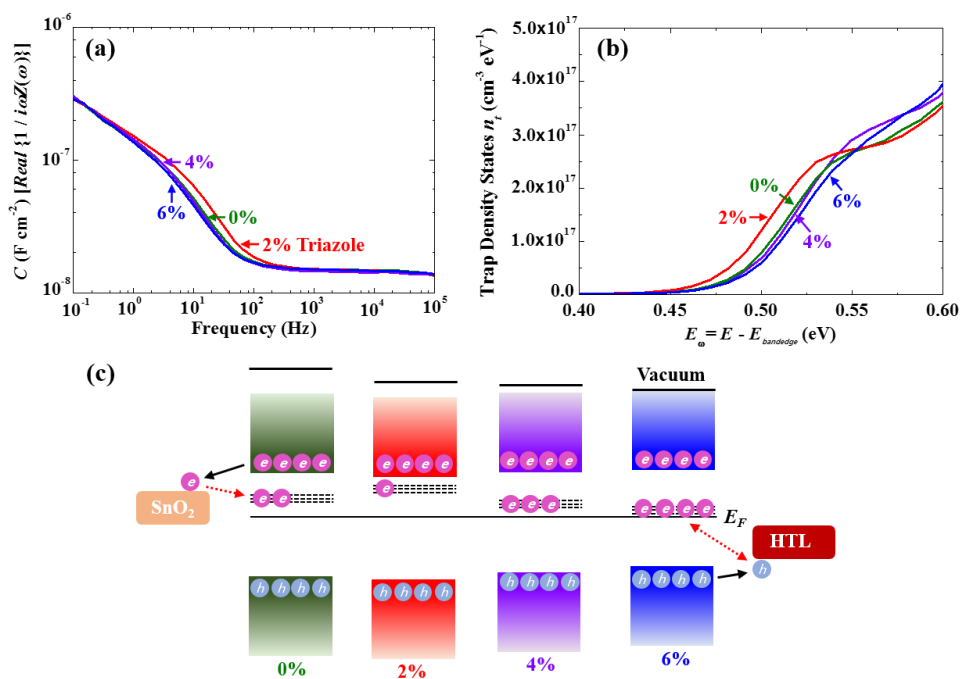
Fig. 6-8. Electronic-trap states of perovskite films. (a) Capacitance-frequency plot and (b) trap-distribution spectra of solar cells with the 1,2,4-triazole-alloyed perovskite. (c) Schematic illustration for the band diagram and trap state in the device.
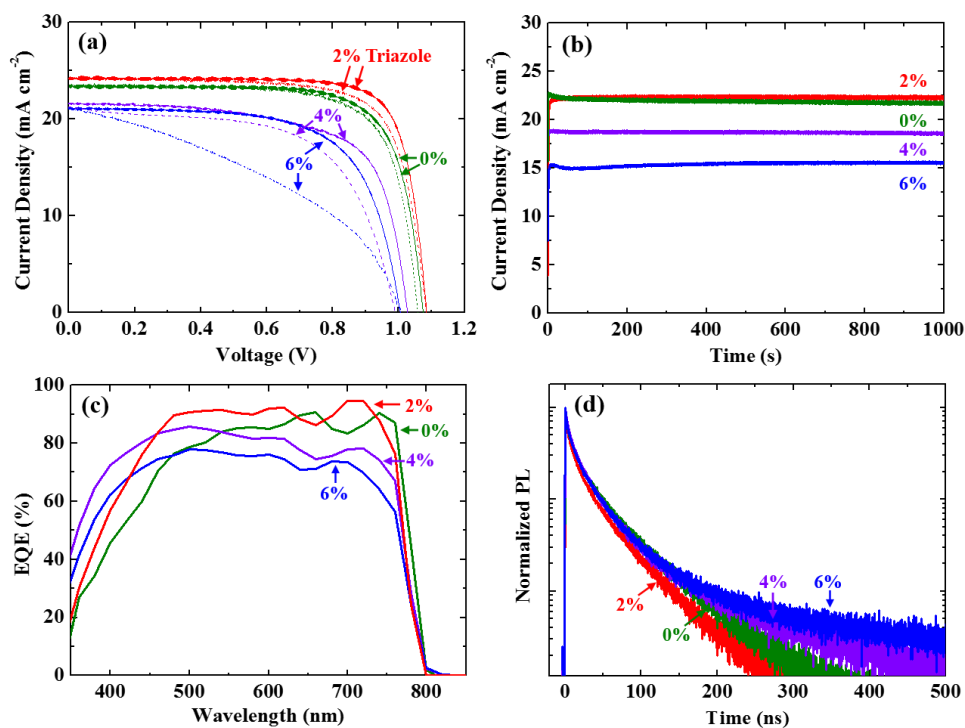
Fig. 6-9. Photovoltaic performance of perovskite solar cells.   (a) *J-V* curves (scan

rate: 10 mV s^{-1}), (b) steady-state current for 1000 s, and (c) EQE spectra

for the bare and 1,2,4-triazole-alloyed perovskite solar cells.   (d) TRPL

spectra   with   the   bare   and   1,2,4-triazole-alloyed   perovskite

(FTO/SnO$_2$/perovskite/spiro-OMeTAD).

Triazole Content	J_{sc} (mA cm^{-2})	V_{oc} (Voltage)	FF (%)	η (%)
0 % (rev.)	23.2	1.07	0.76	18.9 (17.0 ± 1.2)
0 % (for.)	23.5	1.05	0.74	18.4 (16.8 ± 1.0)
2 % (rev.)	24.4	1.09	0.79	20.9 (19.1 ± 1.1)
2 % (for.)	24.4	1.08	0.74	19.6 (18.3 ± 1.0)
4 % (rev.)	21.7	1.03	0.67	15.0 (12.4 ± 1.8)
4 % (for.)	21.3	0.99	0.61	12.9 (10.8 ± 1.4)
6 % (rev.)	21.0	1.00	0.67	14.2 (10.4 ± 2.7)
6 % (for.)	21.0	1.01	0.40	8.60 (6.3 ± 2.2)

Table 6-1.   The highest and average values of the device performance. Photovoltaic performance of perovskite solar cells with 1,2,4-triazole alloyed.
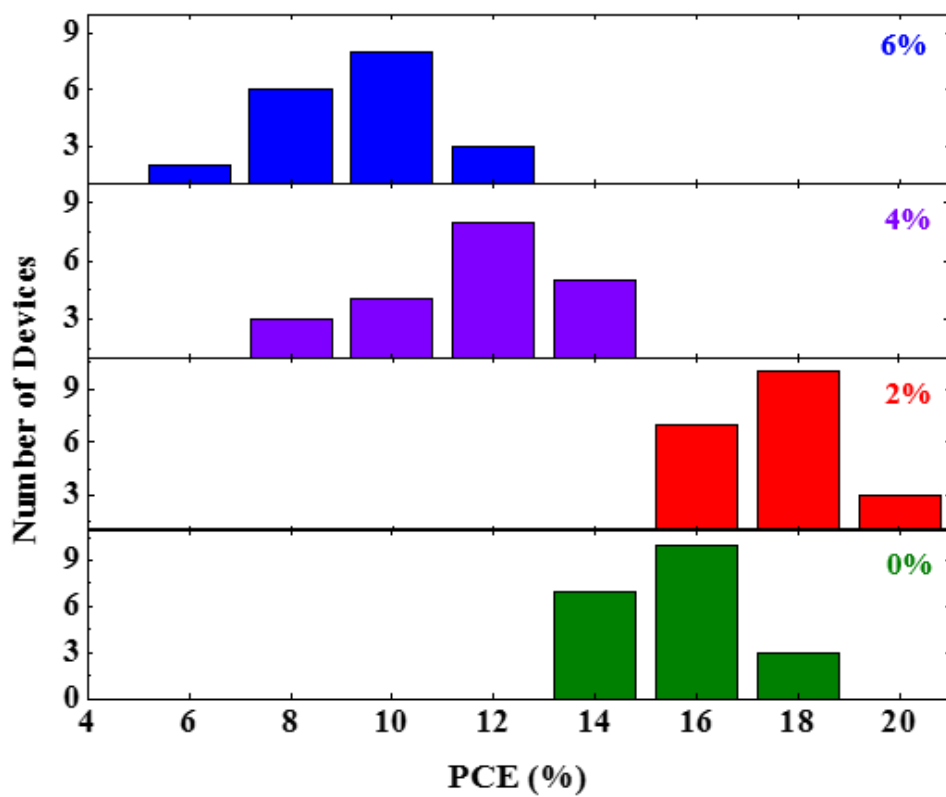
Fig. 6-10.   Device reproducibility of bare and 1,2,4-triazole-alloyed perovskite.
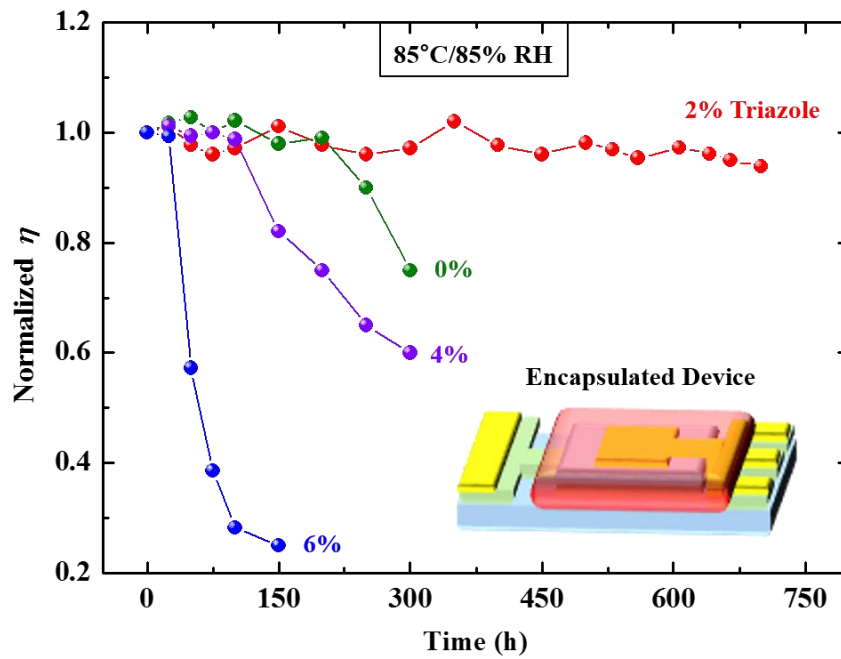
Fig. 6-11.   Device stability under 85°C/85% RH environment (encapsulated).

6.4. Conclusions

Obtaining high PCE and stability for the perovskite solar cells are the major bottlenecks for commercialization. Even though the triple-cation perovskite is well known for its stability, reactive species and weak bonding sites of organic cations (MA and FA) still provide rooms for the further improvement. Herein, we have alloyed 1,2,4-triazole as a cation solute in perovskite to minimize defects and thereby enhance the optoelectronic properties of perovskite, leading to the achievement of superior performance and stability under extreme conditions. To satisfy the structural stabilization, the addition of 1,2,4-triazole is optimally controlled, and the devices with 2%-alloyed perovskite exhibits the PCE of 20.9% with the superior stability compared with the device without solute. These straightforward and novel strategies can support further development for the perovskite research and practical commercialization.

6.5. References

1. NREL Efficiency chart, https://www.nrel.gov/pv/cell-efficiency.html, access on June 21, 2019.

2. W. Chen, Y. Wu, Y. Yue, J. Liu, W. Zhang, X. Yang, H. Chen, E. Bi, I. Ashraful, M. Grätzel, and L. Han, "Efficient and stable large-area perovskite solar cells with inorganic charge extraction layers," *Science* **350**, 944 (2015).

3. J. Lian, B. Lu, F. Niu, P. Zeng, and X. Zhan, "Electron-Transport Materials in Perovskite Solar Cells," *Small Methods* **2**, 1800082 (2018).

4. Z. Song, S. C. Watthage, A. B. Phillips, G. K. Liyanage, R. R. Khanal, B. L. Tompkins, R. J. Ellingson, and M. J. Heben, "Investigation of Degradation Mechanisms of Perovskite-Based Photovoltaic Devices using Laser Beam Induced Current Mapping," *Proc. of SPIE* **9561**, 956107 (2015).

5. J. Kim, T. Hwang, B. Lee, S. Lee, K. Park, H. H. Park, and B. Park, "An Aromatic Diamine Molecule as the *A*-Site Solute for Highly Durable and Efficient Perovskite Solar Cells," *Small Methods* **3**, 1800361 (2019).

6. T. Moon, G. S. Shin, and B. Park, ""Development of Carbon-Based Cathodes for Li-Air Batteries: Present and Future," *Electron. Mater. Lett*. **11**, 917 (2015).

7. D.-R. Jung, J. Kim, C. Nahm, H. Choi, S. Nam, and B. Park, "Review Paper: Semiconductor Nanoparticles with Surface Passivation and Surface Plasmon," *Electron. Mater. Lett*. **7**, 185 (2011).

8. J. Lian, B. Lu, F. Niu, P. Zeng, and X. Zhan, "Electron-Transport Materials in Perovskite Solar Cells," *Small Methods* **2**, 1800082 (2018).

9. N. Li, S. Tao, Y. Chen, X. Niu, C. K. Onwudinanti, C. Hu, Z. Qiu, Z. Xu, G. Zheng, L. Wang, Y. Zhang, L. Li, H Liu, Y. Lun, J. Hong, X. Wang, Y. Liu, H. Xie, Y. Gao, Y. Bai, S. Yang, G. Brocks, Q. Chen, and H. Zhou, "Cation and Anion Immobilization through Chemical Bonding Enhancement with Fluorides for Stable Halide Perovskite Solar Cells," *Nat. Energy* **4**, 408 (2019).

10. M. Gabski, S. Ostendorp, M. Peterlechner, and G. Wilde, "Stability and Performance of Nanostructured Perovskites for Light-Harvesting Applications" *Small Methods* **3**, 1800404 (2019).

11. S. S. Wilson, J. P. Bosco, Y. Tolstova, D. O. Scanlon, G. W. Watson, and H. A. Atwater, "Interface Stoichiometry Control to Improve Device Voltage and Modify Band Alignment in ZnO/Cu2O Heterojunction Solar Cells," *Energy Environ. Sci.* **2014**, *7*, 3606.

12. A. Mihi, C. Zhang, and P. V. Braun, "Transfer of Preformed Three-Dimensional Photonic Crystals onto Dye-Sensitized Solar Cells," *Angew. Chem. Int. Ed.* **50**, 5712 (2011).

13. H.-T. Lien, D. P. Wong, N.-H. Tsao, C.-I Huang, C. Su, K.-H. Chen, and L.-C. Chen, "Effect of Copper Oxide Oxidation State on the Polymer-Based Solar Cell Buffer Layers" *ACS Appl. Mater. Interfaces* **6**, 22445 (2014).

14. D. Kim, G. Y. Kim, C. Ko, S. R. Pae, Y. S. Lee, O. Gunawan, D. F. Ogletree, W. Jo, and B. Shin, "Effects of Postsynthesis Thermal Conditions on Methylammonium Lead Halide Perovskite: Band Bending at Grain Boundaries and Its Impacts on Solar Cell Performance" *J. Phys. Chem. C* **120**, 21330 (2016).

15. T. Todorov, T. Gershon, O. Gunawan, Y. S. Lee, C. Sturdevant, L.-Y. Chang. and S. Guha, "Monolithic Perovskite-CIGS Tandem Solar Cells via In Situ Band Gap Engineering," *Adv. Energy Mater.* **5**, 1500799 (2015).

16. H. H. Park, R. Heasley, L. Sun, V. Steinmann, R. Jaramillo, K. Hartman, R. Chakraborty, P. Sinsermsuksakul, D. Chua, T, Buonassisi, and R. G. Gordon, "Co-Optimization of SnS Absorber and Zn(O,S) Buffer Materials for Improved Solar Cells," *Prog. Photovolt: Res. Appl.* **23**, 90 (2015).

17. T. Hwang, A. J. Yun, J. Kim, D. Cho, S. Kim, S. Hong, and B. Park, "Electronic Traps and Their Correlations to Perovskite Solar Cell Performance via Compositional and Thermal Annealing Controls.," *ACS Appl. Mater. Interfaces* **11**, 6907 (2019).

18. M. Saliba, T. Matsui, J.-Y. Seo, K. Domanski, J.-P. Correa-Baena, M. K. Nazeeruddin, S. M. Zakeeruddin, W. Tress, A. Abate, A. Hagfeldt, and M. Grätzel, "Cesium-Containing Triple Cation Perovskite Solar Cells: Improved Stability, Reproducibility and High Efficiency," *Energy Environ. Sci*. **9**, 1989 (2016).

19. Z. Li, M. Yang, J.-S. Park, S.-H. Wei, J. J. Berry, K. Zhu, "Stabilizing Perovskite Structures by Tuning Tolerance Factor: Formation of Formamidinium and Cesium Lead Iodide Solid-State Alloys," *Chem. Mater.* **28**, 284 (2016).

20 S. Gholipour, A. Morteza Ali, J.-P. Correa-Baena, S.-H. Turren-Cruz, F. Tajabadi, W. Tress, N. Taghavinia, M. Grätzel, A. Abate, F. D. Angelis, C. A. Gaggioli, E. Mosconi, A. Hagfeldt, and M. Saliba, "Globularity-Selected Large Molecules for a New Generation of Multication Perovskites," *Adv. Mater*. **29**, 1702005 (2017).

21. X. Dong, X. Fang, M. Lv, B. Lina, S. zhang, J. Ding, and N. Yuan, "Improvement of the Humidity Stability of Organic-Inorganic Perovskite Solar Cells using Ultrathin Al_2O_3 Layers Prepared by Atomic Layer Deposition," *J. Mater. Chem. A* **3**, 5360 (2015).

22. E. J. Juarez-Perez, L. K. Ono, M. Maeda, Y. Jiang, Z. Hawash, and Y. Qi, "Photodecomposition and Thermal decomposition in Methylammonium Halide Lead Perovskites and Inferred Design Principles to Increase Photovoltaic Device Stability," *J. Mater. Chem. A* **6**, 9604 (2018).

23. E. Smecca, Y. Numata, I. Deretzis, G. Pellegrino, S. Boninelli, T. Miyasaka, A. La Magnaa, and A. Alberti, "Stability of Solution-Processed $MAPbI_3$ and $FAPbI_3$ Layers," *Phys. Chem. Chem. Phys.* **18**, 13413 (2016).

24. J. Yang, Q. Hong, Z. Yuan, R. Xu, X. Guo, S. Xiong, X. Liu, S. Braun, Y. Li, J. Tang, C. Duan, M. Fahlman, and Q. Bao, "Photostability of Perovskite Solar Cells: Unraveling Photostability of Mixed Cation Perovskite Films in Extreme Environment," *Adv. Optical Mater*. **6**, 1800262 (2016).

25. T. Hwang, B. Lee, J. Kim, S. Lee, B. Gil, A. J. Yun, and B. Park, "From Nanostructural Evolution to Dynamic Interplay of Constituents: Perspectives for Perovskite Solar Cells," *Adv. Mater.* **30**, 1704208 (2018).

26. S. Wang, Z. Huang, X. Wang, Y. Li, M. Günther, S. Valenzuela, P. Parikh, A. Cabreros, W Xiong, and Y. S. Meng, "Unveiling the Role of tBP–LiTFSI Complexes in Perovskite Solar Cells," *J. Am. Chem. Soc.* **140**, 16720 (2018).

27. A. K. Jena, M. Ikegami, and T. Miyasaka, "Severe Morphological Deformation

of Spiro-OMeTAD in (CH$_3$NH$_3$)PbI$_3$ Solar Cells at High Temperature," *ACS Energy Lett.* **2**, 1760 (2017).

28. F. Wang, S. Bai, W. Tress, A. Hagfeldt, and F. Gao, "Defects Engineering for High-Performance Perovskite Solar Cells," *npj Flex. Electron.* **2**, 22 (2018).

29. J. Chang, Z. Lin, H. Zhu, F. H. Isikgor, Q.-H. Xu, C. Zhang, Y. Hao, and J. Ouyang, "Enhancing the Photovoltaic Performance of Planar Heterojunction Perovskite Solar Cells by Doping the Perovskite Layer with Alkali Metal Ions," *J. Mater. Chem. A*, **4**, 16546 (2016).

30. M. Saliba, T. Matsui, J.-Y. Seo, K. Domanski, J.-P. Correa-Baena, M. K. Nazeeruddin, S. M. Zakeeruddin, W. Tress, A. Abate, A. Hagfeldtd, and M. Grätzel, "Cesium-Containing Triple Cation Perovskite Solar Cells: Improved Stability, Reproducibility and High Efficiency," *Energy Environ. Sci.* **9**, 1989 (2016).

31 A. D. Jodlowski, C. Roldán-Carmona, G. Grancini, M. Salado, M. Ralaiarisoa, S. Ahmad, N. Koch, L. Camacho, G. d. Miguel, and M. K. Nazeeruddin, "Large Guanidinium Cation Mixed with Methylammonium in Lead Iodide Perovskites for 19% Efficient Solar Cells" *Nat. Energy* **2**, 972 (2017).

32. H. Zheng, G. Liu, L. Zhu, J. Ye, X. Zhang, A. Alsaedi, T. Hayat, X. Pan, and S. Dai, "The Effect of Hydrophobicity of Ammonium Salts on Stability of Quasi-2D Perovskite Materials in Moist Condition," *Adv. Energy Mater.* **8**, 1800051 (2018).

33. Q. Wang, F. Lin, C.-C. Chueh, T. Zhao, M. Eslamian, and A. K.-Y .Jen,

"Enhancing Efficiency of Perovskite Solar Cells by Reducing Defects through Imidazolium Cation Incorporation," *Mater. Today Energy* **7**, 161 (2018).

34. X. Huang, H. Guo, K. Wang, and X. Liu, "Ionic Liquid Induced Surface Trap-State Passivation for Efficient Perovskite Hybrid Solar Cells," *Org. Electron.* **41**, 42 (2017).

35. K. T. Cho, S. Paek, G. Grancini, C. Roldán-Carmona, P. Gao, Y. Lee, and M. K. Nazeeruddin, "Highly Efficient Perovskite Solar Cells with a Compositionally Engineered Perovskite/Hole Transporting Material Interface," *Energy Environ. Sci.* **10**, 621 (2017).

36. Q. Jiang, Y. Zhao, X. Zhang, X. Yang, Y. Chen, Z. Chu, Q. Ye, X. Li, Z. Yinm, and J. You, "Surface Passivation of Perovskite Film for Efficient Solar Cells," *Nat. Photonics* **13**, 460 (2019).

37. J. M. Frost, K. T. Butler, F. Brivio, C. H. Hendon, M. Schilfgaarde, and A. Walsh, "Atomistic Origins of High-Performance in Hybrid Halide Perovskite Solar Cells," *Nano Lett*. **14**, 2584 (2014).

38. A. Amat, E. Mosconi, E. Ronca, C. Quarti, P. Umari, M.. K. Nazeeruddin, M. Gratzel, and F. D. Angelis, "Cation-Induced Band-Gap Tuning in Organohalide Perovskites: Interplay of Spin–Orbit Coupling and Octahedra Tilting," *Nano Lett*. **14**, 3608 (2014).

39. K. Bolton, R. D. Brown, F.R. Burden, and A. Mishra, "The Microwave Spectrum and Dipole Moment of 1,2,4-Triazole: Identification of Tautomer in Vapour Phase," *Chem. Commun*. **15,** 873 (1971).

40. K. S. Rao, and A.K. Chaudhary, "Investigation of the Thermal Decomposition and Stability of Energetic 1,2,4-Triazole Derivatives using a UV Laser Based Pulsed Photoacoustic Technique," *RSC Adv.* **6**, 47646 (2016).

41. C. Ainsworth, "1,2,4-Triazole" *Org. Synth.* **40**, 99 (1960).

42. M. Abdi-Jalebi, M. I. Dar, A. Sadhanala, S. P. Senanayak, M Franckevicius, N. Arora, Y. Hu, M. K. Nazeeruddin, S. M. Zakeeruddin, M Grätzel, and R. H. Friend, "Impact of Monovalent Cation Halide Additives on the Structural and Optoelectronic Properties of $CH_3NH_3PbI_3$ Perovskite," *Adv. Energy Mater.* **6**, 1502472 (2016).

43. J. Fan, Y. Ma, C. Zhang, C. Liu, W. Li, R. E. I. Schropp, and Y. Mai, "Thermodynamically Self-Healing 1D–3D Hybrid Perovskite Solar Cells," *Adv. Energy Mater.* **8**, 1703421 (2018).

44. W.-G. Li, H.-S. Rao, B.-X. Chen, X.-D. Wanga, and D.-B. Kuang, "A Formamidinium–Methylammonium Lead Iodide Perovskite Single Crystal Exhibiting Exceptional Optoelectronic Properties and Long-Term Stability" *J. Mater. Chem. A* **5**, 19431 (2017).

45. A. Mahendran, P. Gopinath, and R. Breslow, "Single Molecule Conductance of Aromatic, Nonaromatic, and Partially Antiaromatic Systems," *Tetrahedron Lett.* **56**, 4833 (2015).

46. J. V. Passarelli, D. J. Fairfield, N. A. Sather, M. P. Hendricks, and H. Sai, "Enhanced Out-of-Plane Conductivity and Photovoltaic Performance in n = 1 Layered Perovskites through Organic Cation Design," *J. Am. Chem. Soc.* **140**, 7313 (2018).

47. A. D. Jodlowski, C. Roldán-Carmona, G. Grancini, M. Salado, M. Ralaiarisoa, S. Ahmad, N. Koch, L. Camacho, G. d. Miguel, and M. K. Nazeeruddin, "Large Guanidinium Cation Mixed with Methylammonium in Lead Iodide Perovskites for 19% Efficient Solar Cells" *Nat. Energy* **2**, 972 (2017).

48. G. Kieslich, S. Sun, and A. K. Cheetham, "Solid-State Principles Applied to Organic-Inorganic Perovskites: New Tricks for an Old Dog" *Chem. Sci*. **5**, 4712 (2014).

49. J. Kim, T. Hwang, S. Lee, B. Lee, J. Kim, G. S. Jang, S. Nam, and B. Park, "Solvent and Intermediate Phase as Boosters for the Perovskite Transformation and Solar Cell Performance," *Sci. Rep*. **6**, 25648 (2016).

50. B. Lee, T. Hwang, S. Lee, B. Shin, and B. Park, "Microstructural Evolution of Hybrid Perovskites Promoted by Chlorine and its Impact on the Performance of Solar Cell," *Sci. Rep*. **9**, 4803 (2019).

51. B. Lee, B. Shin, and B. Park, ""Uniform Cs2SnI6 Thin Films for Lead-Free and Stable Perovskite Optoelectronics via Hybrid Deposition Approaches"," *Electron. Mater. Lett*. **15**, 192 (2019).

52. H. Fujiwara, M. Kato, M. Tamakoshi, T. Miyadera, and M. Chikamatsu, "Optical Characteristics and Operational Principles of Hybrid Perovskite Solar Cells," *Phys. Status Solidi A* **215**, 1700730 (2018).

53. J. H. Lee, J.-H. Lee, E.-H. Kong, and H. M. Jang, "The nature of hydrogen-bonding interaction in the prototypic hybrid halide perovskite, tetragonal $CH_3NH_3PbI_3$," *Sci. Rep*. **6**, 21687 (2016).

54. K. Bolton, R. D. Brown, F.R. Burden, and A. Mishra, "The Microwave Spectrum and Dipole Moment of 1,2,4-Triazole: Identification of Tautomer in Vapour Phase,"

Chem. Commun. **15,** 873 (1971).

55. J. M. Frost, K. T. Butler, F. Brivio, C. H. Hendon, M. V. Schilfgaarde, and A. Walsh, "Atomistic Origins of High-Performance in Hybrid Halide Perovskite Solar Cells," *Nano Lett*. **14**, 2584 (2014).

56. J. Catalán, M. Sánchez-Cabezudo, J. L. G. De Paz, J. Elguero, R. W. Taft, and F. Anvia, "The Tautomerism of 1,2,3-triazole, 3(5)-Methylpyrazole, and Their Cations," *J. Comput. Chem.* **10**, 426 (1989).

57. D. Christen, J. H. Griffiths, and J. Sheridan, "The Microwave Spectrum of Imidazole; Complete Structure and the Electron Distribution from Nuclear Quadrupole Coupling Tensors and Dipole Moment Orientation," *Z. Naturforsch. A*. **36**, 1378 (1981).

58. K. T. Potts, "The Chemistry of 1,2,4-Triazoles," *Chem. Rev*. **61**, 87 (1961).

59. J. G. Aston, C. W. Siller, and G. H. Messerly, "Heat Capacities and Entropies of Organic Compounds. III. Methylamine from 11.5°K. to the Boiling Point. Heat of Vaporization and Vapor Pressure. The Entropy from Molecular Data," *J. Am. Chem. Soc.*, **59**, 1743 (1937).

60. I. Zarazua, G. Han, P. P. Boix, S. Mhaisalkar, F. Fabregat-Santiago, I. Mora-Sero, J. Bisquert, and G. Garcia-Belmonte, "Surface Recombination and Collection Efficiency in Perovskite Solar Cells from Impedance Analysis," *J. Phys. Chem. Lett*. **7**, 5105 (2016).

61. O. lmora, C. Aranda, E. Mas-Marza, and G. Garcia-Belmonte, "On Mott-Schottky Analysis Interpretation of Capacitance Measurements in Organometal Perovskite Solar Cells," *Appl. Phys. Lett*. **109**, 173903 (2016).

62. I. Zarazua, J. Bisquert, and G. Garcia-Belmonte, "Light-Induced Space-Charge Accumulation Zone as Photovoltaic Mechanism in Perovskite Solar Cells," *J.*

Phys. Chem. Lett. **7**, 525 (2016).

63. S. A. L. Weber, I. M. Hermes, S.-H. Turren-Cruz, C. Gort, V. W. Bergmann, L. Gilson, A. Hagfeldt, M. Gratzel, W. Tress, and R. Berger, "How the Formation of Interfacial Charge causes Hysteresis in Perovskite Solar Cells," *Energy Environ. Sci*. **11**, 2404 (2018).

64. T. Walter, R. Herberholz, C. Müller, and H. W. Schock, "Determination of Defect Distributions from Admittance Measurements and Application to $Cu(In,Ga)Se_2$ Based Heterojunctions," *J. Appl. Phys*. **80**, 4411 (1996).

65. D. Prochowicz, P. Yadav, M. Saliba, M. Saski, S. M. Zakeeruddin, J. Lewinski, and M. Gratzel, "Reduction in the Interfacial Trap Density of Mechanochemically Synthesized $MAPbI_3$," *ACS Appl. Mater. Interfaces* **9**, 28418 (2017).

66. M. Samiee, S. Konduri, B. Ganapathy, R. Kottokkaran, H. A. Abbas, A. Kitahara, P. Joshi, L. Zhang, M. Noack, and V. Dalal, "Defect Density and Dielectric Constant in Perovskite Solar Cells," *Appl. Phys. Lett*. **105**, 153502 (2014).

67. A. J. Yun, J. Kim, T. Hwang, and B. Park, "Origins of Efficient Perovskite Solar Cells with Low-Temperature Processed SnO_2 Electron Transport Layer," *ACS Appl. Energy Mater,* **2**, 3554 (2019).

Appendix:

List of Publications and Presentations

A.1. Publications (International)

1. "Triamine-Based Aromatic Cation as a Novel Stabilizer for Efficient Perovskite Solar Cells"

   Jinhyun Kim, Alan Jiwan Yun, Bumjin Gil, Younghyun Lee, and Byungwoo Park*

   Adv. Func. Mater. (Accepted).

2. "Interfacial Modification and Defect Passivation by Crosslinking Interlayer with Realization of Efficient and Stable CuSCN-Based Perovskite Solar Cell"

   Jinhyun Kim,[+] Younghyun Lee,[+] Alan Jiwan Yun,[+] Bumjin Gil, and Byungwoo Park*

   Adv. Func. Mater. (In Preparation).

3. "Origins of Efficient Perovskite Solar Cells with Low-Temperature Processed SnO$_2$ Electron Transport Layer"

   Alan Jiwan Yun,[+] **Jinhyun Kim**,[+] Taehyun Hwang, and Byungwoo Park[*]

   ACS Appl. Energy Mater. (2019). DOI: 10.1021/acsaem.9b00293.

4. "An Aromatic Diamine Molecule as the *A*-Site Solute for Highly Durable and Efficient Perovskite Solar Cells"

   Jinhyun Kim, Taehyun Hwang, Byungho Lee, Sangheon Lee, Kimin Park, Helen Hejin Park, and Byungwoo Park[*]

   Small Methods **3**, 1800361 (2019). **[Front Cover]**

5. "From Nanostructural Evolution to Dynamic Interplay of Constituents: Perspectives for Perovskite Solar Cells"

Taehyun Hwang,[+] Byungho Lee,[+] **Jinhyun Kim**,[+] Sangheon Lee,[+] Bumjin Gil, Alan Jiwan Yun, and Byungwoo Park[*]

Adv. Mater. **30**, 1704208 (2018). **[Inside Front Cover]**

6. "Synergetic Effect of Double-Step Blocking Layer for the Perovskite Solar Cell"

Jinhyun Kim, Taehyun Hwang, Sangheon Lee, Byungho Lee, Jaewon Kim, Jaewook Kim, Bumjin Gil, and Byungwoo Park[*]

J. Appl. Phys. **122**, 145106 (2017).

7. "Solvent and Intermediate Phase as Boosters for the Perovskite Transformation and Solar Cell Performance"

Jinhyun Kim, Taehyun Hwang, Sangheon Lee, Byungho Lee, Jaewon Kim, Gil Su Jang, Seunghoon Nam, and Byungwoo Park[*]

Sci. Rep. **6**, 25648 (2016).

8. "Electronic Traps and Their Correlations to Perovskite Solar Cell Performance via Compositional and Thermal Annealing Controls"

Taehyun Hwang, Alan Jiwan Yun, **Jinhyun Kim**, Duckhyung Cho, Sangyeon Kim, Seunghun Hong, and Byungwoo Park[*]

ACS Appl. Mater. Interfaces **11**, 6907 (2019).

9. "Complementary Surface Modification by Disordered Carbon and Reduced Graphene Oxide on SnO_2 Hollow Spheres as an Anode for Li-Ion Battery"

Hyungsub Woo, Sungun Wi, Jaewon Kim, **Jinhyun Kim**, Sangheon Lee, Taehyun Hwang, Joonhyeon Kang, Jaewook Kim, Kimin Park, Bumjin Gil,

Seunghoon Nam,[*] and Byungwoo Park[*]

Carbon **129**, 342 (2018).

10. "Evaluating the Optoelectronic Quality of Hybrid Perovskites by Conductive Atomic Force Microscopy with Noise Spectroscopy"

Byungho Lee, Sangheon Lee, Duckhyung Cho, **Jinhyun Kim**, Taehyun Hwang, Kyung Hwan Kim, Seunghun Hong,[*]Taeho Moon,[*] and Byungwoo Park[*]

ACS Appl. Mater. Interfaces **8**, 30985 (2016).

11. "Investigation of Chlorine-Mediated Microstructural Evolution of $CH_3NH_3PbI_3(Cl)$ Grains for High Optoelectronic Responses"

Taehyun Hwang, Duckhyung Cho, **Jinhyun Kim**, Jaewon Kim, Sangheon Lee, Byungho Lee, Kyung Hwan Kim, Seunghun Hong, Chunjoong Kim, and Byungwoo Park[*]

Nano Energy **25**, 91 (2016).

12. "Integration of $CdSe/CdSe_xTe_{1-x}$ Type-II Heterojunction Nanorods into Hierarchically Porous TiO_2 Electrode for Efficient Solar Energy Conversion"

Sangheon Lee,[+] Joseph C. Flanagan,[+] Joonhyeon Kang, **Jinhyun Kim**, Moonsub Shim,[*] and Byungwoo Park[*]

Sci. Rep. **6**, 26992 (2016).

13. "Organic-Acid Texturing of Transparent Electrodes Toward Broadband Light Trapping in Thin-Film Solar Cells"

Woojin Lee, Taehyun Hwang, Sangheon Lee, Seung-Yoon Lee, Joonhyeon Kang, Byungho Lee, **Jinhyun Kim**, Taeho Moon,[*] and Byungwoo Park[*]

Nano Energy **17**, 180 (2015).

225   *Appendix.*

14. "Facile Conversion Synthesis of Densely-Formed Branched ZnO-Nanowire Arrays for Quantum-Dot-Sensitized Solar Cells"

Woojin Lee, Suji Kang, Taehyun Hwang, Kunsu Kim, Hyungsub Woo, Byungho Lee, Jaewon Kim, **Jinhyun Kim**, and Byungwoo Park[*]

Electrochim. Acta **167**, 194 (2015).

15. "Nanoroughness Control of Al-Doped ZnO for High Efficiency Si Thin-Film Solar Cells"

Seung-Yoon Lee, Taehyun Hwang, Sangheon Lee, Woojin Lee, Byungho Lee, **Jinhyun Kim**, Soohyun Kim, Hyun Lee, Heon-Min Lee, and Byungwoo Park[*]

Curr. Appl. Phys. **15**, 1353 (2015).

16. "Improving Scattering Layer through Mixture of Nanoporous Spheres and Nanoparticles in ZnO-Based Dye-Sensitized Solar Cells"

Chohui Kim, Hongsik Choi, Jae Ik Kim, Sangheon Lee, **Jinhyun Kim**, Woojin Lee, Taehyun Hwang, Suji Kang, Taeho Moon,[*] and Byungwoo Park[*]

Nanoscale Res. Lett. **9**, 295 (2014).

Appendix.

A.1. Presentations (International and Domestic)

1. "Origins of Efficient Perovskite Solar Cell with Low-Temperature Processed Tin Oxide Electron Transport Layer"

   Alan Jiwan Yun, **Jinhyun Kim**, Taehyun Hwang, Byungwoo Park

   International Conference on Electronic Materials and Nanotechnology for Green Environment (ENGE2018). Jeju, Korea, November 12-14, 2018.

2. "Unraveling the Origins that Enable Efficient Perovskite Solar Cells: Influence of Thermal Annealing via Temporal Evaluation"

   Taehyun Hwang, Byungho Lee, Sangheon Lee, **Jinhyun Kim**, Bumjin Gil, Alan Jiwan Yun, and Byungwoo Park

   Materials Research Society (MRS) Spring Meeting. Phoenix, AZ, April 2-6, 2018.

3. "Imidazole as a Cation-Dopant for Stable and Efficient Perovskite Solar Cells"

   Jinhyun Kim, Taehyun Hwang, Byungho Lee, Sangheon Lee, Bumjin Gil, Kimin Park, and Byungwoo Park

   Materials Research Society (MRS) Spring Meeting. Phoenix, AZ, April 2-6, 2018. **[Oral by Jinhyun Kim]**

4. "Organometallic Perovskite Synthesis for Efficient and Stable Perovskite Solar Cells"

   Jinhyun Kim, Taehyun Hwang, Sangheon Lee, Byungho Lee, Jaewon Kim, and Byungwoo Park

   Materials Research Society (MRS) Fall Meeting. Boston, MA, November 26-December 2, 2016. **[Poster by Jinhyun Kim]**

5. "Integration of II-VI Nanorods in Sensitized Photovoltaics via Open-Structured Photoanode and Co-Sensitization Strategy"

   Sangheon Lee, Joseph C. Flanagan, Joonhyeon Kang, **Jinhyun Kim**, Moonsub Shim, and Byungwoo Park

   Materials Research Society (MRS) Fall Meeting. Boston, MA, November 26-December 2, 2016.

6. "Organometallic Perovskite Synthesis for Efficient and Stable Perovskite Solar Cells"

   Jinhyun Kim, Taehyun Hwang, Sangheon Lee, Byungho Lee, Jaewon Kim, and Byungwoo Park

   International Conference on Electronic Materials and Nanotechnology for Green Environment (ENGE2016). Jeju, Korea, November 6-9, 2016. **[Poster by Jinhyun Kim]**

7. "Investigation of Chlorine-Mediated Microstructural Evolution of $CH_3NH_3PbI_3(Cl)$ for Enabling High Performance Solar Cell"

   Taehyun Hwang, Duckhyung Cho, **Jinhyun Kim**, Jaewon Kim, Sangheon Lee, Byungho Lee, Kyung Hwan Kim, Seunghun Hong, and Byungwoo Park

   International Conference on Electronic Materials and Nanotechnology for Green Environment (ENGE2016). Jeju, Korea, November 6-9, 2016.

8. "Integration of II-VI Nanorods in Sensitized Photovoltaics via Open-Structured Photoanode and Co-Sensitization Strategy"

   Sangheon Lee, Joseph C. Flanagan, Joonhyeon Kang, **Jinhyun Kim**, Moonsub Shim, and Byungwoo Park

International Conference on Electronic Materials and Nanotechnology for Green Environment (ENGE2016). Jeju, Korea, November 6-9, 2016.

9. "Integration of CdSe/CdSe$_x$Te$_{1-x}$ Type-II Heterojunction Nanorods into Hierarchically Porous TiO$_2$ Electrode for Efficient Solar Energy Conversion" Sangheon Lee, Joseph C. Flanagan, Joonhyeon Kang, **Jinhyun Kim**, Moonsub Shim, and Byungwoo Park
Global Photovoltaic Conference 2015 (GPVC2015). Busan, Korea, November 15-20, 2015.

국문초록

에너지 소비는 대표적으로 화석연료, 석유화학, 핵 발전에 의존되어 왔다. 본 에너지들은 지구온난화와 핵폐기물 등, 인류의 안전을 위협하고 있다. 차선책으로써, 재생에너지가 현재 에너지생산을 대체하고 있는 추세이나 공급량에 못 미치는 실정이다. 태양전지는 입사 광을 전기로 변환시켜주는 에너지 발전장치로써, 환경적 문제없이 에너지를 공급해줄 수 있는 촉망 받는 해결책이라고 할 수 있다. 태양전지를 에너지 시장에서 경쟁력을 갖게 하기 위해, 저비용에서의 높은 광 전환효율과 함께 높은 내구성을 포함하고 있어야 한다. 더 나아가, 웨어러블 기기와 같이 생활에 밀접할 수 있도록 적용 가능해야 한다. 그러므로 태양전지의 넓은 상용화를 위해서, 물질과 소자에 대한 과학적인 이해와 발전이 필요하다.

연구진들은 태양전지의 잠재성을 끌어내기 위하여 다양한 물질 및 소자 구조들을 탐구해 왔다. 특히, 광전특성이 뛰어난 박막반도체 물질을 태양전지에 적용시키는 방향이 널리 탐구 되었다. 그 중에서도, 유무기 페로브스카이트는 우수한 밴드갭, 확산거리, 흡수계수의 본연의 우수한 특성들로 인해 많은 주목을 받았다. 더 나아가 합성 및 공정의 간편함과 저비용에 있어서 대량생산에서 강한 이점을 지니고 있다. 하지만, 유무기 페로브스카이트에서의 유기물은 (methylamonium (MA) 또는 formamidinium (FA)) 외부 열, 빛, 수분에 높은 반응성을 가지고 있어서, 실생활에서의 적용이 어려운 실정이다. 유무기 페로브스카이트의 문제 이외에도, 소자 내에서의 전자 및 정공

전달물질은 가격이 높고 복잡한 공정을 요구하므로 유무기 페로브스카이트 태양전지의 상용화에 걸림돌이 되고 있다. 그러므로 현재의 한계를 뛰어넘기 위한 물질 및 소자의 추가적인 연구가 요구되어야 한다.

1장에서는 유무기 페로브스카이트와 태양전지의 기초적인 이해를 돕기 위한 소개를 할 것이다. 이는 물리화학적 접근에 의거한 소재 이론 및 태양전지의 작동원리를 다룸과 동시에, 태양전지의 광전특성을 향상시키기 위한 선행 연구들을 짚고 넘어가고자 한다. 더 나아가, 물질 및 소자의 분해이론과 이를 해결하기 위한 선행연구 되었던 해결 방안을 소개함으로써 유무기 페로브스카이트 연구분야를 이해하고자 한다.

2장에서는 페로브스카이트 태양전지의 이상적인 공정과 합성을 다루고자 한다. 2014년, 염소가 도핑된 페로브스카이트는 격자구조내의 패시베이션 효과로 많은 주목을 받아왔다. 이로 인하여, 염소 도핑은 성능향상과 안정성을 모두 올려주는 방법으로 여겨져 왔다. 하지만, 이를 합성하기 위한 화학적 이해는 미미하게 이루어져 왔고, 이를 이해하면 추가적인 최적화를 할 수 있는 가능성을 지니고 있다. 염소가 도핑된 페로브스카이트의 반응과정을 이해하기 위해, 다양한 공정과 합성법을 2장에서 구체적으로 다루었다. 결론 적으로는 반응의 정도를 조절하는 기술을 적용하여 반응 과정중의 중간상을 발견하는데 성공하였고, 이를 공학적으로 응용하여 극도로 안정한 페로브스카이트를 만드는데 성공하였다. 최종적으로, 이를 페로브스카이트 태양전지에 응용하여 안정적이고 고효율을 내는 소자를 만드는 방법을 논하고자

한다.

　　　3장에서는 전자전달물질의 합성과 공정을 다루고자 한다. 금속산화물은 전자전달물질로 널리 이용되어왔으며, 높은 수준의 박막을 얻기 위하여 복잡한 공정들을 요구로 한다. 대표적으로 진공공정 또는 용액공정을 이용하여 전자전달층을 투명전극 위에 증착 한다, 허나 각각의 방법에는 질 높은 박막을 형성하는데 문제를 가지고 있다. 또한 이러한 박막의 질은 상단에 증착이 될 페로브스카이트의 형성에도 영향을 준다. 그러므로 용액공정과 진공공정을 융합하여 단점들을 보완하고 소자의 성능을 향상시킨 이상적인 전자전달층 제작법을 소개하고자 한다.

　　　4장에서는 페로브스카이트의 분해과정을 관찰하는 내용을 다루고자 한다. 페로브스카이트 내부의 유기물부분은 페로브스카이트의 분해를 중점적으로 일으키는 부분으로 알려져 있고, 이를 분석하고 보완하는 방법론에 대해 공부해 보았다. 또한 새로운 페로브스카이트 디자인을 통한 광전특성 향상 원리를 다뤄보고자 한다. 대표적으로, 다양한 아민 개수의 방향족유기물을 이상적으로 활용하여 페로브스카이트의 유기 부분에 치환하였다. 방향족유기물의 구조특수성은 비편재화된 파이 결합으로 인해 소재 및 소자의 광전특성과 안정성을 기하급수적으로 향상시켰다. 더 나아가, 소재 이론 및 디자인 방법론 등을 소개하고자 한다.

　　　5장에서는, 전자전달물질의 안정성 및 비용적인 측면을 다루고자 한다. 대부분의 상황에서는, 금속산화물은 광촉매반응을 가지고 있으며, 이는 페로브스카이트와의 분해반응을 일으켜 낮은 소자

안정성을 가지게 된다. 그러므로, 안정적이고 효율적인 전자전달물질을 만드는 방법론에 대해 설명하고자 한다. 더 나아가, 전자전도도를 얻기 위한 금속산화물의 고온합성은 제조단가를 높이는 문제가 있기도 하다. 결과적으로, 저온에서 합성가능하고 안정하면서도 고효율을 소자를 만드는 방법론을 다루고자 한다.

6장에서는 페로브스카이트의 화학적인 요소들을 향상시키기 위한 복합적인 전략을 소개하고자 한다. 페로브스카이트는 유기물, 전이금속, 그리고 할로겐으로 이루어져있고, 유기물이 대표적으로 낮은 안정성을 가지고 있다. 유기물은 페로브스카이트 격자구조 내에 수소결합을 하고 있으며, 이는 극성성질을 띄는 외부환경과 높은 반응성을 가지고 있다. 그러므로 이러한 화학결합을 제어하기 위한 금속 그리고 저극성 유기물들을 복합적으로 응용하여 소재를 안정화시키는 방법을 논하고자 한다. 안정화 과정을 진행함과 동시에, 광전기적 특성 및 열역학적 변화를 관찰하고 소자에서의 성능 및 안정성 향상을 추가적으로 관찰하고자 한다.

주요어: 태양전지, 유무기 페로브스카이트, 조성공학, 용매, 양이온, 음이온, 전자전달물질, 정공전달물질, 안정성, 고분자, 금속산화물, 복합물질, 증착공정, 재결합, 결함, 전기적 트랩.

학번: 2013−23817

감사의 글

2013년 연구실 생활을 시작하여 6년이란 시간이 빠르게 지났습니다. 수많은 일들이 있었고 그 속에서 이뤄낸 작은 결실들과 가르침들을 간직하고 새로운 곳에서 새로운 도전을 하고자 합니다. 긴 유학생활 이후 익숙하지 않은 한국에서의 시간을 화려하고 가치 있게 만들어주신 교수님, 연구실 선후배들, 그리고 수많은 고마운 분들께 감사의 글을 적고자 합니다.

먼저 학위과정 동안 함께 연구자로써 성장할 수 있는 기회를 주신 박병우 교수님께 감사 드립니다. 연구에 대해 자유롭게 생각하고 토론할 수 있도록 기회들을 마련해주신 교수님의 배려는 연구를 창의적으로 바라보는데 많은 도움이 되었습니다. 또한 제가 연구 및 생활에 지칠 때 매번 위로해주시며 저의 삶의 원동력을 되새기며 힘을 낼 수 있게 해주었습니다. 자주 커피도 주시고 편하게 교수님과 소통할 수 있어서 대학원의 삶이 만족스러웠습니다.

제가 연구를 하면서 난관에 부딪치거나 조언을 구해야 할 때 아낌없이 도와주신 신병하교수님 그리고 대학원생분들 분께 이 자리를 빌어 진심으로 감사 드립니다. 다양한 의견과 해결책들을 나누며 지식적인 부분과 실험적인 부분들은 저를 더 뛰어난 연구자로 성장시켜주었습니다. 더불어 바쁘신 와중에 저희 학위논문 심사를 위해 귀한 시간을 내어주시고 조언을 주신 심사위원님들께도 감사 드립니다. 유기 및 고분자에 대한 깊은 이해를 많이 생각하고 논리를 펼칠 수 있게 도와주신 김장주교수님과 이태우교수님, 분야에 다양한 지식과 접근방법론을 심도 있게 생각할 수 있도록 조언해주신 김진영교수님과

234　　　　　　　　　　　　　　*감사의 글*

신병하교수님. 분야의 전반적인 큰 틀에서 여러 깨달음을 느끼게 해주셨던 김상범교수님의 조언들은 제가 학위를 마무리하는데 그리고 연구자가 되는데 있어서 큰 영향을 주었습니다.

학위 기간 동안 많은 도움을 주시고 즐거운 추억들을 함께 나누도록 도와주신 연구실 선후배님들께 감사의 말씀을 전합니다. 연구실 초기에 부족한 저를 도와주신 문태호 교수님과 남승훈 교수님, 깊은 경험과 지식에서 나오는 김천중 교수님과의 대화는 저를 즐겁고 분야에 대해 생각해보는 도전적인 자세를 느낄 수 있게 해주셨습니다. 또한 따뜻한 인품과 유머로 항상 연구실의 생기를 넣어주셨던 재익이형과 꽁치형, 그리고 연구실 초기에 가장 잘 챙겨주신 초희누나, 따뜻한 웃음을 지어주시며 좋은 말 그리고 위로도 해주신 수지누나덕분에 많이 배우고 보람된 연구실생활을 시작할 수 있었습니다. 준현이형과는 같은 분야는 아니셨지만, 안에서 또는 밖에서 같이 연구실 및 인생에 대해 많은 얘기를 나누고 혼나면서 도전적인 실험정신 및 노력보단 성과라는 말을 가슴에 새기며 지낼 수 있도록 도와주셨습니다. 연구실에서 늠름한 형이시자 따뜻하게 후배들을 아껴주셨던 성언이형을 보면서 본받을 점이 많다고 생각하였습니다. 항상 후배들의 연구 및 생활을 챙기셨고 좋은 추억들을 많이 주셨습니다. 많이 바쁘셔서 자주 뵙지는 못했지만 항상 따뜻하게 대해주셨던 승윤이형 그리고 논자시 및 강력한 정보력으로 저의 졸업도움 및 조언을 해주셨던 선태형께도 깊은 감사의 인사를 드립니다. 페로브스카이트 태양전지를 초기 때 시작하여 많은 난관에 봉착할 때 태현이형 그리고 병호형과 같이 의견들을 나누며 헤쳐나갔습니다. 때로는 엄격한 선배였지만, 함께 연구하고 놀면서

연구를 발전시키는 길이 심심하지 않고 위안이 많이 되었습니다. 연구 이외에도 병호형과 태현이형에게는 감사하고 미안한 것도 많습니다. 제가 고집도 부리고 잘못된 행동이 있을 때 지적해주시며 더 좋은 연구자의 길로써 인도하심에 진심으로 감사 드립니다. 저랑 동갑이자 저의 선배인 상헌이에게도 많이 감사합니다. 열정만 가득하고 철없던 연구실 초기시절 항상 물어보면 친절하게 도와주고 의견도 내주면서 어떻게 보면 저보다 형 같은 구석이 많다고 느꼈습니다. 매번 사람들을 도우려는 착한 심성은 어딜 가든 좋은 결과를 낼 수 있으리라 장담하고 기원합니다. 형섭이형과는 정말 많은 추억들이 있었고 같이 여행도 가며 돈독한 우정을 지켜나갈 수 있었으나, 요새 많이 바쁘신 거 같아서 아쉽습니다. 인생에 대해서도 많은 얘기를 나누며 위로도 많이 해주시고 정신 없었던 학위과정 속에 너무도 감사한 사람이었습니다. 재원이형께서도 항상 든든한 형처럼 대화하고 저의 고민 그리고 난관들을 들어주시며 격려해주신 부분들이 많이 위안이 되었습니다. 어떻게 보면 저는 연구실에서 철없는 막내처럼 지내왔고 인격적으로 훌륭했었던 선배들 덕에 행복한 연구생활을 했다고 생각하고 아마 선배님들께서도 동의하실 거라 생각합니다. 막내의 생활을 즐기고 있을 때 후배들이 많이 들어왔습니다. 부지런하고 앞장서서 문제를 잘 해결해나가는 지완이, 성품이 바르고 열심히 하는 범진이, 돌발행동을 해서 당황스럽지만 마음만은 따뜻한 기민이, 그리고 지금까지 날 잘 따라와주고 믿어준 고마운 영현이에게 남은 연구실 생활을 즐겁고 잘 보내라는 말을 전합니다.

　　연구실 외에도 저에게 서울대대학원에서의 삶은 감사한

236　　　　　　　　　　　　　　　　　　　　*감사의 글*

부분들이 많았습니다. 연구실외에서도 연구적인 도움을 많이 받았고 서로 도우며 생각과 도전정신을 키워나갔습니다. 우선 신병하교수님 연구실의 김대한씨에게 이 자리를 빌려 감사의 인사 드립니다. 웃음을 항상 잃지 않으시며 죄송할 정도로 저희에게 많은 도움을 주셨습니다. 또한 김대형교수님 연구실의 태규와 웅찬이에게도 감사의 인사를 드립니다. 룸메로 만나 페로브스카이트에 대해 아무것도 모르던 시절 같이 헤매고 의견 나누고 장비도 조금씩 써보고 많은 위안이 되었습니다. 또한 밖에서 보면서 참 좋은 사람이라는 것들을 많이 느꼈습니다. 이제는 페로브스카이트에 대해 심도 있는 대화를 할 수 있는 횟수는 줄어들겠지만, 훌륭한 동생 그리고 연구원으로서 마주하기를 바랍니다. 약 6년이란 시간 동안 새로 형성된 형 동생 친구들이 많습니다. 항상 심심한 밤이면 같이 한잔을 기울이며 인생애기 나누던 혜성이형은 저에게 정말 고마운 존재입니다. 형의 인생관이나 순수한 열정 그리고 문제를 해결해나가는 말씀들을 들을 때 참으로 배울 점이 많은 사람이라는걸 느꼈습니다. 그리고 너무도 즐겁게 형과 같이 여행도하고 놀았던 시간들은 제 대학원생활에 활력소가 되어주었습니다. 학교를 떠나 이후에도 형과 함께 즐거운 추억들을 계속해서 만들어 나가고 싶습니다. 또한 병관이도 참으로 소중한 동생입니다. 항상 병관이랑 만나면 텐션도 올라가고 즐거웠습니다. 같이 있으면 치유 받는다는 느낌이 드는 저에게 굉장히 좋았던 사람입니다. 그 외에도 군대동기들, 서울대입구역에서의 감사한 사람들 등등 너무도 많은 사람들이 있지만, 항상 감사하고 소중했습니다. 언제나 즐겁고 행복하길 기원하고 그런 과정에 제가 함께하길 바랍니다.

감사의 글

중학교 때부터 유학을 가 한국에 중학교 고등학교 동창이 많이 있지는 않지만 이 자리를 빌어 소중한 친구들에게 감사하다는 말 하고 싶습니다. 알렉스는 고등학교 때부터 참 찰떡같이 붙어 지내던 친구였습니다. 철없는 우리들은 서로 티격태격하며 지금까지 왔지만, 고등학교 그리고 대학교에 있어서 참으로 위안도 많이 되고 서로 잘 챙겨주는 죽마고우 같은 인연이 되었음에 감사하게 생각합니다. 또한 JD팸의 근희 윤재와도 지금 다들 각자의 길에서 열심히 살고 있지만, 지금까지 제가 밟아온 길에 많은 도움 그리고 격려가 되었습니다. 경환이는 회사에서 보게 될 테지만, 참으로 재미있는 추억들도 많았고 앞으로 즐기면서 나갈 미래가 기대가 됩니다.

마지막으로 박사학위를 받게 되는 지금까지 제가 걱정 없이 학업에만 전념할 수 있도록 지지해주신 부모님께 감사드립니다. 제가 이렇게 까지 할 수 있었을까 의심을 하고 중간에 수많은 난관들이 있었으나, 그럴 때마다 응원해주고 지지해주셔서 제가 잘 마무리 지었음에 의심하지 않습니다. 듣기 싫은 소리들을 하셨을 때도 이 모든 것들이 저에 대한 걱정과 발전을 위해 하셨다는 것들을 알고 있습니다. 또한 부모님께서 걱정하지 않으시기를 바라며 더 열심히 노력하기도 했던 것 같습니다. 지금까지 받아온 사랑과 지원, 앞으로 천천히 갚아나가도록 하겠습니다. 사랑합니다.

2019년 8월
김진현 드림

감사의 글